Full Band Monte Carlo Simulation

of Nanowires and Nanowire Field Effect Transistors

by

Raghuraj Hathwar

A Dissertation Presented in Partial Fulfillment
of the Requirements for the Degree
Doctor of Philosophy

Approved July 2016 by the
Graduate Supervisory Committee:

Stephen Goodnick, Chair
Marco Saraniti
Dragica Vasileska
David Ferry

ARIZONA STATE UNIVERSITY

August 2016

ABSTRACT

In this work, transport in nanowire materials and nanowire field effect transistors is studied using a full band Monte Carlo simulator within the tight binding basis. Chapter 1 is dedicated to the importance of nanowires and nanoscale devices in present day electronics and the necessity to use a computationally efficient tool to simulate transport in these devices. Chapter 2 discusses the calculation of the full band structure of nanowires based on an atomistic tight binding approach, particularly noting the use of the exact same tight binding parameters for bulk band structures as well as the nanowire band structures. Chapter 3 contains the scattering rate formula for deformation potential, polar optical phonon, ionized impurity and impact ionization scattering in nanowires using Fermi's golden rule and the tight binding basis to describe the wave functions. A method to calculate the dielectric screening in 1D systems within the tight binding basis is also described. Importantly, the scattering rates of nanowires tends to the bulk scattering rates at high energies, enabling the use of the same parameter set that were fitted to bulk experimental data to be used in the simulation of nanowire transport. A robust and efficient method to model interband tunneling is discussed in chapter 4 and its importance in nanowire transport is highlighted. In chapter 5, energy relaxation of excited electrons is studied for free standing nanowires and cladded nanowires. Finally, in chapter 6, a full band Monte Carlo particle based solver is created which treats confinement in a full quantum way and the current voltage characteristics as well as the subthreshold swing and percentage of ballistic transport is analyzed for an $In_{0.7}Ga_{0.3}As$ junctionless nanowire field effect transistor.

ACKNOWLEDGMENTS

I am deeply grateful to my advisor Dr. Stephen M. Goodnick. His support and advice was essential to this work and this thesis would not have been completed without them. His knowledge in the area helped me traverse the difficult problems encountered in this work. I would like to thank Dr. Marco Saraniti, for supporting me throughout my PhD, for allowing me to work on his Monte Carlo code and develop it into this thesis. Without his technical and computational experience and resources none of this work would have been possible. I would also like to thank Dr. Dragica Vasileska and Dr. David Ferry for being a part of my Graduate Advisory Committee and for always being available to lend me advice whenever I encountered road blocks in my research. I would like to acknowledge the numerical device modeling group at Intel, Oregon, for funding the project and in particular Dr. Roza Kotlyar for her valuable advice and insight into the direction of this project.

Last but not least, I am forever grateful to my parents for the constant support and love they have shown towards me and to my friends for always being there when I needed them the most.

TABLE OF CONTENTS

Page

LIST OF TABLES…………………………………………………………………..vi

LIST OF FIGURES………………………………………………………………...vii

CHAPTER

1. INTRODUCTION 1

1.1. Emergence of Nanoscale Devices.. 1

1.2. Simulation Methods for Nanoscale Structures 2

2. BAND STRUCTURE OF BULK AND NANOWIRE MATERIALS 8

2.1. The Empirical Tight Binding Method... 9

2.2. Band Structure of Nanowires.. 17

2.2.1. Supercell Creation.. 18

2.2.2. Surface Passivation 20

2.2.3. Band Structures of Si and InAs Nanowires 22

2.2.4. Eigenvalue Solver 25

2.2.5. Density of States 26

3. SCATTERING RATES OF BULK AND NANOWIRE MATERIALS...................... 29

3.1. Tight Binding Scattering Rates of Bulk Materials..................................... 29

3.2. Tight Binding Scattering Rates of Nanowires 35

3.2.1. Deformation Potential Scattering Rate 36

CHAPTER Page

3.2.2. Polar Optical Phonon Scattering Rate 42

3.2.3. Ionized Impurity Scattering Rate 43

3.2.4. Dielectric Screening in Nanowires 45

3.2.5. Surface Roughness Scattering in Nanowires 49

3.2.6. Impact Ionization Scattering 52

3.3. Speed Optimizations for Scattering Rate Calculations 57

4. LOW FIELD AND HIGH FIELD TRANSPORT IN NANOWIRES.......................... 60

4.1. Rode's Method for 1D and 3D systems 60

4.2. Uniform Field Monte Carlo Simulations 66

4.3. Multiband Transport in Nanowires 73

4.3.1. Krieger and Iafrate (KI) Equations 75

4.3.2. Solution of the KI Equations.. 76

4.3.3. Numerical Solution of the KI Equations in Nanowires 82

4.3.4. Implementation of the KI Equation Solution within the Monte Carlo Method……...88

4.3.5. Effect of Interband Tunneling on Transport in Nanowires............................ 91

4.4. High Field Transport in Nanowires 103

5. ENERGY RELAXATION IN NANOWIRES 107

5.1. Energy Relaxation in Cladded Nanowires 110

CHAPTER Page

6. DEVICE SIMULATIONS 117

6.1. Junctionless Nanowire Field Effect Transistors 117

6.2. Transport across Different Slabs 124

6.3. Surface Injection at Contacts 125

6.4. Simulation of $In_{0.7}Ga_{0.3}As$ JNFET 128

6.5. Ballistic Percentages 131

7. SUMMARY AND CONCLUSIONS 134

7.1. Future Work 137

REFERENCES 139

LIST OF TABLES

Table Page

2.1: Parameter List for the $sp^3d^5s^*$ Empirical Tight Binding Method Including Spin-orbit Interaction for GaAs, Si and InAs. 12

2.2: Two Center Integral Formulae for the ETB Method 13

LIST OF FIGURES

Figure Page

2.1: Bulk Band Structures of a) GaAs, b) Si and c) InAs………………………….. 16

2.2: Primitive Cell Structure of GaAs…………………………………………… 17

2.3: The Supercell Structure for a Wurtzite GaN-InN Superlattice (Zhou2013)…... 19

2.4: The Supercell Structure for a Zinc Blende 3 nm x 3 nm Si NW along [111]…. 20

2.5: Variation of the Band Gap Obtained using the Hybridization Method………… 22

2.6: Band structure of Si and InAs Nanowire along [100] and [111]………………. 23

2.7: Variation of band gaps of Si, GaAs and InAs Nanowires……………………… 25

2.8: Reduction in the Bandwidth using a Reverse Cuthill Mckee Algorithm………. 26

2.9: Compariosn of Density of States between Bulk and Nanowires……………….. 28

3.1: a) Non-orthogonal and b) Orthogonal Orbitals in Si………………………….... 34

3.2: Bulk GaAs Non-polar and Polar Optical Phonon Scattering Rates…………….. 35

3.3: Comparison between Si Electron Bulk and Nanowire Scattering Rates……….. 40

3.4: Comparison between Si Hole Bulk and Nanowire Scattering Rates…………… 40

3.5: Comparison between GaAs Electron Bulk and Nanowire Scattering Rates…… 41

3.6: Compariosn between GaAs Hole Bulk and Nanowire Scattering Rates……….. 41

3.7: Comparison between GaAs POP Scattering Rate……………………………… 43

3.8: Ionized Impurity and Deformation Potential Scattering Rate for Si…………… 45

3.9: Plot of the Additional Atom Layer added to a 2.5 nm x 2.5 nm Si Nanowire … 51

3.10: Plot of the Atom Structure against a Poisson Grid in Two Dimensions……… 51

3.11: Plot of Impact Ionization and Deformation Potential Scattering Rate for Si … 57

Figure Page

3.12: Comparison Between the Loop Size of the Overlap Integral…………………. 59

4.1: Variation of the Phonon Limited Mobility of Si Nanowire with Width……….. 62

4.2: Variation of the Phonon Limited Mobility of GaAs Nanowire with Width……. 63

4.3: Variation of the Electron and Hole Mobility of a Si Nanowire along [100] with the Doping Concentration with and without Screening……………………... 64

4.4: Variation of the Electron and Hole mobility of a GaAs Nanowire along [100] with the Doping Concentration with and without Screening…………………... 65

4.5: Comparison of Drift Velocity versus Electric Field for Si Electrons and Holes.. 68

4.6: Comparison of Drift Velocity versus Electric Field for GaAs Electrons and Holes………………………………………………………………………. 69

4.7: Carrier Population at Steady State in a 3 nm x 3 nm GaAs Nanowire along [100] for a) 1.0 kV/cm, b) 10 kV/cm and c) 100 kV/cm……………………….. 72

4.8: Transient Plot of Electron Velocity for a 3 nm x 3 nm GaAs Nanowire along [100] for Different Electric Fields…………………………………………… 72

4.9: Transient Plot of Total Electron Energy for a 3 nm x 3 nm GaAs Nanowire along [100] for Different Electric Fields……………………………………….. 73

4.10: The Magnitude of the X Matrix between Band 1 and Band 7, and Band1 and Band 4 in a 3 nm x 3 nm InAs Nanowire along [100]…………………………. 81

4.11: (a) The Conduction Band of a 3 nm x 3 nm Si Nanowire along [100]. (b) The Difference between using the 1st Term and both the 1st and 2nd Terms in the Magnus Expansion on the Probability Coefficients……………………………. 84

Figure	Page

4.12: (a) The Difference between using Different Step Sizes for the Magnus 4th Order and the Runge-Kutta 4th Order (RK4) Method. The Region of the Band Structure Simulated is Shown in Figure 4.11 (a) inset…………………………. 87

4.13: (a) Band Structure of a 3 nm x 3 nm InAs Nanowire Band Structure along [100]. (b) Plot of Transition Probabilities under an applied electric field of (b) 10kV/cm, (c) 100 kV/cm and (d) 1 MV/cm for the First Three Bands at the Location Shown in the inset of Figure 4.12 (a)………………………………… 92

4.14: (a) Band Structure of a 3 nm x 3 nm Si Nanowire along the [100] Direction. (b) Plot of Transition Probabilities under an Applied Electric Field of (b) 1.0 kV/cm and (c) 100 kV/cm for the first four Bands at the Band Crossing Shown in the inset of (a)…………………………………………………………... 96

4.15: (a) Conduction Band Structure of 3 nm x 3 nm InAs Nanowire along [100]. (b) Conduction Band Structure of 3 nm x 3 nm InAs Nanowire along [111]. (c) Plot of Average Electron Kinetic Energies in 3 nm x 3 nm InAs Nanowires along [100] and [111] with and without Multi-band Drift. (d) Plot of Average Hole Kinetic Energies in 3 nm x 3 nm InAs Nanowires along [100] and [111] with and without Multi-band Drift…………………………………………... 97

4.16: (a) Conduction Band Structure of 3 nm x 3 nm Si Nanowire along the [111] Direction. (b) Valence Band Structure of 3 nm x 3 nm Si Nanowire along the [111] Direction. (c) Plot of Average Electron Kinetic Energies in 3 nm x 3 nm Si Nanowires along the [100] and [111] Directions with and without Multi-

Figure Page

band Drift. (d) Plot of Average Hole Kinetic Energies in 3 nm x 3 nm Si Nanowires along the [100] and [111] Directions with and without Multi-band Drift………………………………………………………………………... 100

4.17: Snapshot of Electrons in the Conduction Band of 3 nm x 3 nm InAs along [111] at the end of the Simulation without Multi-band Drift at 1MV/cm and 4MV/cm………………………………………………………………………… 102

4.18: Electron Drift Velocity of Si Nanowires along the [100] Direction Versus Electric Field for Different Nanowire Widths………………………………….. 104

4.19: Hole Drift Velocity of Si Nanowires along [100] Versus Electric Field for Different Nanowire Widths…………………………………………………….. 105

4.20: Electron Drift Velocity of GaAs Nanowires along [100] Versus Electric Field for Different Nanowire Widths…………………………………………………. 105

4.21: Hole Drift Velocity of GaAs Nanowires along [100] Versus Electric Field for Different Nanowire Widths…………………………………………………….. 106

5.1: Scattering Rates of a 2 nm x 2 nm InAs NW Compared with Bulk……………. 107

5.2: Carrier Chart for a 3 nm x 3 nm InAs NW with Excited Electrons…………….. 108

5.3: Energy Relaxation of Hot Electrons in Bulk InAs, 2 nm x 2 nm InAs NW [100] and 3 nm x 3 nm InAs NW [100]……………………………………… 109

5.4: Distribution Functions for Different Electric Fields on a 3 nm x 3 nm InAs NW [100]………………………………………………………………….. 109

5.5: The Supercell of a 2.0 nm x 2.0 nm In0.53Ga0.47As Nanowire along [100]

Figure Page

Cladded by 1.5 nm of InP…………………………………………………………. 111

5.6: 50 Supercells of a 2.0 nm x 2.0 nm In0.53Ga0.47As Nanowire along [100]

Cladded by 1.5 nm of InP…………………………………………………………. 112

5.7: The First 300 Conduction Bands of a 2.0 nm x 2.0 nm In0.53Ga0.47As

Nanowire along [100] with 1.5 nm InP Cladding………………………………. 113

5.8: The First 300 Conduction Bands of a 2.0 nm x 2.0 nm In0.53Ga0.47As

Nanowire along [100] with 0.5 nm InP Cladding………………………………. 113

5.9: Band Gap of In0.53Ga0.47As Nanowires along [100] with InP Cladding for

Different Wire and Cladding Thicknesses……………………………………… 114

5.10: Average Electron Energies for 2 nm x 2 nm In0.53Ga0.47As Nanowire

along [100] with Different Cladding Thicknesses……………………………… 115

5.11: Average Electron Energies for 3 nm x 3 nm In0.53Ga0.47As Nanowire along

[100] with Different Cladding Thicknesses…………………………………….. 115

5.12: Percentage of Carriers Undergoing Impact Ionization (Multiple Electron

Generation) as a Function of Excitation Energy for Different Nanowire

Claddings……………………………………………………………………….. 116

6.1: An Example Device Structure Showing the Division of the JNFET into Slabs

to Simplify the Computations…………………………………………………... 118

6.2: Band Structure for a 3 nm x 3 nm In0.7Ga0.3As Nanowire…………………… 119

6.3: Diagram Showing the Charge of the Carrier Distributed along the Atoms

Within a Poisson Well………………………………………………………….. 120

Figure Page

6.4: Probability Charge Density Across the Cross-Section of a Nanowire for a 3 nm x3 nm In0.7Ga0.3As Nanowire…………………………………………………… 121

6.5: Flowchart for the 1D Monte Carlo Method…………………………………….. 123

6.6: Transfer of a Carrier Moving from 1 slab to Another slab……………………... 124

6.7: Schematic Showing the Carrier Injection Algorithm…………………………... 127

6.8: Comparison of Subthreshold Swing (SS) of a JNFET using the Traditional Charge Neutrality Injection Method and the Surface Injection Method……….. 127

6.9: General JNFET Device Structure Simulated…………………………………… 128

6.10: ID-VD and ID-VG Curves for Different VG and VD Values Respectively….. 129

6.11: a) Plot of ID vs VG for Different gate Length JNFETs, b) Variation of Subthreshold Swing of the Nanowire JNFET Against its Device and gate Length……………………………………………………………………... 130

6.12: Schematic plot of a JNFET Showing the Paths a Carrier can take from the Point of Injection to Ejection…………………………………………………… 131

6.13: Plot of Total Carriers Passing Through the Drain that Underwent Different Number of Scattering Events, b) Ballistic Percentage as a Function of gate Length……………………………………………………………………... 132

1. INTRODUCTION

1.1. Emergence of Nanoscale Devices

The significant progress in integrated circuits (IC) technology over the past five decades has become the driving power of the semiconductor technology industry. A key factor of the progress in IC technology is the scaling down of the dimensions of each transistor, the basic element of integrated circuits, thereby increasing the total number of transistors in one IC chip. This increases the functionality of the chip while keeping its cost roughly constant. The device scaling has been successfully predicted by Moore's law (Moore1965) – the number of transistors on one IC chip has quadrupled every three years and the feature size of each transistor has shrunk to half of its original value at the same time. To date, microprocessors with 1.4 billion transistors have been realized, and the corresponding metal oxide semiconductor field effect transistor (MOSFET) gate lengths in modern chips has already entered the nanometer regime. The aggressive scaling of the device size has to be continued to maintain the successive improvements in circuit technology. Unfortunately, as the MOSFET gate length enters the nanometer regime, short channel effects (SCEs), such as drain induced barrier lowering (DIBL), gate induced drain leakage (GIDL), etc., have become increasingly significant, which limits the scaling capability of planar bulk or silicon on insulator (SOI) MOSFETs (Frank2001). For these reasons, novel device structures and materials including silicon nanowire

transistors (Cui2002), FinFETs (Choi2001), carbon nanotube FETs (Alvi2005), etc., are being explored by the industry as well as various academic departments.

Another problem that becomes prevalent as the channel length reduces is the control of the gate over the channel. Effective gate control is required for a nanoscale MOSFETs to achieve good device performance. For this reason, silicon nanowires, which allow multi-gate or gate all around transistors, are being explored. Wires with rectangular cross-sections are used to fabricate different types of tri gate/gate all around FETs. The nanowire transistor is one candidate which has the potential to overcome the problems caused by short channel effects in MOSFETs and has gained significant attention from both device and circuit developers. In addition to the effective suppression of short channel effects due to the improved gate control, the multi-gate nanowire FETs show good current values and increased mobilities under particular strain conditions and nanowire orientations. As a result, the nanowire transistor has obtained broad attention from both the semiconductor industry (Kotlyar2012) and academia (Colinge2009).

1.2. Simulation Methods for Nanoscale Structures

The study of charge transport in semiconductors is of fundamental importance both from the point of view of the basic physics and for its applications to electrical devices (Brews1980). As the need for electrical appliances grew the need for smaller and faster devices grew as well. This led to the reduction in the size of the devices. In recent

years nanowires have become important as both a novel material and as a channel for transistors. It is therefore very important to understand the material properties of nanowires and create models that can simulate transport in nanowires. Recent experimental work suggests that the growth of freestanding small diameter [110] Si NWs (<10nm) is thermodynamically favorable. Simulations also predict that the phonon limited hole mobility in these dimensionally reduced structures significantly exceed that of electrons. It is therefore important to have a simulation tool capable of accurate results on nanowire simulations.

There are several methods to solve transport in nanoscale devices. Methods using the traditional drift diffusion model is still popular due to the simplicity in its implementation. The drift diffusion method being a fundamentally classical method, requires external models to be added in order to simulate nanoscale devices. Models such as the self-consistent coupled Schrödinger Poisson model, effective potential model and the Bohm quantum potential model are regularly used to simulate nanoscale devices (Fiori2007). The band structure gets modified due to the confinement in nanoscale devices. This has to be incorporated into the drift diffusion model with modified effective masses. The mobility of the materials will also have to be changed due to the change in scattering rates of the confined systems. Unfortunately, the accuracy of such simulations are not good and often require extensive calibration to experimental data to be useful in analysis. Parameters are usually very difficult to obtain since the parameters change drastically based on the extent of confinement in these nanoscale devices.

A more rigorous approach used is the NEGF method (Datta1997). This is a fully quantum approach that is the most accurate theoretically, unfortunately, to simulate

realistic devices, including dissipative scattering is computationally prohibitive, and attempts at approximations of the method have unphysical results. There are several publications on nanowire FETs using the effective mass Schrödinger-Poisson solver coupled with NEGF method (Martinez2007, Dastjerdy2010, Wang2004). Though these simulations are able to capture phase breaking, tunneling and other quantum effects accurately, they have many drawbacks when simulating real device geometries. To add scattering into the Green's function approach requires a non-local self-energy scattering matrix. This matrix is very dense and therefore to simplify calculations scattering is assumed to be local, similar to a semi-classical Monte Carlo approach. Also dissipative scattering is usually ignored to further simplify the matrix, often approximating transport to being purely ballistic or close to ballistic (Martinez2007, Dastjerdy2010). Also to solve the Schrödinger equation, bulk effective masses are used which can be very different from the effective masses in nanowires (Horiguchi1996). At high energies, the band structure of nanowires is highly non-parabolic and very dense (Buin2008), considering a full band structure is essential to capture the transport in the high field regimes. Last but not least, the computational cost of 3D NEGF methods is very large and regularly requires simulations to be run on hundreds or thousands of processors.

In this thesis, the Monte Carlo method is employed to study transport in nanowires. Monte Carlo techniques are statistical numerical methods, which are applied to the simulation of random processes. In truth, the Monte Carlo method as a statistical numerical method was born well before its application to transport problems and has been applied to a number of scientific fields (Boyle1997). In the case of the charge transport, however, the solution of the Boltzmann transport equation is a direct simulation

of the dynamics of the carriers in the material. This means that while the simulation is being run, and while the solution is being approached, any physical information can be easily extracted. Therefore, even though the result of Monte Carlo simulations require a correct physical interpretation, the method is a very useful tool to achieve accurate solutions. It permits the simulation of particular physical situations unattainable in experiments, or even investigation of nonexistent materials in order to emphasize special features of the phenomenon under study. This use of the Monte Carlo technique makes it similar to an experimental technique and can be compared with analytically formulated theory. Although the Boltzmann transport equation does not incorporate quantum transport behavior, by modifying the Boltzmann transport equation to a purely 1D transport equation, with the confinement and charge distribution along the confined directions calculated in a fully quantum way, transport in long nanowires can be accurately simulated. In this work, the full band structure of nanowires are calculated using the $sp^3d^5s^*$ tight binding method including spin-orbit interaction (Boykin2004). The deformation potential scattering rates are calculated based on work done by Buin (2008) and extended to polar optical phonon, ionized impurity, impact ionization and surface roughness scattering rates are calculated within the tight binding basis. Using the same parameters that are used for bulk material simulations, the scattering rates of nanowires are also calculated. By coupling the particle based Monte Carlo to the tight binding band structure and scattering rate calculation in a self-consistent manner, dissipative transport in nanowire FETs is successfully simulated. By using a full band Monte Carlo simulation, transport at high energies, where scattering dominates and dissipative transport is important, can be accurately modeled. Compared to NEGF simulations where

hundreds or thousands of processors are required to run a simulation, all the simulations in this work are run on a single processor greatly reducing the computational cost in comparison. Therefore, due to the relatively low computational cost and the effective incorporation of dissipative scattering this work provides a very useful tool to simulate transport in nanowire structures.

In chapter 2, the calculation of the full band structure of nanowire devices is discussed with regard to the empirical tight binding method. The tight binding method, also used to calculate the band structure of the bulk method is used to obtain the band structure of the nanowire without any extra parameters.

In chapter 3, the scattering rates of nanowires and bulk materials are calculated within the tight binding basis. At high energies, the scattering rate of the nanowire material is shown to agree to the scattering rate of the bulk material for the same scattering rate parameters, an important property which allows the simulation of nanowire devices without any additional parameters.

In chapter 4, the low field and high field analysis of nanowires is performed. In the low-field regime, the Boltzmann transport equation is solved using Rode's method (Rode1972). The high field transport is analyzed using a uniform field Monte Carlo simulation. The scattering rate parameters for Si and GaAs are obtained by fitting the mobility and velocity field curves with experimentally obtained data. The same parameters are then used to simulate high field transport in nanowires. A new model to describe the interband tunneling process is also introduced. The importance of the model in simulating high field transport in nanowires is also discussed.

In chapter 5, the energy relaxation of excited electrons is studied in free standing nanowires as well as cladded nanowires, the multi-exciton generation process is also studied in cladded nanowires. In chapter 6, a full band particle based Monte Carlo simulator is used to study the current voltage properties of an $In_{0.7}Ga_{0.3}As$ junctionless nanowire field effect transistor (JNFET). Important modifications are made to the traditional Monte Carlo process to incorporate confinement effect in a fully quantum way in nanowires.

2. BAND STRUCTURE OF BULK AND NANOWIRE MATERIALS

The method used to calculate the band structure of nanowires is usually the same as the methods used to calculate the band structure of bulk materials. Since the focus of this work is on nanowires, the advantages and disadvantages of the methods used will be discussed with regard to the calculation of nanowire band structures. The calculation of the band structure of nanowire materials is essential to understanding the transport through these materials. There are various methods available to calculate the band structure of nanowires such as the plane-wave basis non local empirical pseudopotential method (EPM) (Chelikowsky1984), the empirical tight binding method (ETB) (Vogl1983) and the density functional theory (DFT) within the local density approximation (LDA) (Williamson2006). Though all the methods listed above solve the time-independent Schrödinger equation to obtain the band structure across the full Brillouin zone (BZ) they employ different approximations to the nature of the wave function. This translates to certain advantages and disadvantages to each method. The empirical pseudopotential method approximates the wave function as a summation of plane waves. Due to the extended nature of these waves, a cladding layer of several nanometers is usually required around the nanowire to accurately obtain the band structure of the nanowire. This makes the calculation computationally expensive although due to the nature of the method it requires relatively few parameters. The empirical tight binding method on the other hand assumes the wave function is a linear combination of atomic orbitals on each atom. In most cases a linear combination of the s, p, d and s^* orbitals are used to describe the wave function. Due to the highly localized nature of

these atomic orbitals, the surface can be considered to be passivated with hydrogen and therefore a fewer number of atoms are required in the calculation of the band structure. This makes the calculation relatively computationally inexpensive. Unfortunately, the energy interaction between the orbitals in the Hamiltonian are approximated to fitting parameters, which leads to a large number of fitting parameters due to the large number of different orbitals on each atom. Fitting band structures to experimental data using the empirical tight binding methods usually involve computationally expensive genetic algorithms (Klimeck2000). The density functional theory approach on the other hand uses a local density approximation to relax the nanowire structure to its closest energy minimum and is very computationally expensive compared to the EPM and the ETB methods. In this work, we use the empirical tight binding method to calculate the band structure of both bulk and nanowire materials using the same set of parameters fitted to experimental data available for bulk materials.

2.1. The Empirical Tight Binding Method

As mentioned before, the band structure of a system can be obtained by solving the time independent Schrödinger equation of the system given by equation (2.1)

$$H\psi = E\psi \tag{2.1}$$

where H is the Hamiltonian for the system, E are its eigenvalues and ψ are its eigenvectors or wave functions. Since the system represents a crystal structure, the wave functions of the system must be Bloch waves. Therefore

$$\psi(r+R) = e^{ikr}\psi(r) \tag{2.2}$$

where k is the wave vector. The tight binding approximation is to assume the Bloch function is a sum of atomic orbitals centered on the individual atoms. Based on this approximation, the solution $\psi(r)$ of the time independent Schrödinger equation given by equation (2.1) is written as

$$\psi_{\nu}(\mathbf{k},\mathbf{r}) = \frac{1}{\sqrt{N}} \sum_{n,m} c_{\nu}(\mathbf{k}) e^{i\mathbf{k}.\mathrm{R}_n} \varphi_m \left[\mathbf{r} - (\tau_m \pm n\mathbf{a}_m)\right] \tag{2.3}$$

where the summation over n indicates the summation over all unit cells in the crystal, m is the number of atoms in a unit cell, $\mathbf{a}_m$ is primitive lattice vector for atom m, ν is the band index, $\mathbf{k}$ is the wave vector, N is the number of unit cells in the crystal, τ_m is the location of orbital m within the unit cell, φ_m are the atomic orbitals and c_ν are the orthonormal expansion coefficients obtained from an eigenvalue solver when solving equation (2.1).

In diamond and zinc-blende materials the unit cell consists of 2 atoms. Assuming each atom contains the s-orbital which consists of 1 orbital, the p-orbital which consists of 3 orbitals (p_x, p_y, p_z), the d-orbital which consists of 5 orbitals $(d_{xz}, d_{yz}, d_{xy}, d_{z^2}, d_{x^2-y^2})$ and the s^*-orbital, an excited s-type orbital (was introduced to describe the conduction bands reasonable well (Vogl1983)), which consists of 1 orbital, each atom now contains 10 different atomic orbitals. By including the spin-orbit interaction, each orbital can either be spin-up or spin-down increasing the number of orbitals to 20 per atom. With 2 atoms per unit cell in most bulk materials, this makes the Hamiltonian size in equation (2.1) equal to 40 for bulk materials. This is still much lower

than empirical pseudopotential methods where the matrix size can be as high as 300 depending on the number of reciprocal lattice vectors chosen (Rieger1993).

Assuming the tight binding wave functions can be written as described in equation (2.3), inserting equation (2.3) in to equation (2.1) we obtain

$$H_k \mathrm{B}_k = \varepsilon_k \mathrm{S}_k \mathrm{B}_k \tag{2.4}$$

where $H_k = \int \psi_k^*(r) H \psi_k(r) d^3 r$, $S_k = \int \psi_k^*(r) \psi_k(r) d^3 r$ and B_k are the coefficients of the atomic orbitals. Equation (1.4) is a generalized eigenvalue problem and can be solved using mathematical libraries such as ARPACK (Lehoucq1997), SLEPc (Hernandez2005), etc. Since the wave functions described in equation (2.3) are not orthogonal, the overlap integral S_k cannot be approximated to an identity matrix. This greatly increases the computational burden of solving equation (2.4). To simplify this, a transformation called the Lowdin transformation is applied to equation (2.4) to reduce it from a generalized eigenvalue problem to a simple eigenvalue problem. The following steps are applied (Papaconstantopoulos1986)

$$Hb = \varepsilon S b \tag{2.5}$$

$$\left(S^{-\frac{1}{2}} H S^{-\frac{1}{2}} \right) \left(S^{\frac{1}{2}} b \right) = \varepsilon \left(S^{\frac{1}{2}} b \right) \tag{2.6}$$

$$H_1 b_1 = \varepsilon b_1 \tag{2.7}$$

where $H_1 = S^{-\frac{1}{2}} H S^{-\frac{1}{2}}$ and $b_1 = S^{\frac{1}{2}} b$. Therefore by modifying the wave function and Hamiltonian the generalized eigenvalue problem is reduced to a simple eigenvalue problem with the **same** eigenvalues. Of course this now creates a new problem, even

though the eigenvalues are the same, the eigenvectors or wave functions are different. The tight binding wave function shown in equation (2.3) is now a linear combination of Lowdin orbitals and not atomic orbitals as is usually erroneously mentioned in literature. Lowdin orbitals are more localized on an atom than atomic orbitals (like Gaussian or Slater type orbitals) but also have non-zero values on the neighboring atoms so as to satisfy the orthogonality condition (Lu2005). A common approximation is to assume that the Lowdin orbitals are similar to atomic orbitals and use either a Slater type orbital or Gaussian type orbital to represent the atomic orbital. These orbitals are in general not orthogonal to each other. The validity of this approximation is yet to be rigorously verified. The lack of a proper description of the wave functions makes it difficult to calculate the scattering rates as will be shown in chapter 3.

The band structures calculated using the ETB method for bulk Si, GaAs and InAs are shown in Figure 2.1 using the $sp^3d^5s^*$ empirical tight binding method including spin-orbit interaction. The tight binding parameters used are listed in Table 2.1 (Boykin2004).

Table 2.1: Parameter list for the $sp^3d^5s^*$ empirical tight binding method including spin-orbit interaction for GaAs, Si and InAs.

Parameter	GaAs	Si	InAs
a	5.6532	5.43	6.0583
E_{sa}	-8.063758	-2.15168	-5.9801
E_{pa}	3.126841	4.22925	3.5813
E_{sc}	-1.603222	-2.15168	0.3333
E_{pc}	4.745896	4.22925	6.4939
E_{s^*a}	21.930865	19.11650	17.8411
E_{s^*c}	23.630466	19.11650	17.8411
E_{da}	13.140998	13.78950	12.1954

E_{dc}	14.807586	13.78950	12.1954
$ss\sigma$	-1.798514	-1.95933	-1.4789
$s^*s^*\sigma$	-4.112848	-4.24135	-3.8514
$s_a^*s_c\sigma$	-1.688128	-1.52230	-2.1320
$s_as_c^*\sigma$	-1.258382	-1.52230	-1.2219
$s_ap_c\sigma$	3.116745	3.02562	2.3159
$s_cp_a\sigma$	2.776805	3.02562	2.8006
$s_a^*p_c\sigma$	1.635158	3.15565	2.6467
$s_c^*p_a\sigma$	3.381868	3.15565	1.9012
$s_ad_c\sigma$	-0.39647	-2.28485	-2.5828
$s_cd_a\sigma$	-2.151852	-2.28485	-2.4499
$s_a^*d_c\sigma$	-0.145161	-0.80993	-0.8497
$s_c^*d_a\sigma$	-0.810997	-0.80993	-0.8371
$pp\sigma$	4.034685	4.10364	4.1188
$pp\pi$	1.275446	-1.51801	-1.3687
$p_ad_c\sigma$	-1.478036	-1.35554	-2.1222
$p_cd_a\sigma$	-0.064809	-1.35554	-2.0584
$p_ad_c\pi$	1.830852	2.38479	1.5462
$p_cd_a\pi$	2.829426	2.38479	1.7106
$dd\sigma$	-1.216390	-1.68136	-1.2009
$dd\pi$	2.042009	2.58880	2.1820
$dd\delta$	-1.829113	-1.81400	-1.7788
λ_a	0.194174	0.01989	0.1763
λ_c	0.036594	0.01989	0.1248

The off-diagonal elements of the tight binding Hamiltonian is calculated using the two-center integral approximation given by Slater (1954) listed in Table 2.2 where l, m, n are the cosine of the angles along the x, y, z axes between the two atoms respectively.

Table 2.2: Two center integral formulae for the ETB method

$E_{s,s}$	$(ss\sigma)$
$E_{s,x}$	$l(sp\sigma)$

$$E_{x,x} \qquad l^2\left(pp\sigma\right)+\left(1-l^2\right)\left(pp\pi\right)$$

$$E_{x,y} \qquad lm\left(pp\sigma\right)-lm\left(pp\pi\right)$$

$$E_{x,z} \qquad ln\left(pp\sigma\right)-ln\left(pp\pi\right)$$

$$E_{s,xy} \qquad \sqrt{3}lm\left(sd\sigma\right)$$

$$E_{s,x^2-y^2} \qquad \sqrt{3}/2\left(l^2-m^2\right)\left(sd\sigma\right)$$

$$E_{s,3z^2-r^2} \qquad \left[n^2-1/2\left(l^2+m^2\right)\right]\left(sd\sigma\right)$$

$$E_{x,xy} \qquad \sqrt{3}l^2m\left(pd\sigma\right)+m\left(1-2l^2\right)\left(pd\pi\right)$$

$$E_{x,yz} \qquad \sqrt{3}lmn\left(pd\sigma\right)-2lmn\left(pd\pi\right)$$

$$E_{x,zx} \qquad \sqrt{3}l^2n\left(pd\sigma\right)+n\left(1-2l^2\right)\left(pd\pi\right)$$

$$E_{x,x^2-y^2} \qquad \sqrt{3}/2\,l\left(l^2-m^2\right)\left(pd\sigma\right)+l\left(1-l^2+m^2\right)\left(pd\pi\right)$$

$$E_{y,x^2-y^2} \qquad \sqrt{3}/2\,m\left(l^2-m^2\right)\left(pd\sigma\right)-m\left(1+l^2-m^2\right)\left(pd\pi\right)$$

$$E_{z,x^2-y^2} \qquad \sqrt{3}/2\,n\left(l^2-m^2\right)\left(pd\sigma\right)-n\left(l^2-m^2\right)\left(pd\pi\right)$$

$$E_{x,3z^2-r^2} \qquad l\left[n^2-1/2\left(l^2+m^2\right)\right]\left(pd\sigma\right)-\sqrt{3}ln^2\left(pd\pi\right)$$

$$E_{y,3z^2-r^2} \qquad m\left[n^2-1/2\left(l^2+m^2\right)\right]\left(pd\sigma\right)-\sqrt{3}mn^2\left(pd\pi\right)$$

$$E_{z,3z^2-r^2} \qquad n\left[n^2-1/2\left(l^2+m^2\right)\right]\left(pd\sigma\right)\sqrt{3}n\left(l^2+m^2\right)\left(pd\pi\right)$$

$$E_{xy,xy} \qquad 3l^2m^2\left(dd\sigma\right)+\left(l^2+m^2-4l^2m^2\right)\left(dd\pi\right)+\left(n^2+l^2m^2\right)\left(dd\delta\right)$$

$$E_{xy,yz} \qquad 3lm^2n\left(dd\sigma\right)+ln\left(1-4m^2\right)\left(dd\pi\right)+ln\left(m^2-1\right)\left(dd\delta\right)$$

$$E_{xy,yz} \qquad 3l^2mn\left(dd\sigma\right)+mn\left(1-4l^2\right)\left(dd\pi\right)+mn\left(l^2-1\right)\left(dd\delta\right)$$

$$E_{xy,x^2-y^2} \qquad 3/2\,lm\left(l^2-m^2\right)\left(dd\sigma\right)+2lm\left(m^2-l^2\right)\left(dd\pi\right)+1/2\,lm\left(l^2-m^2\right)\left(dd\delta\right)$$

$$E_{yz,x^2-y^2} \qquad 3/2\,mn\left(l^2-m^2\right)\left(dd\sigma\right)-mn\left[1+2\left(l^2-m^2\right)\right]\left(dd\pi\right)$$
$$+mn\left[1+1/2\left(l^2-m^2\right)\right]\left(dd\delta\right)$$

$$E_{zx,x^2-y^2} \qquad 3/2\,nl\left(l^2-m^2\right)\left(dd\sigma\right)+nl\left[1-2\left(l^2-m^2\right)\right]\left(dd\pi\right)$$
$$-nl\left[1-1/2\left(l^2-m^2\right)\right]\left(dd\delta\right)$$

$$E_{xy,3z^2-r^2} \qquad \sqrt{3}lm\left[n^2-1/2\left(l^2+m^2\right)\right]\left(dd\sigma\right)-2\sqrt{3}lmn^2\left(dd\pi\right)$$
$$+\sqrt{3}/2\,lm\left(1+n^2\right)\left(dd\delta\right)$$

$$E_{yz,3z^2-r^2} \qquad \sqrt{3}mn\left[n^2-1/2\left(l^2+m^2\right)\right]\left(dd\sigma\right)$$
$$+\sqrt{3}mn\left(l^2+m^2-n^2\right)\left(dd\pi\right)-\sqrt{3}/2\,mn\left(l^2+m^2\right)\left(dd\delta\right)$$

$E_{zx,3z^2-r^2}$	$\sqrt{3}ln\left[n^2-1/2\left(l^2+m^2\right)\right](dd\sigma)$ $+\sqrt{3}ln\left(l^2+m^2-n^2\right)(dd\pi)-\sqrt{3}/2\,ln\left(l^2+m^2\right)(dd\delta)$
$E_{x^2-y^2,x^2-y^2}$	$3/4\left(l^2-m^2\right)^2(dd\sigma)+\left[l^2+m^2-\left(l^2-m^2\right)^2\right](dd\pi)$ $+\left[n^2+1/2\left(l^2-m^2\right)^2\right](dd\delta)$
$E_{x^2-y^2,3z^2-r^2}$	$1/2\left(l^2-m^2\right)\left[n^2-1/2\left(l^2+m^2\right)\right](dd\sigma)$ $+\sqrt{3}n^2\left(m^2-l^2\right)(dd\pi)+\sqrt{3}/4\left(1+n^2\right)\left(l^2-m^2\right)(dd\delta)$
$E_{3z^2-r^2,3z^2-r^2}$	$\left[n^2-1/2\left(l^2+m^2\right)\right]^2(dd\sigma)+3n^2\left(l^2+m^2\right)(dd\pi)+3/4\left(l^2+m^2\right)^2(dd\delta)$

The primitive unit cell as well as its next nearest neighbors that are used for GaAs are shown in Figure 2.2. The solid circles represent the atoms in the primitive unit cell while the hollow circles are the nearest neighbors connected to the primitive unit cell atoms by dotted lines. Red circles represent the Ga while the blue circles represent As. Each atom contains one neighbor that exists within the same primitive cell and 3 other neighbors that are in 3 different primitive cells obtained by translational shifts according to the basis vectors as shown in the figure.

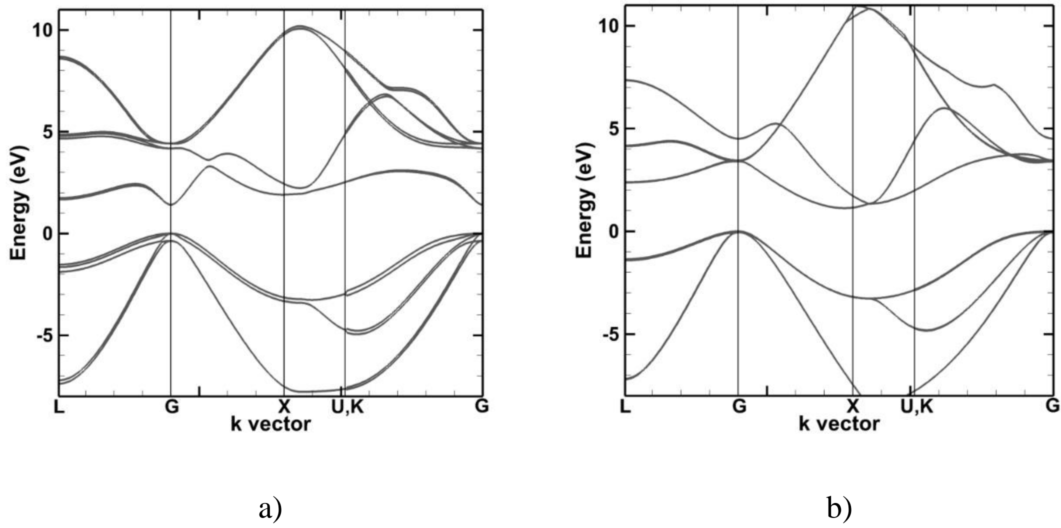

a) b)

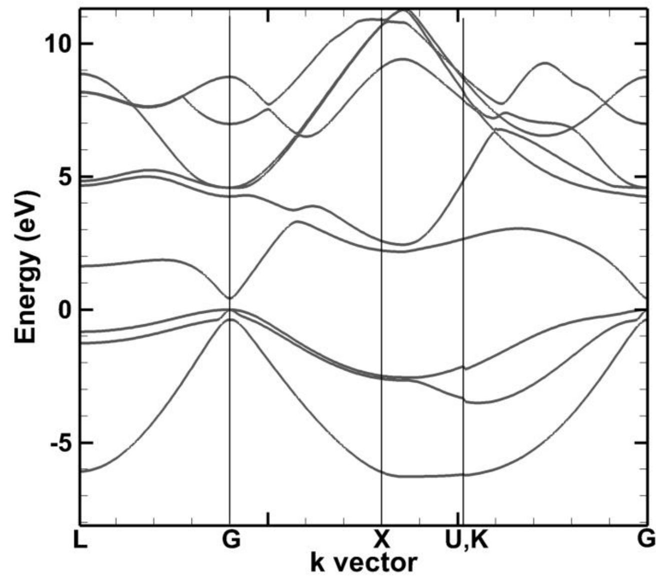

c)

Figure 2.1: Bulk band structures of a) GaAs, b) Si and c) InAs along important symmetry directions in the 1st Brillouin Zone using the empirical tight binding method.

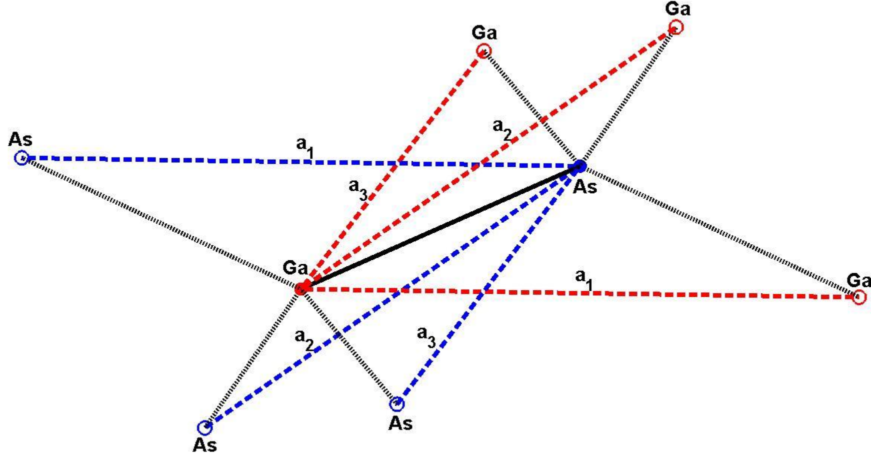

Figure 2.2: Primitive cell structure of GaAs. Red circles indicate Gallium atoms while blue circles indicate Arsenide atoms. Solid lines represent bonds. Solid circles are atoms in the primitive unit cell, while hollow circles are nearest neighbor atoms obtained by translational shifts according to the basis vectors $\mathbf{a_1}$, $\mathbf{a_2}$ and $\mathbf{a_3}$.

The parameters listed in Table 2.1 are obtained by fitting important points in the band structure such as band gaps and effective masses to the available experimental data of the bulk materials (Vurgaftman2001).

2.2. Band Structure of Nanowires

For the case of nanowires, equation (2.3) can be written as

$$\psi_{\nu}\left(k,\mathbf{r}\right)=\frac{1}{\sqrt{N}}\sum_{n,m}c_{\nu}\left(k\right)e^{ikna_l}\varphi_m\left[\mathbf{r}-\left(\tau_m\pm na_l\right)\right] \quad (2.8)$$

where the summation over n indicates the summation is over all supercells in the nanowire, a_l is the NW lattice constant, ν is the band index, k is the wave vector along the NW axis, N is the number of supercells, m is the orbital type and location, τ_m is the location of orbital m within the supercell, φ_m are the atomic orbitals and c_ν are the expansion coefficients obtained from an eigenvalue solver. The key difference between equations (2.3) and (2.8) is that in the case of nanowires, the momentum exists only along the nanowire axis. The main difference in the calculation of the band structure of nanowires is the creation of the supercell as opposed to the use of the primitive cell in bulk band structure calculations. Due to the confinement along two directions, the supercell can be very large and contains many primitive cells of the bulk material. This makes the matrix in equation (1) very large and the solution of the eigenvalue problem computationally expensive for large nanowire widths/diameters.

2.2.1. Supercell Creation

The supercell of a nanowire is the smallest cell of atoms that when replicated along the axis of the nanowire produces the entire nanowire. The supercell of a nanowire depends on the cross-sectional profile of the nanowire as well as its orientation. Once the orientation of the nanowire is defined, the primitive basis vectors of the material are used to calculate its periodicity along its axis. If the orientation of the nanowire is different from the [100] the primitive basis vectors are first rotated to the defined nanowire orientation. The position of any atom can then be obtained by the following equation

$$\vec{T} = n_1\vec{a_1} + n_2\vec{a_2} + n_3\overleftarrow{a_3} \quad (2.9)$$

where n_1, n_2, n_3 are natural numbers and $\vec{a_1}, \vec{a_2}, \vec{a_3}$ are the rotated primitive basis vectors for the given material. The atoms in the nanowire are populated according to equation (2.9), where the neighbor of each atom is obtained by adding or subtracting a primitive vector. The dimensions along the confined directions are restricted according to the cross-section of the nanowire. Once the nanowire is sufficiently populated, the periodicity along the nanowire axis can be calculated. This also automatically gives the supercell of the nanowire. An example of a supercell structure for different cases is shown in Figures 2.3 and 2.4.

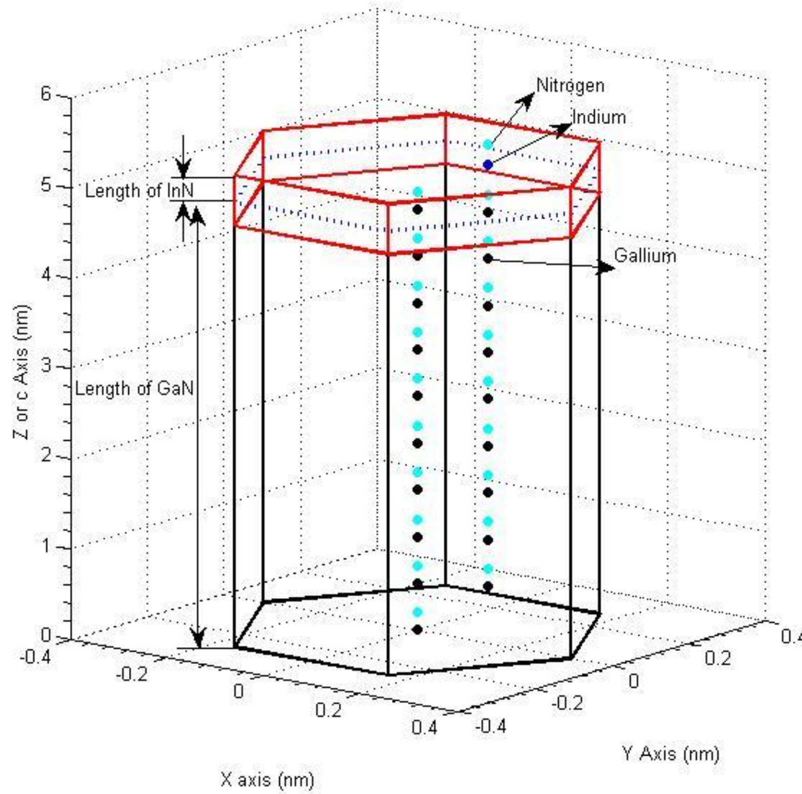

Figure 2.3: The supercell structure for a Wurtzite GaN-InN superlattice (Zhou2013).

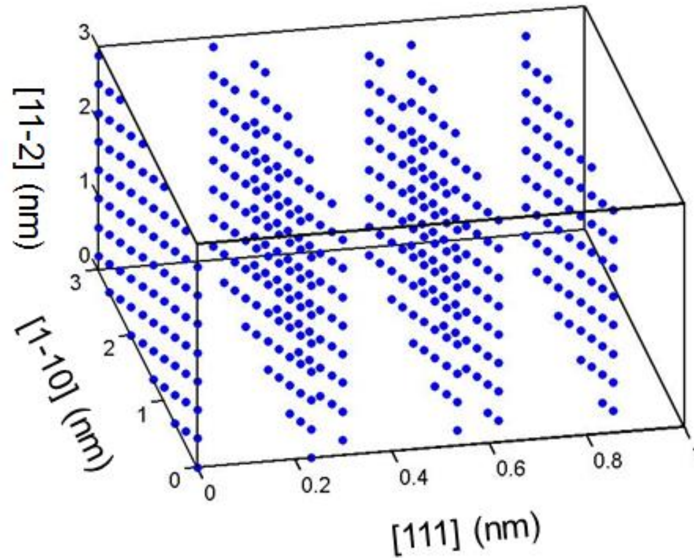

Figure 2.4: The supercell structure for a Zinc Blende 3 nm x 3 nm Si NW along [111].

2.2.2. Surface Passivation

In supercells which contain quantization, there are directions along which there is no periodicity. Therefore there exists atom within the supercell which don't have all their bonds satisfied. This creates dangling bonds which must be addressed, otherwise the band gap becomes filled with surface states and the band structure is modified. A common method to address this is to introduce artificial periodicity in to the system or by using a buffer layer around the nanowire. In most cases, the buffer layer must be very thick to completely remove the effect of the surface layer on the band structure. This greatly increases the computational cost as now the Hamiltonian of the entire system including the buffer layer has to be inverted as opposed to just the nanowire. A more commonly used method is the sp^3 hybridization method (Lee2004). This method to some degree, mimics the physical passivation of the dangling bonds with other atoms such as hydrogen

or oxygen. The energies of the bonding and antibonding states of SiH_4 for example are 18 eV and 5 eV below the valence band edge of bulk Si, respectively (Cardona1983). The sp^3 hybridization method is the approximation of the bonding and antibonding states between vacuum and a dangling bond at an energy determined by δ_{sp^3}. As an example of how particular bonds at the surface can be passivated, take for example a simple sp^3 system.

$$D = \begin{pmatrix} \varepsilon_s & 0 & 0 & 0 \\ 0 & \varepsilon_p & 0 & 0 \\ 0 & 0 & \varepsilon_p & 0 \\ 0 & 0 & 0 & \varepsilon_p \end{pmatrix} \tag{2.10}$$

$$V = \begin{pmatrix} 1 & 1 & 1 & 1 \\ 1 & -1 & -1 & 1 \\ 1 & 1 & -1 & -1 \\ 1 & -1 & 1 & -1 \end{pmatrix} \tag{2.11}$$

Here D represents the on-site energy for the system and V is the combination of s, p_x, p_y and p_z orbitals that represent the different possible bonds in a Zinc Blende system. The on-site energies are first converted to the sp^3 basis by

$$D^{new} = [V][D][V^T] \tag{2.12}$$

Then depending on which bond is dangling the on-site energy is decreased (the diagonal elements are increased by δ_{sp^3}) and then the system is rotated back to the original s, p_x, p_y and p_z orbital basis and added to the TB Hamiltonian as shown below

$$D = [V^T][D^{new_mod}][V] \tag{2.12}$$

The effect of the dangling bond energy (δ_{sp^3}) on the band gap of a 5 nm x 5 nm GaAs NW is shown in Figure 2.5. As the sp^3 hybridization parameter is increased, the surface states are removed from the mid gap and the band gap of the material converges to a fixed value.

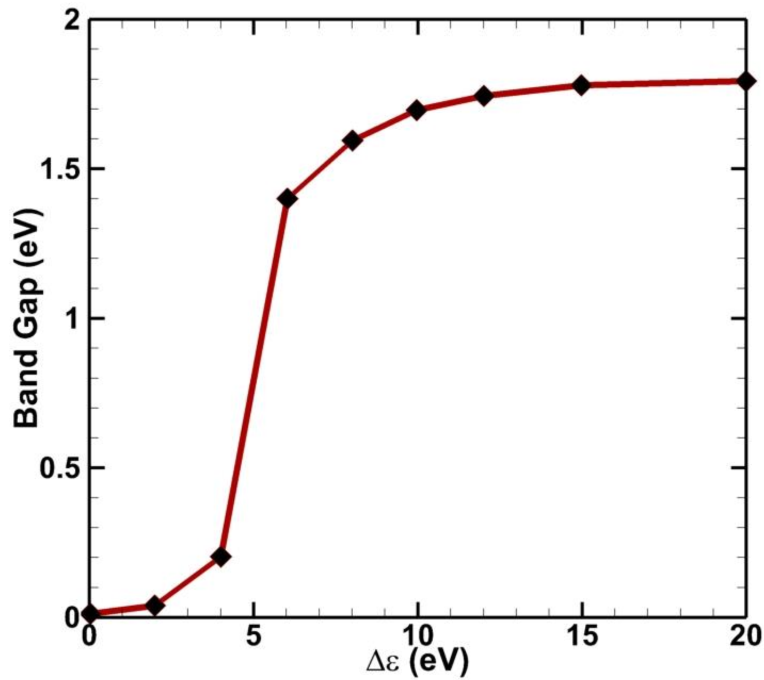

Figure 2.5: Variation of the band gap obtained using the sp^3 hybridization method with the sp^3 $(\Delta\varepsilon)$ hybridization energy parameter.

2.2.3. Band Structures of Si and InAs Nanowires

Once the Tight Binding Hamiltonian is set up, the energy band structure of the nanowire can be calculated for every k-point along the BZ ($-\pi / a$ to $+\pi / a$) where a is

the periodicity of the nanowire along the transport direction. The band structures are shown in Figure 2.6.

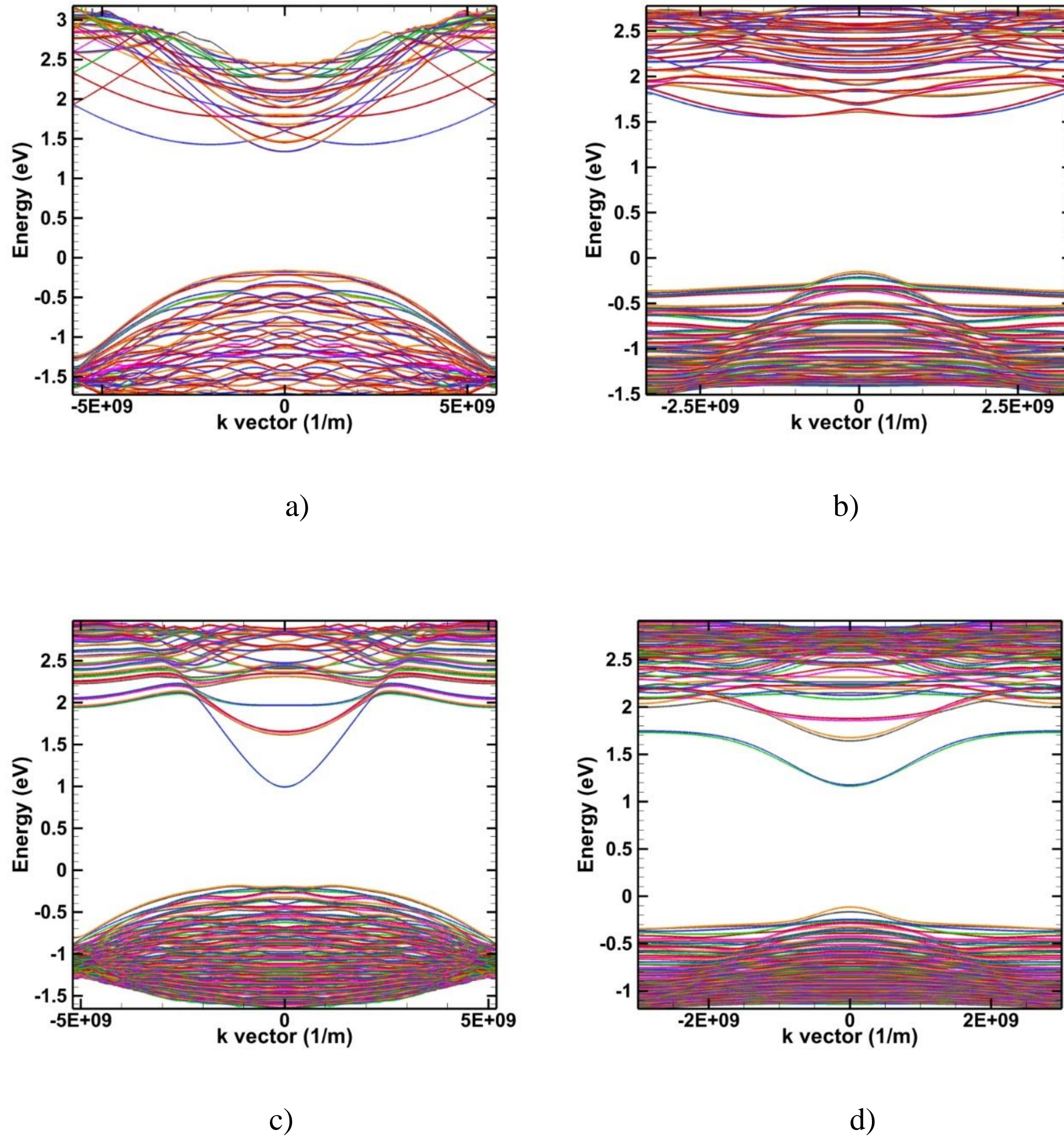

Figure 2.6: Band structure of a) 3 nm x 3 nm Si nanowire along [100], b) 3 nm x 3 nm Si nanowire along [111], c) 3 nm x 3 nm InAs nanowire along [100] and d) 3 nm x 3 nm InAs nanowire along [111] using the empirical tight binding method.

In most eigenvalue solvers, a reference energy is required and the closest say 100 bands with respect to the reference energy value is calculated. As the energy bands and eigenvectors for different k points are calculated, the energy reference has to be accordingly shifted, otherwise it is possible some valence band states will be obtained if the reference energy is too low. A simple method to ensure that you are always calculating the conduction or valence bands exclusively is to make the reference energy follow the equation

$$E_{ref}\left(i\right)=\begin{cases}\dfrac{E_{\max}\left(i-1\right)-E_{\min}\left(i-1\right)}{2}-0.2 & for\,conduction\,bands\\ \dfrac{E_{\min}\left(i-1\right)-E_{\max}\left(i-1\right)}{2}+0.2 & for\,valence\,bands\end{cases} \tag{2.13}$$

for successive k points. This way the reference energy is always in the middle of the span of energy bands you would require. The downside is that for the first k point the reference energy needs to be input separately. This requires a rough idea of the magnitude of the bandgap of the nanowire. The variation of the band gap with nanowire width is shown for Si, GaAs and InAs in Figure 2.7.

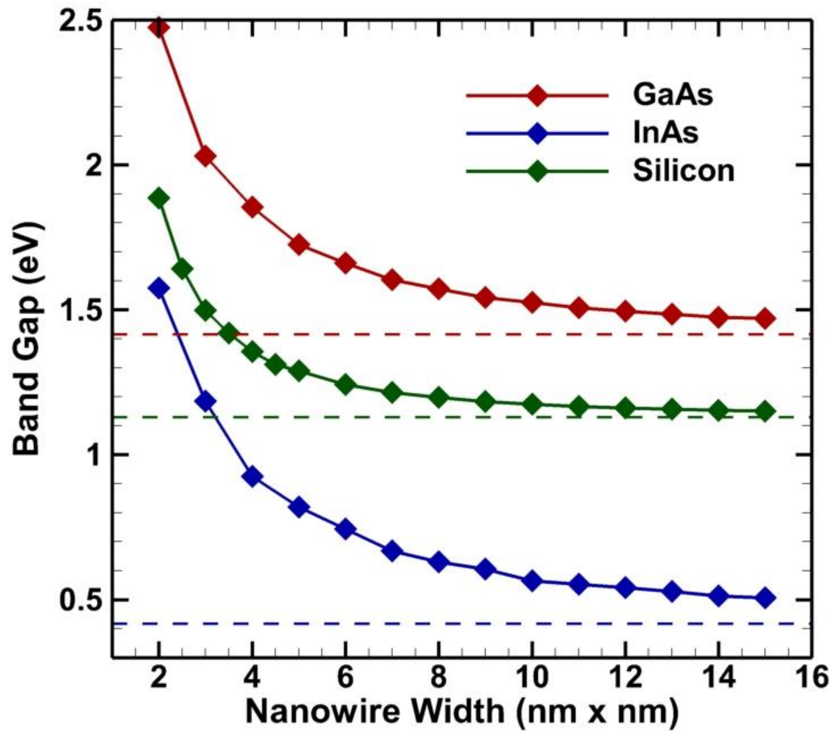

Figure 2.7: Variation of band gaps of Si, GaAs and InAs nanowires with nanowire widths

2.2.4. Eigenvalue Solver

The super cell structure of nanowires is fairly big even for small dimension nanowires. The super cell of a 3 nm x 3 nm Silicon nanowire along the [111] direction (shown in Fig. 2.4) contains 448 Silicon atoms. Using the $sp^3d^5s^*$ nearest neighbor ETB method including spin means that each atom will have 20 orbitals. Therefore the matrix size for this system will be 8960 x 8960. Inverting such a huge matrix for every k point in the Brillouin Zone (BZ) is prohibitively expensive. In this work the banded eigenvalue solver from ARPACK and the sparse eigenvalue solver from SLEPc are used to solve the

matrices. Only a few eigenvalues (~100) and their corresponding eigenvectors are calculated. To improve the efficiency of the banded eigenvalue solver, the bandwidth of the Tight Binding Hamiltonian is reduced using a reverse Cuthill Mckee algorithm (Crane1976). An example is shown in Fig 2.8.

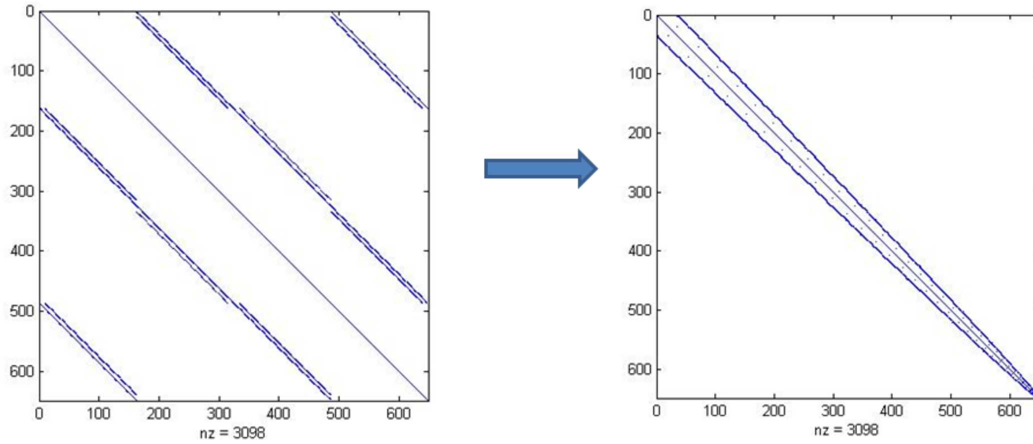

Figure 2.8: The reduction in the bandwidth of a matrix using a reverse Cuthill Mckee algorithm.

2.2.5. Density of States

The density of states of nanowire and bulk materials is given by the following equations

$$DOS_{1D}(E) = \frac{e}{2\pi A}\int \frac{\partial k}{\partial E'}\delta(E-E')dE' \qquad (2.14)$$

$$DOS_{3D}(E) = \frac{e}{8\pi^3}\int \frac{\partial k}{\partial E'}\delta(E-E')dE' \quad (2.15)$$

where A is the cross-sectional area of the nanowire. The comparison between the DOS of a 3 nm x 3 nm $In_{0.7}Ga_{0.3}As$ NW along [100] and bulk $In_{0.7}Ga_{0.3}As$ and the DOS of a 3 nm x 3 nm Si NW along [100] and bulk Si is shown in Figures 2.9.

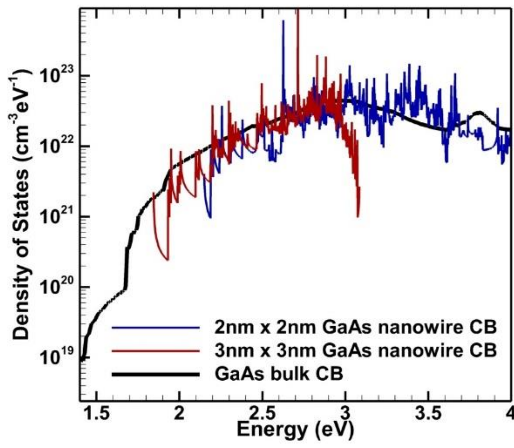

a)

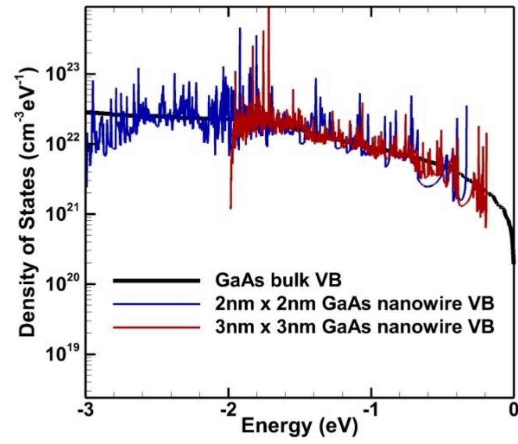

b)

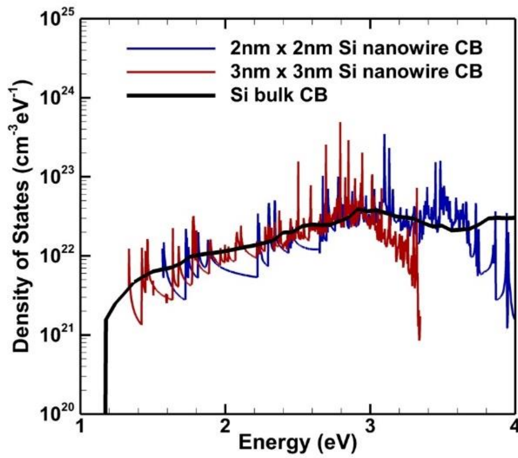

c)

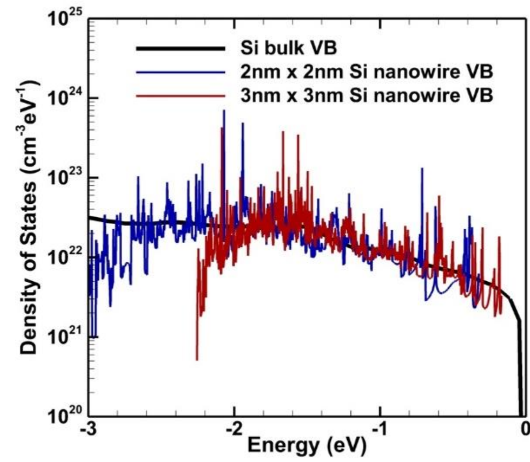

d)

Figure 2.9: Comparison of density of states between bulk and nanowire materials using the same tight binding parameters. a) conduction bands of 2 nm x 2 nm and 3 nm x 3 nm GaAs nanowires along [100], b) valence bands of 2 nm x 2 nm and 3 nm x 3 nm GaAs nanowires along [100], c) conduction bands of 2 nm x 2 nm and 3 nm x 3 nm Si nanowires along [100] and d) valence bands of 2 nm x 2 nm and 3 nm x 3 nm Si nanowires along [100].

At high energy it is observed that the density of states of the nanowire oscillate around the density of states of the bulk material. This can be understood by the fact that at high energies, the carriers are less confined and should have confinement free (bulk-like) behavior.

3. SCATTERING RATES OF BULK AND NANOWIRE MATERIALS

3.1. Tight Binding Scattering Rates of Bulk Materials

The scattering rates of the bulk material within the tight binding scheme are calculated using Fermi's golden rule

$$W_{\mu,\nu}(\mathbf{k},\mathbf{k}') = \frac{2\pi}{\hbar}\left|V_{\mathbf{k},\mathbf{k}'}\right|^2 \delta\left(E_{\nu,\mathbf{k}'} - E_{\mu,\mathbf{k}} \pm \hbar\omega\right) \tag{3.1}$$

where $\mathbf{k}$ and $\mathbf{k}'$ are the initial and final wave vectors at band indices μ and ν respectively. $V_{\mathbf{k},\mathbf{k}'}$ is the matrix element for the particular scattering mechanism, $E_{\mu,\mathbf{k}}$ and $E_{\nu,\mathbf{k}'}$ are the initial and final energy states respectively and ω is the phonon frequency if present in the scattering mechanism. The Dirac delta function in equation (3.1) represents the energy conservation property of the scattering process. The scattering rate from $\mathbf{k}$ to $\mathbf{k}'$ for a particular phonon vector $\mathbf{q}$ for the case of deformation potential scattering can be written as (Fischetti1988)

$$\begin{aligned} W_{\mu,\nu}(\mathbf{k},\mathbf{k}',\mathbf{q}) = \frac{2\pi}{\hbar}\left|\left\langle \psi_\nu(\mathbf{k}'), N_{|\mathbf{q}|} + \frac{1}{2} \pm \frac{1}{2}\left|H_{\mathbf{q},e-ph}\right|\psi_\mu(\mathbf{k}), N_{|\mathbf{q}|}\right\rangle\right|^2 \\ \times\,\delta\left(E_\nu(\mathbf{k}') - E_\mu(\mathbf{k}) \pm \hbar\omega(|\mathbf{q}|)\right) \end{aligned} \tag{3.2}$$

where $\mathbf{k}$ and $\mathbf{k}'$ are the initial and final wave vectors at band indices μ and ν respectively, $N_{|\mathbf{q}|}$ is the equilibrium phonon occupation number, $\psi_\nu(\mathbf{k}')$ and $\psi_\mu(\mathbf{k})$ are the final and initial wave functions respectively. The matrix element in equation (3.2) is given by

$$V_{\mathbf{kk}'} = E_a \left[\frac{\hbar}{2\rho V \omega(|\mathbf{q}|)} \right]^{1/2} \left(N_{|\mathbf{q}|} + \frac{1}{2} \pm \frac{1}{2} \right)^{1/2} \int_{\mathbf{r}} \psi_\nu^*(\mathbf{k}') e^{i\mathbf{q}.\mathbf{r}} \psi_\mu(\mathbf{k}) d\mathbf{r} \tag{3.3}$$

where E_a is the deformation potential constant whose value is $E_{ac}|\mathbf{q}|$ for acoustic phonons and E_{op} for optical phonons, ρ is the crystal density and V is the crystal volume. The integration in equation (3.3) can be calculated using equation (2.3) to give

$$\int_{\mathbf{r}} \psi_\nu^*(\mathbf{k}') e^{i\mathbf{q}.\mathbf{r}} \psi_\mu(\mathbf{k}) d\mathbf{r} = \sum_{m,m'} C_{\mu,m}(\mathbf{k}) C_{\nu,m'}^*(\mathbf{k}') \sum_{n,n'} \frac{1}{N} e^{-i\mathbf{k}'.R_{n'}} e^{i\mathbf{k}.R_n} I_{m,m',n,n'}(\mathbf{q}) \tag{3.4}$$

where

$$I_{m,m',n,n'}(\mathbf{q}) = \int_{\mathbf{r}} \phi_{m'}^* \left[\mathbf{r} - (\tau_{m'} \pm n'\mathbf{a}_{m'}) \right] e^{i\mathbf{q}.\mathbf{r}} \phi_m \left[\mathbf{r} - (\tau_m \pm n\mathbf{a}_m) \right] d\mathbf{r} \tag{3.5}$$

Solving equation (3.5) is difficult given that the exact spatial variation of the atomic orbitals are unknown other than the fact that they are highly localized around the atom. At this point several approximations will be made to simplify equation (3.5). The first approximation is that neighboring unit cells within the tight binding scheme have very little overlap, mathematically this translates to $n = n'$. The summation involving n and n' can then be approximated to

$$\sum_{n,n'} \frac{1}{N} e^{-i\mathbf{k}'.R_{n'}} e^{i\mathbf{k}.R_n} = \sum_n \frac{1}{N} e^{i(\mathbf{k}-\mathbf{k}'+\mathbf{q})n\mathbf{a}} = \delta[\mathbf{k} - \mathbf{k}' + \mathbf{q}] \tag{3.6}$$

where $R_n = n\mathbf{a}$ and the discrete points $e^{i\mathbf{q}n\mathbf{a}}$ is taken from the continuous function $e^{i\mathbf{q}.\mathbf{r}}$. The Kronecker delta function in equation (3.6) guarantees the momentum conservation of the scattering process. Another important approximation to equation (3.5) is to assume that the overlap integral between: (i) orbitals on different atoms and (ii) different types of

orbitals on the same atom is zero. This is a valid approximation if the span of the orbital m is much less than $2\pi/|\mathbf{q}|$ which is true for small $\mathbf{q}$ (Buin2008). Using the above approximation, the overlap integral becomes

$$I_{m,n}(\mathbf{q}) = \int_{\mathbf{r}} \phi_m^*\left[\mathbf{r}-(\tau_m)\right] e^{i\mathbf{q}.\mathbf{r}} \phi_m\left[\mathbf{r}-(\tau_m)\right] d\mathbf{r} = e^{i\mathbf{q}.\tau_m} \tag{3.7}$$

The matrix element can now be written as,

$$\begin{aligned} V_{\mathbf{kk}'} = E_a \left[\frac{\hbar}{2\rho V \omega(|\mathbf{q}|)}\right]^{1/2} \left(N_{|\mathbf{q}|} + \frac{1}{2} \pm \frac{1}{2}\right)^{1/2} \\ \times \sum_m C_{\mu,m}(\mathbf{k}) C_{\nu,m}^*(\mathbf{k}') e^{i\mathbf{q}.\tau_m} \delta\left[\mathbf{k}-\mathbf{k}'+\mathbf{q}\right] \end{aligned} \tag{3.8}$$

The scattering rate from $\mathbf{k}$ to $\mathbf{k}'$ is then given by

$$W_{\mu,\nu}(\mathbf{k},\mathbf{k}') = \sum_{\mathbf{q}} W_{\mu,\nu}(\mathbf{k},\mathbf{k}',\mathbf{q}) = \sum_{\mathbf{q}} \frac{2\pi}{\hbar} |V_{\mathbf{kk}'}|^2 \delta\left(E_\nu(\mathbf{k}') - E_\mu(\mathbf{k}) \pm \hbar\omega(|\mathbf{q}|)\right) \tag{3.9}$$

Inserting equation (3.8) in to equation (3.9) we get

$$\begin{aligned} W_{\mu,\nu}(\mathbf{k},\mathbf{k}') = \frac{2\pi}{\hbar} E_a^2 \left[\frac{\hbar}{2\rho V \omega(|\mathbf{q}|)}\right] \left(N_{|\mathbf{q}|} + \frac{1}{2} \pm \frac{1}{2}\right) \left|S_{\mu,\nu}(\mathbf{k},\mathbf{k}')\right|^2 \\ \times \delta\left(E_\nu(\mathbf{k}') - E_\mu(\mathbf{k}) \pm \hbar\omega(|\mathbf{q}|)\right) \end{aligned} \tag{3.10}$$

where

$$S_{\mu,\nu}(\mathbf{k},\mathbf{k}') = \sum_m C_{\mu,m}(\mathbf{k}) C_{\nu,m}^*(\mathbf{k}') e^{i\mathbf{q}.\tau_m} \tag{3.11}$$

The scattering rate to a volume of k-space around $\mathbf{k}'$ is obtained by summing over a region of k-space around $\mathbf{k}'$ to obtain,

$$W_{\mu,\nu}(\mathbf{k},\Delta\mathbf{k}') = \sum_{\Delta\mathbf{k}'} W_{\mu,\nu}(\mathbf{k},\mathbf{k}') = \frac{E_a^2}{8\pi^2\hbar}\left[\frac{\hbar}{\rho\omega(|\mathbf{q}|)}\right]\left(N_{|\mathbf{q}|} + \frac{1}{2} \pm \frac{1}{2}\right) \times \left|S_{\mu,\nu}(\mathbf{k},\mathbf{k}')\right|^2 DOS(\mathbf{k}') \tag{3.12}$$

where

$$DOS(\mathbf{k}') = \int_{\mathbf{s}} \frac{\partial k'}{\partial E} d\mathbf{s} \tag{3.13}$$

where $\mathbf{s}$ is the constant energy surface within $\Delta\mathbf{k}'$ given by the energy conserving delta function in equation (3.9). Assuming dispersionless optical phonons and a linear dispersion and the equipartition approximation for acoustic phonons we get

$$W_{\mu,\nu,op}(\mathbf{k},\mathbf{k}') = \frac{E_{op}^2}{8\pi^2}\left[\frac{1}{\rho\omega_{op}}\right]\left(N_{|\mathbf{q},op|} + \frac{1}{2} \pm \frac{1}{2}\right)\left|S_{\mu,\nu}(\mathbf{k},\mathbf{k}')\right|^2 DOS(\mathbf{k}') \tag{3.14}$$

and

$$W_{\mu,\nu,\mathrm{ac}}(\mathbf{k},\mathbf{k}') = \frac{E_{ac}^2}{8\pi^2\hbar}\left[\frac{kT}{\rho v_s^2}\right]\left|S_{\mu,\nu}(\mathbf{q})\right|^2 DOS(\mathbf{k}') \tag{3.15}$$

where $\mathbf{q} = \mathbf{k} - \mathbf{k}'$. Using a similar derivation for polar optical phonon scattering, the scattering rate from $\mathbf{k}$ to $\Delta\mathbf{k}'$ is

$$W_{\mu,\nu,pop}(\mathbf{k},\mathbf{k}') = \frac{\omega_{op}e^2}{8\pi}\left[\frac{1}{\varepsilon_\infty} - \frac{1}{\varepsilon_0}\right]\left(N_{|\mathbf{q},op|} + \frac{1}{2} \pm \frac{1}{2}\right)\left|S_{\mu,\nu}(\mathbf{k},\mathbf{k}')\right|^2 DOS(\mathbf{k}') \tag{3.16}$$

The scattering rates obtained using the tight binding basis is similar to those obtained using the empirical pseudopotential method (EPM) except for the overlap integral (Saraniti2008). Recent studies have shed light on the nature of the tight binding atomic orbitals described in equation (2.8) (Lu2005). In addition to the orbitals being highly localized around an atom, a property regularly taken advantage of, the atomic orbitals are

also localized on the neighboring atoms and have the opposite value on the neighboring atoms. This seems to arise due to the necessity of the atomic orbitals to be orthonormal. This can be taken into account in the overlap integral in equation (3.4). Assuming nearest neighbor localizations in the calculation of the overlap integral, equation (3.4) can be written as

$$S_{\mu,\nu}\left(\mathbf{k},\mathbf{k}'\right) = \sum_{m} P_{\mu,\nu,m}\left(\mathbf{k},\mathbf{k}'\right) e^{i\mathbf{q}\cdot\tau_m} \tag{3.17}$$

where

$$\begin{aligned} P_{\mu,\nu,m}\left(\mathbf{k},\mathbf{k}'\right) &= C_{\mu,m}\left(\mathbf{k}\right) C^*_{\nu,\mathrm{m}}\left(\mathbf{k}'\right) + \\ &F \sum_{m_{neigh}} \left[C_{\mu,m}\left(\mathbf{k}\right) C^*_{\nu,\mathrm{m}_{neigh}}\left(\mathbf{k}'\right) e^{i\mathbf{k}'\mathbf{a}_{vec}} + C_{\nu,\mathrm{m}_{neigh}}\left(\mathbf{k}\right) C^*_{\mu,\mathrm{m}}\left(\mathbf{k}'\right) e^{-i\mathbf{k}\mathbf{a}_{vec}} \right] \end{aligned} \tag{3.18}$$

where m_{neigh} is summed over all nearest neighbors of m and would depend on the crystal structure, F is the fraction of the net atomic orbital, that is centered at atom m, present on its neighboring atom m_{neigh} and $\mathbf{a}_{vec}$ is the vector that translates the primitive cell containing atom m to the primitive cell containing atom m_{neigh}. The orbitals are still assumed to be highly localized to the atom and its neighbor as shown in Figure (3.1).

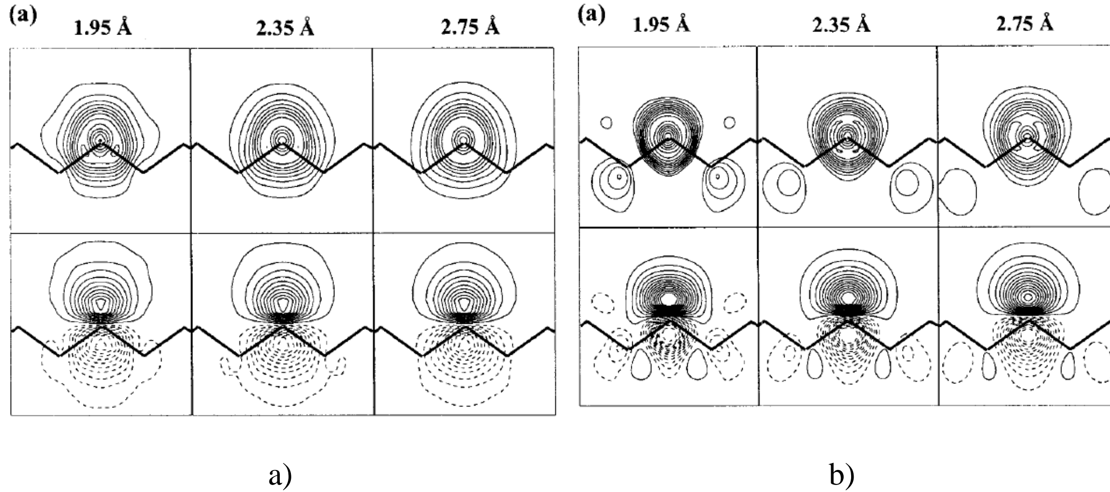

a) b)

Figure 3.1: a) Non-orthogonal and b) orthogonal s- and p- like quasi-atomic minimal basis orbitals in Si for different bond lengths in the (110) plane (Lu2005).

In the case of bulk Si or GaAs, out of the four neighboring atoms, one neighboring atom will always exist in the same primitive cell as the atom m causing $\mathbf{a}_{vec}$ to be zero. The other three neighboring atoms each have $\mathbf{a}_{vec}$ as one of the three primitive basis vectors of the Diamond and Zinc Blende crystal structure respectively. As can be seen in Figure (3.2), even a small value for the fraction F has a significant increase in the polar optical phonon scattering and non-polar optical phonon scattering rates at low energies in GaAs.

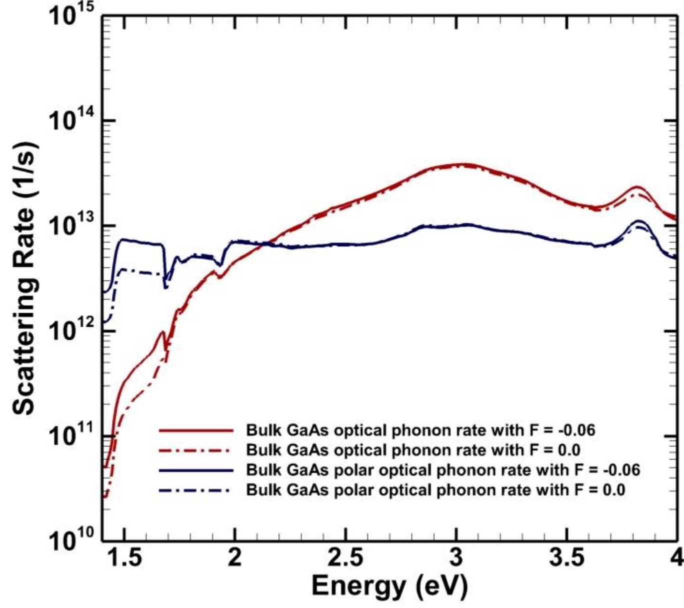

Figure 3.2: Bulk GaAs non-polar and polar optical phonon scattering rates for a neighboring factor of F = 0.0 and F = -0.06.

3.2. Tight Binding Scattering Rates of Nanowires

The scattering rates for nanowires are also calculated using Fermi's golden rule.

$$W_{\mu,\nu}(k,k') = \frac{2\pi}{\hbar}|V_{k,k'}|^2 \,\delta\left(E_{\nu,k'} - E_{\mu,k} \pm \hbar\omega\right), \tag{3.19}$$

where k and k' are the initial and final wave vectors along the nanowire axis at band indices μ and ν respectively. $V_{k,k'}$ is the matrix element for the particular scattering mechanism, $E_{\mu,k}$ and $E_{\nu,k'}$ are the initial and final energy states respectively and ω is the phonon wavenumber if present in the scattering mechanism. The wave function within the tight binding scheme for nanowires is given by equation (2.8).

3.2.1. Deformation Potential Scattering Rate

Similar to equation (3.2), the deformation potential scattering rate from k_x to $k_x^{'}$ is given by

$$W_{\mu,\nu}\left(k_x,k_x^{'},\mathbf{q}\right)=\frac{2\pi}{\hbar}\left|\left\langle\psi_\nu\left(k_x^{'}\right),N_{|\mathbf{q}|}+\frac{1}{2}\pm\frac{1}{2}\middle|H_{\mathbf{q},e-ph}\middle|\psi_\mu\left(k_x\right),N_{|\mathbf{q}|}\right\rangle\right|^2 \times\delta\left(E_\nu\left(k_x^{'}\right)-E_\mu\left(k_x\right)\pm\hbar\omega\left(|\mathbf{q}|\right)\right) \quad (3.20)$$

where the nanowire axis is assumed to be along the x-axis and that the phonons are described by bulk phonon dispersion relations. The matrix element in equation (3.20) is

$$V_{k_xk_x^{'}}=E_a\left[\frac{\hbar}{2\rho V\omega\left(|\mathbf{q}|\right)}\right]^{1/2}\left(N_{|\mathbf{q}|}+\frac{1}{2}\pm\frac{1}{2}\right)^{1/2}\int_{\mathbf{r}}\psi_\nu^*\left(k_x\right)e^{i\mathbf{q}.\mathbf{r}}\psi_\mu\left(k_x^{'}\right)d\mathbf{r} \quad (3.21)$$

Following the same steps used in the bulk rate calculation the integral in equation (3.21) is given by

$$\int_{\mathbf{r}}\psi_\nu^*\left(k_x\right)e^{i\mathbf{q}.\mathbf{r}}\psi_\mu\left(k_x^{'}\right)d\mathbf{r}=\sum_{m,m'}C_{\mu,m}\left(k_x\right)C_{\nu,m'}^*\left(k_x^{'}\right)\sum_{n,n'}\frac{1}{N}e^{-ik_x^{'}n'a_x}e^{ik_xna_x}I_{m,m',n,n'}\left(\mathbf{q}\right) \quad (3.22)$$

where

$$I_{m,m',n,n'}\left(\mathbf{q}\right)=\int_{\mathbf{r}}\phi_{m'}^*\left[\mathbf{r}-\left(\tau_{m'}\pm n'a_x\right)\right]e^{i\mathbf{q}.\mathbf{r}}\phi_m\left[\mathbf{r}-\left(\tau_m\pm na_x\right)\right]d\mathbf{r} \quad (3.23)$$

Using the same approximation used in the bulk case, equation (3.24) can be written as

$$\int_{\mathbf{r}}\psi_\nu^*\left(k_x\right)e^{i\mathbf{q}.\mathbf{r}}\psi_\mu\left(k_x^{'}\right)d\mathbf{r}=\sum_{m}C_{\mu,m}\left(k_x\right)C_{\nu,m}^*\left(k_x^{'}\right)e^{i\mathbf{q}.\tau_m}\delta\left[k_x-k_x^{'}+q_x\right] \quad (3.24)$$

The Kronecker delta function in equation (3.24) conserves momentum only along the direction of the nanowire axis. The matrix element for deformation potential scattering is therefore

$$V_{k_x k_x^{'}} = E_a \left[\frac{\hbar}{2\rho V \omega(|\mathbf{q}|)} \right]^{1/2} \left(N_{|\mathbf{q}|} + \frac{1}{2} \pm \frac{1}{2} \right)^{1/2} \times \sum_m C_{\mu,m}(k_x) C_{\nu,m}^{*}(k_x^{'}) e^{i\mathbf{q}.\tau_m} \delta\left[k_x - k_x^{'} + q_x \right] \tag{3.25}$$

The scattering rate from k_x to $k_x^{'}$ is then given by,

$$W_{\mu,\nu}(k_x, k_x^{'}) = \sum_{\mathbf{q}} W_{\mu,\nu}(k_x, k_x^{'}, \mathbf{q}) = \sum_{\mathbf{q}} \frac{2\pi}{\hbar} \left| V_{k_x k_x^{'}} \right|^2 \times \delta\left(E_\nu(k_x^{'}) - E_\mu(k_x) \pm \hbar\omega(|\mathbf{q}|) \right) \tag{3.26}$$

At this point the derivation of the scattering rates for nanowires starts to deviate from that of the bulk case due to the Kronecker delta function in equation (3.25). The momentum is only conserved along the direction of the nanowire axis. Therefore the summation over $\mathbf{q}$ in equation (3.26) along the confined directions needs to be calculated. The scattering rate from k_x to $\Delta k_x^{'}$ is given by

$$W_{\mu,\nu}(k_x, \Delta k_x^{'}) = \sum_{\Delta k_x^{'}, \mathbf{q}} W_{\mu,\nu}(k_x, k_x^{'}, \mathbf{q}) \tag{3.27}$$

Converting the summation over $\mathbf{q}$ to an integration over $\mathbf{q}$ and assuming dispersionless optical phonons and a linear dispersion and the equipartition approximation for acoustic phonons we get

$$W_{\mu,\nu,ac}(k_x, \Delta k_x^{'}) = \int_{\Delta k_x^{'}, q_x} \left[\frac{L_x}{2\pi} \frac{E_{ac} kT}{8\pi^2 \rho v_s^2 \hbar} \right] I_{\mu,\nu}(k_x, k_x^{'}) \times \delta\left[k_x - k_x^{'} + q_x \right] \delta\left(E_\nu(k_x^{'}) - E_\mu(k_x) \pm \hbar\omega(|\mathbf{q}|) \right) dq_x dk_x^{'} \tag{3.28}$$

for acoustic phonons and

$$W_{\mu,\nu,\mathrm{op}}\left(k_x,\Delta k_x^{'}\right)=\int\limits_{\Delta k_x^{'},q_x}\left[\frac{L_x}{2\pi}\frac{E_{op}}{8\pi^2\rho\omega_{op}}\right]\left(N_{|\mathbf{q},op|}+\frac{1}{2}\pm\frac{1}{2}\right)I_{\mu,\nu}\left(k_x,k_x^{'}\right) \times\delta\left[k_x-k_x^{'}+q_x\right]\delta\left(E_\nu\left(k_x^{'}\right)-E_\mu\left(k_x\right)\pm\hbar\omega\left(|\mathbf{q}|\right)\right)dq_x dk_x^{'} \tag{3.29}$$

for optical phonons. Converting the integral over q_x to a summation to get rid of the Kronecker delta function and integrating over the energy conserving delta function to obtain the density of states we get

$$W_{\mu,\nu,ac}\left(k_x,\Delta k_x^{'}\right)=\left[\frac{E_{ac}kT}{8\pi^2\rho v_s^2\hbar}\right]I_{\mu,\nu}\left(k_x,k_x^{'}\right)DOS\left(k_x^{'}\right) \tag{3.30}$$

and

$$W_{\mu,\nu,\mathrm{op}}\left(k_x,\Delta k_x^{'}\right)=\left[\frac{E_{op}}{8\pi^2\rho\omega_{op}}\right]\left(N_{|\mathbf{q},op|}+\frac{1}{2}\pm\frac{1}{2}\right)I_{\mu,\nu}\left(k_x,k_x^{'}\right)DOS\left(k_x^{'}\right) \tag{3.31}$$

where

$$I_{\mu,\nu}\left(k_x,k_x^{'}\right)=\int\limits_{q_t}\int\limits_{\theta}\sum_{m,m'}C_{\nu,m}^{*}\left(k_x^{'}\right)C_{\mu,m}\left(k_x\right)C_{\mu,m'}^{*}\left(k_x\right)C_{\nu,m'}\left(k_x^{'}\right)e^{i\mathbf{q}\cdot\left[\tau_m-\tau_{m'}\right]}q_t d\theta dq_t \tag{3.32}$$

and

$$DOS\left(k_x^{'}\right)=\frac{\partial k_x^{'}}{\partial E} \tag{3.33}$$

where q_t is the magnitude of the phonon wave vector $\mathbf{q}$ along the confinement plane, θ is the angle between q_y and q_z, and $q_x=k_x^{'}-k_x$. Equation (3.32) can be further simplified to

$$I_{\mu,\nu}\left(k_x,k_x^{'}\right)=2\pi\int\limits_{q_t=0}^{q_c}\sum_{m,m'}C_{\nu,m}^{*}\left(k_x^{'}\right)C_{\mu,m}\left(k_x\right)C_{\mu,m'}^{*}\left(k_x\right)C_{\nu,m'}\left(k_x^{'}\right) \times J_0\left(q_t a_{diff}\right)e^{iq_x\left[\tau_{m,x}-\tau_{m',x}\right]}q_t dq_t \tag{3.34}$$

where $a_{diff} = \sqrt{\left(\tau_{m,y} - \tau_{m',y}\right)^2 + \left(\tau_{m,z} - \tau_{m',z}\right)^2}$, J_0 is the Bessel function of the first kind and q_c is the cut-off wave vector for phonons along the confinement plane (Buin2008). Integrating equation (3.34) over q_t we get,

$$I_{\mu,\nu}\left(k_x, k_x^{'}\right) = 2\pi \sum_{m,m'} C_{\nu,m}^{*}\left(k_x^{'}\right) C_{\mu,m}\left(k_x\right) C_{\mu,m'}^{*}\left(k_x\right) C_{\nu,m'}\left(k_x^{'}\right) e^{iq_x\left[\tau_{m,x} - \tau_{m',x}\right]} F\left(a_{diff}\right) \quad (3.35)$$

where

$$F\left(a_{diff}\right) = \begin{cases} J_1\left(a_{diff} q_c\right) / a_{diff} & a_{diff} \neq 0 \\ q_c^2 / 2 & a_{diff} = 0 \end{cases} \quad (3.36)$$

If the atomic orbitals are also localized on the neighboring atoms as described previously then equation (3.35) becomes,

$$I_{\mu,\nu}\left(k_x, k_x^{'}\right) = 2\pi \sum_{m} P_{\mu,\nu,m}^{*}\left(k_x, k_x^{'}\right) \sum_{m'} P_{\mu,\nu,m'}\left(k_x, k_x^{'}\right) e^{iq_x\left[\tau_{m,x} - \tau_{m',x}\right]} F\left(a_{diff}\right) \quad (3.37)$$

where $P_{\mu,\nu,m}\left(k_x, k_x^{'}\right)$ is given by equation (3.18). The comparison between the scattering rates of bulk and nanowire materials for the same material using the same parameters is shown in Figures 3.3, 3.4, 3.5 and 3.6.

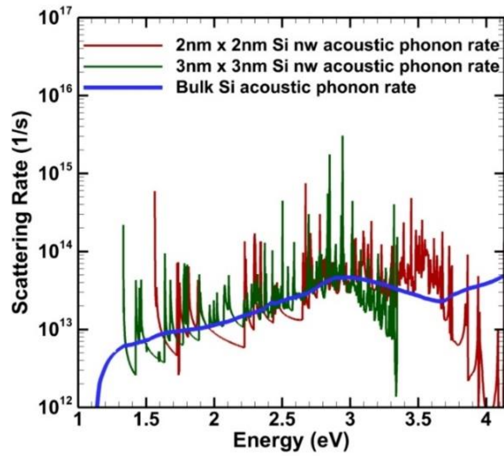

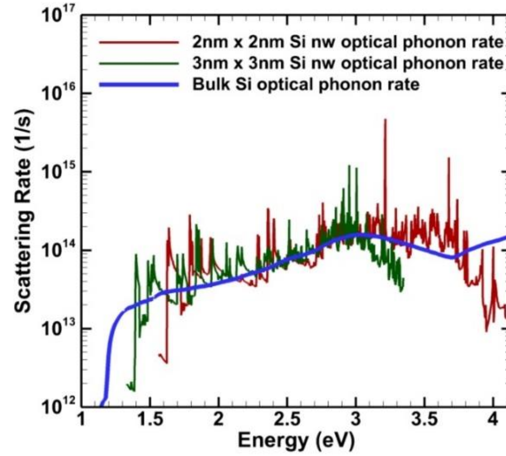

a) b)

Figure 3.3: Comparison between the electron scattering rate of bulk Si, 2 nm x 2 nm and 3 nm x 3 nm Si along [100] for a) acoustic phonons and b) non-polar optical phonons.

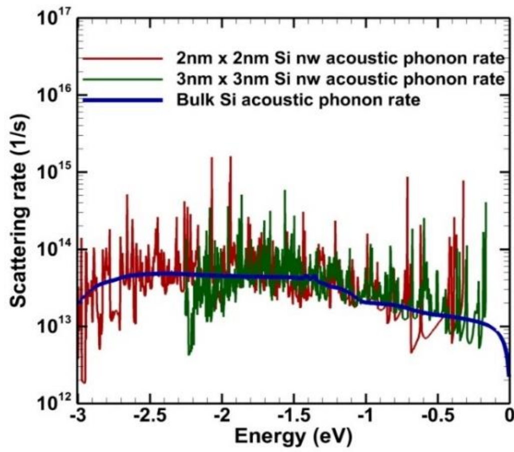

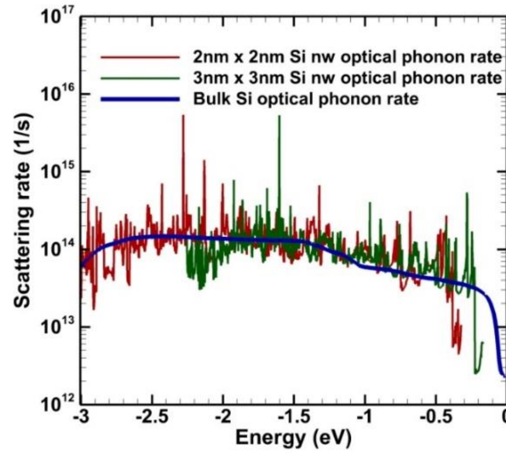

a) b)

Figure 3.4: Comparison between the hole scattering rate of bulk Si, 2 nm x 2 nm and 3 nm x 3 nm Si along [100] for a) acoustic phonons and b) non-polar optical phonons.

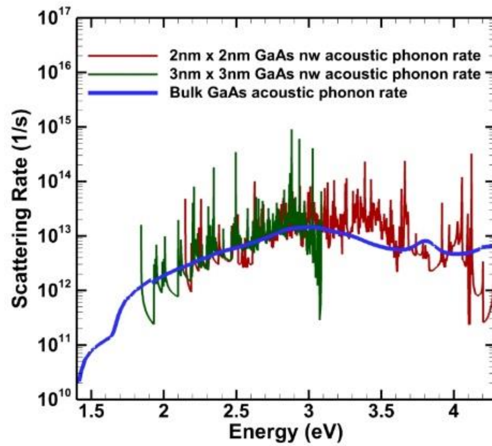

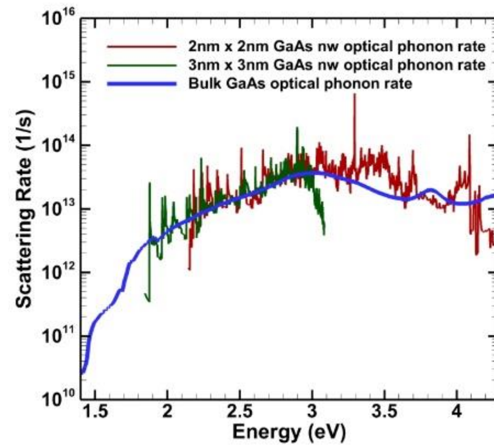

a) b)

Figure 3.5: Comparison between the electron scattering rate of bulk GaAs, 2 nm x 2 nm and 3 nm x 3 nm GaAs along [100] for a) acoustic phonons and b) non-polar optical phonons.

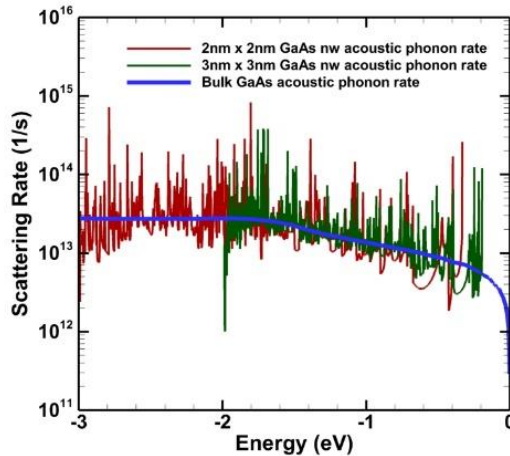

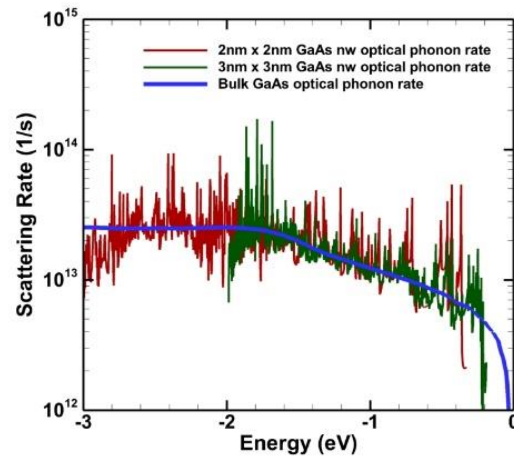

a) b)

Figure 3.6: Comparison between the hole scattering rate of bulk GaAs, 2 nm x 2 nm and 3 nm x 3 nm GaAs along [100] for a) acoustic phonons and b) non-polar optical phonons.

3.2.2. Polar Optical Phonon Scattering Rate

Similar derivation for polar optical phonon scattering gives the rate from k_x to $\Delta k_x^{'}$ as

$$W_{pop,\mu,\nu}\left(k_x,\Delta k_x^{'}\right)=\frac{\omega_0 e^2}{16\pi^2}\left[\frac{1}{\varepsilon_\infty}-\frac{1}{\varepsilon_0}\right]\left(N_{|\mathbf{q}|,\mathrm{op}}+\frac{1}{2}\pm\frac{1}{2}\right)I_{pop,\mu,\nu}\left(k_x,k_x^{'}\right)DOS(k_x^{'}) \quad (3.38)$$

where

$$\begin{aligned} I_{pop,\mu,\nu}\left(k_x,k_x^{'}\right)=&\sum_m P_{\mu,\nu,m}^{*}\left(k_x,k_x^{'}\right)\sum_{m'}P_{\mu,\nu,m'}\left(k_x,k_x^{'}\right)\\ &\times\left[e^{iq_x\left[\tau_{m,x}-\tau_{m',x}\right]}\int_0^{q_c}\frac{J_0\left(q_t a_{diff}\right)}{q_x^2+q_t^2}q_t dq_t\right] \end{aligned} \quad (3.39)$$

The latter integral in equation (3.39) is pre-calculated for different values of q_x and a_{diff} at the beginning of the simulation. This greatly improves the computational time. Figure 3.7 show the comparison between bulk scattering rates and nanowire scattering rates calculated using the above formulae.

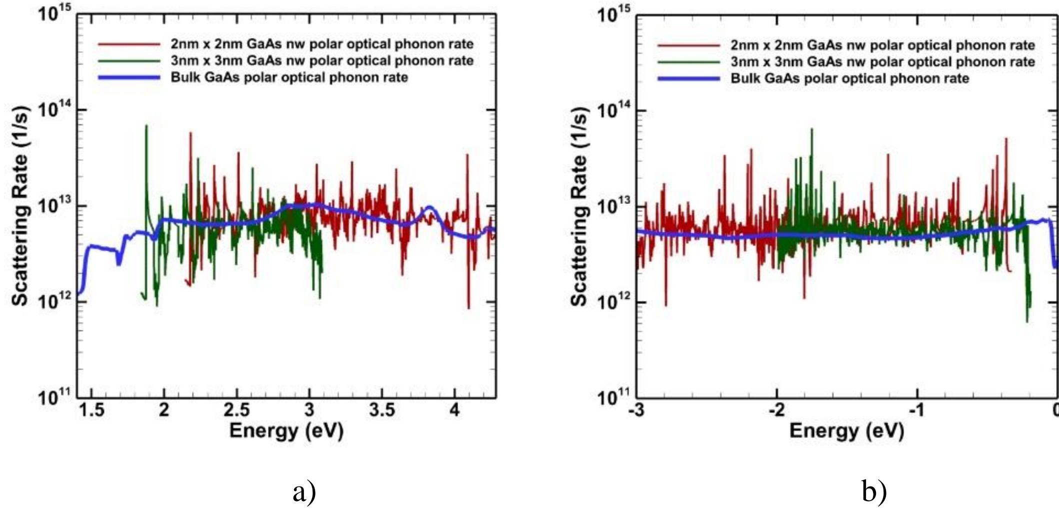

a) b)

Figure 3.7: Comparison between the polar optical scattering rate of bulk GaAs, 2 nm x 2 nm and 3 nm x 3 nm GaAs along [100] for a) electrons and b) holes.

3.2.3. Ionized Impurity Scattering Rate

The ionized impurity scattering rate is calculated for each ionized impurity atom and then multiplied over the number of ionized impurities present in a unit cell of the nanowire. The scattering rate due to a single ionized impurity i is given by Fermi's golden rule (Ferry2009)

$$W_{imp,\mu,\nu}\left(k_x,k_x^{'}\right)=\frac{2\pi}{\hbar}\left|V_i\left(k_x,k_x^{'}\right)\right|^2\delta\left(E_\nu\left(k_x^{'}\right)-E_\mu\left(k_x\right)\right) \tag{3.40}$$

where

$$V_i\left(k_x,k_x^{'}\right)=\frac{Ze^2}{\left(2\pi\right)^3}\int_{\mathbf{r},\mathbf{q}}\psi_\nu^*\left(k_x^{'}\right)\frac{e^{i\mathbf{q}\cdot[\mathbf{r}-\mathbf{r}_i]}}{\varepsilon_{1D}\left(q_x\right)\left|\mathbf{q}\right|^2}\psi_\mu\left(k_x\right)d^3rd^3q \tag{3.41}$$

where $\mathbf{r}_i$ is the position of the ith impurity atom within the unit/super cell. Expanding the tight binding wave functions and assuming only interactions between similar orbitals on the same atom is non-negligible we get

$$V_i\left(k_x,k_x^{'}\right)=\frac{Ze^2}{\left(2\pi\right)^3}\int_{q_x,q_t,\theta}\sum_m C_\nu^*\left(k_x^{'}\right)\frac{e^{i\mathbf{q}\cdot\left[\tau_m-\mathbf{r}_i\right]}e^{-\left(q_t^2+q_x^2\right)^2\alpha^2/8}}{\varepsilon_{1D}\left(q_x\right)\left|\mathbf{q}\right|^2}q_t C_\mu\left(k_x\right) \\ \times\delta\left[k_x^{'}-k_x+q_x\right]dq_x dq_t d\theta \tag{3.42}$$

where $\mathbf{q}=\left(q_t,q_x\right)$. Converting the integration over q_x to a summation to deal with the Kronecker delta function and using similar identities that were used for polar optical phonon scattering we get

$$V_i\left(k_x,k_x^{'}\right)=V_i\left(q_x,r_i\right)=\frac{2\pi}{L_x}\frac{Ze^2}{4\pi^2\varepsilon_{1D}\left(q_x\right)}\sum_m C_\nu^*\left(k_x^{'}\right)C_\mu\left(k_x\right)e^{iq_x\left[\tau_{m,x}-r_{i,x}\right]}F_{m,i}\left(q_x\right) \tag{3.43}$$

where

$$F_{m,i}\left(q_x\right)=\int_{q_t}\frac{J_0\left(q_t a_{diff}\right)}{q_x^2+q_t^2}q_t dq_t \tag{3.44}$$

where $a_{diff}=\sqrt{\left(\tau_{m,y}-\tau_{\mathrm{r}_i,y}\right)^2+\left(\tau_{m,\mathrm{z}}-\tau_{\mathrm{r}_i,\mathrm{z}}\right)^2}$ is the radial distance between orbital m and impurity $\mathbf{r}_i$, L_x is the length of the crystal along the nanowire axis and $q_x=k_x^{'}-k_x$. The scattering rate due to a density of impurity atoms is obtained by averaging over every atom in the unit cell. The total scattering rate due to a density of impurity atoms N_I is given by

$$W_{imp,\mu,\nu}(k_x,k_x^{'})=\left(\frac{2\pi}{L_x}\right)^2\frac{2\pi}{\hbar}\frac{N_I V}{N_{atoms}}\sum_{i=1}^{N_{atoms}}\frac{\left|V_{i,\mu,\nu}\left(q_x,\mathbf{r}_i\right)\right|^2}{\left|\varepsilon_{1D}\left(q_x\right)\right|^2}\delta\left(E_\nu\left(k_x^{'}\right)-E_\mu\left(k_x\right)\right) \tag{3.45}$$

where V is the volume of the crystal. The scattering rate from k_x to $\Delta k_x^{'}$ is obtained by summing equation (3.45) over all final states and converting that summation to an integration to deal with the Dirac delta function to get

$$W_{imp,\mu,\nu}(k_x,\Delta k_x^{'}) = \frac{4\pi^2}{\hbar}\frac{A_{cs}N_I}{N_{atoms}}\sum_{i=1}^{N_{atoms}}\frac{\left|V_{i,\mu,\nu}\left(q_x,\mathbf{r}_i\right)\right|^2}{\left|\varepsilon_{1D}\left(q_x\right)\right|^2}DOS\left(k_x^{'}\right) \tag{3.46}$$

where the ratio V/L_x is denoted by the nanowire cross-sectional area A_{cs}. Figure (3.6) show the plot of ionized impurity scattering for a 2 nm x 2 nm and 3 nm x 3 nm Si nanowire along the [100] direction.

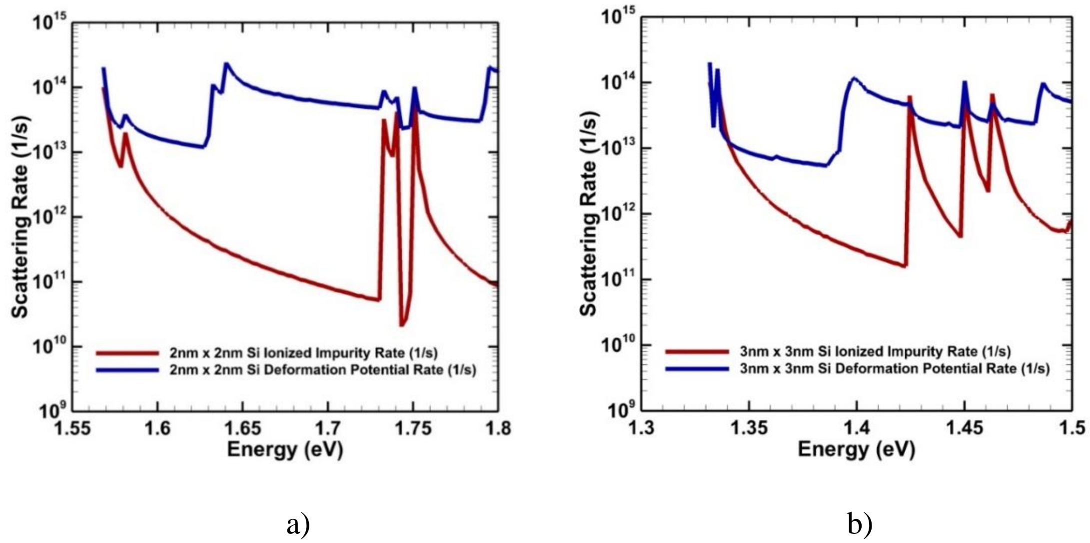

a) b)

Figure 3.8: Ionized impurity scattering rate and deformation potential scattering rate of a) 2 nm x 2 nm Si nanowire along [100] and b) 3 nm x 3 nm Si nanowire along [100].

3.2.4. Dielectric Screening in Nanowires

The induced charge due to a time dependent perturbation of an external potential is given by (Ferry2009)

$$\rho_{\text{ind}}(\mathbf{r},\omega) = -e\sum_{k_x,n,n'} \psi_n^*(k_x)\psi_{n'}(k_x+q_x)V_{nn'}^{ext}(q_x)L_{nn'}(q_x,\omega)e^{iq_x x} \tag{3.47}$$

where $\mathbf{r} = (\mathbf{r}_t, x)$, where $\mathbf{r}_i$ is a vector along the confinement plane and x is along the nanowire axis, n and n' are initial and final band indices, $V_{nn'}^{ext}(q_x)$ is the Fourier transform of the external potential and $L_{nn'}(q_x,\omega)$ is the Lindhard dielectric function given by

$$L_{nn'}(q_x,\omega) = \frac{f_n(k_x) - f_{n'}(k_x+q_x)}{E_{n'}(k_x+q_x) - E_n(k_x) - \hbar\omega - i\alpha\hbar} \tag{3.48}$$

where α is a small convergence parameter. The induced potential due this charge is given by Coulomb's law as

$$V_{ind}(\mathbf{r}) = -\frac{e}{4\pi\varepsilon_s}\int_{\mathbf{r}'} \frac{\rho_{\text{ind}}(\mathbf{r}',\omega)}{|\mathbf{r}-\mathbf{r}'|}d\mathbf{r}' \tag{3.49}$$

Using the Fourier transform of the potential gives us

$$V_{ind}(\mathbf{r}) = -\frac{e}{(2\pi)^3\varepsilon_s}\int_{\mathbf{r}',\mathbf{q}'} \frac{\rho_{\text{ind}}(\mathbf{r}',\omega)}{|\mathbf{q}'|^2}e^{i\mathbf{q}'\cdot(\mathbf{r}-\mathbf{r}')}d\mathbf{r}'d\mathbf{q}' \tag{3.50}$$

Using equation (3.47) the potential may be written as

$$\begin{aligned} V_{ind}(\mathbf{r}) = \frac{e^2}{(2\pi)^3\varepsilon_s}\int_{\mathbf{r}',\mathbf{q}'}\sum_{k_x,n,n'} \psi_n^*(k_x,\mathbf{r}')\psi_{n'}(k_x+q_x,\mathbf{r}')V_{nn'}^{ext}(q_x) \\ \times L_{nn'}(q_x,\omega)e^{iq_x x'}\frac{e^{i\mathbf{q}'\cdot(\mathbf{r}-\mathbf{r}')}}{|\mathbf{q}'|^2}d\mathbf{r}'d\mathbf{q}' \end{aligned} \tag{3.51}$$

The spatial dependence of the wave functions are shown to stress that the integration is done over $\mathbf{r}'$. Expanding the tight binding wave functions and using the same approximations that were used for the derivations of the scattering rates the induced potential can be written as

$$V_{ind}(\mathbf{r}) = \frac{e^2}{(2\pi)^3 \varepsilon_s} \int_{\mathbf{q}'} \sum_{k_x,n,n',\mu} C^*_{n,\mu}(k_x) C_{n',\mu}(k_x+q_x) e^{iq_x\tau_{\mu,x}} e^{i\mathbf{q}_x'\cdot\mathbf{r}} \frac{e^{-i\mathbf{q}'\cdot\tau_\mu}}{|\mathbf{q}'|^2} \times \delta\left[q_x - q_x'\right] L_{nn'}(q_x,\omega) V^{ext}_{nn'}(q_x)\, dq_x' dq_t' d\theta' \tag{3.52}$$

Converting the integration over q_x' to a summation to get rid of the Kronecker delta function and force $q_x' = q_x$ we get the final expression of the induced potential as,

$$V_{ind}(\mathbf{r}) = \frac{2\pi}{L_x} \frac{e^2}{(2\pi)^3 \varepsilon_s} \int_{q_t',\theta'} \sum_{k_x,n,n',\mu} C^*_{n,\mu}(k_x) C_{n',\mu}(k_x+q_x) e^{iq\tau_{\mu,x}} e^{i\mathbf{q}'\cdot\mathbf{r}} \times \frac{e^{-i\mathbf{q}'\cdot\tau_\mu}}{|\mathbf{q}'|^2} L_{nn'}(q_x,\omega) V^{ext}_{nn'}(q_x)\, dq_t' d\theta' \tag{3.53}$$

where $\mathbf{q}' = (q_t', q_x')$. We now look at the matrix element of the induced potential over initial and final basis states k_x and k_x' in bands m and m', respectively.

$$V^{mm'}_{ind}(k_x - k_x') = \sum_{k_x'} \int_{\mathbf{r}} \psi^*_{m'}(k_x',\mathbf{r}) V_{ind}(\mathbf{r}) \psi_m(k_x,\mathbf{r})\, d\mathbf{r} \tag{3.54}$$

Inserting equation (3.54) into equation (3.53), the induced potential can be written as

$$V^{mm'}_{ind}(k_x - k_x') = \frac{2\pi}{L_x} \frac{e^2}{(2\pi)^3 \varepsilon_s} \sum_{k_x' k_x,n,n',\mu} \int_{\mathbf{r}} \int_{q_t',\theta'} C^*_{n,\mu}(k_x) C_{n',\mu}(k_x+q_x) \times \psi^*_{m'}(k_x',\mathbf{r}) \psi_m(k_x,\mathbf{r}) e^{iq_x\tau_{\mu,x}} \times e^{i\mathbf{q}'\cdot\mathbf{r}} \frac{e^{-i\mathbf{q}'\cdot\tau_\mu}}{|\mathbf{q}'|^2} L_{nn'}(q_x,\omega) V^{ext}_{nn'}(q_x)\, dq_t' d\theta' d\mathbf{r} \tag{3.55}$$

Once again, expanding the tight binding wave functions and using the localized orbital approximations we get

$$V_{ind}^{mm'}\left(k_x-k_x^{'}\right)=\frac{e^2}{L_x\left(2\pi\right)^2\varepsilon_s}\sum_{\substack{k_x^{'}k_x,\\ n,n',\\ \mu,\mu'}}\int_{q_t^{'},\theta'}C_{n,\mu}^{*}\left(k_x\right)C_{n',\mu}\left(k_x+q_x\right)C_{m',\mu'}^{*}\left(k_x^{'}\right)C_{m,\mu'}\left(k_x\right)$$
$$\times e^{iq_x\tau_{\mu,x}}\frac{e^{i\mathbf{q}'\cdot\left[\tau_{\mu'}-\tau_{\mu}\right]}}{\left|\mathbf{q}'\right|^2}\delta\left[k_x^{'}-k_x+q_x\right]L_{nn'}\left(q_x,\omega\right)V_{nn'}^{ext}\left(q_x\right)dq_t^{'}d\theta' \tag{3.56}$$

The summation over final states collapses the Kronecker delta function to give $k_x^{'}=k_x+q_x$. The net induced potential can now be written as

$$V_{ind}^{mm'}\left(q_x\right)=\frac{e^2}{L_x\left(2\pi\right)^2\varepsilon_s}\sum_{\substack{k_x,n,\\ n',\mu,\\ \mu'}}\int_{q_t^{'},\theta'}C_{n,\mu}^{*}\left(k_x\right)C_{n',\mu}\left(k_x+q_x\right)C_{m',\mu'}^{*}\left(k_x+q_x\right)C_{m,\mu'}\left(k_x\right)$$
$$\times e^{iq_x\tau_{\mu,x}}\frac{e^{i\mathbf{q}'\cdot\left[\tau_{\mu'}-\tau_{\mu}\right]}}{\left|\mathbf{q}'\right|^2}L_{nn'}\left(q_x,\omega\right)V_{nn'}^{ext}\left(q_x\right)dq_t^{'}d\theta' \tag{3.57}$$

The integral is similar to the one used in polar optical phonon scattering, using the same integral identities, the induced potential is given by

$$V_{ind}^{mm'}\left(q_x\right)=\frac{2\pi}{L_x}\frac{e^2}{\left(2\pi\right)^2\varepsilon_s}\sum_{k_x,n,n'}F_{\mathrm{n,n'}}\left(k_x,q_x\right)L_{nn'}\left(q_x,\omega\right)V_{nn'}^{ext}\left(q_x\right) \tag{3.58}$$

where

$$F_{\mathrm{n,n'}}\left(k_x,q_x\right)=\sum_{\mu,\mu'}C_{n,\mu}^{*}\left(k_x\right)C_{n',\mu}\left(k_x+q_x\right)C_{m',\mu'}^{*}\left(k_x+q_x\right)C_{m,\mu'}\left(k_x\right)$$
$$\times e^{iq_x\tau_{\mu,x}}\int_{q_t}\frac{J_0\left(q_t a_{diff}\right)}{q_x^2+q_t^2}q_t dq_t \tag{3.59}$$

where $a_{diff}=\sqrt{\left(\tau_{\mu,y}-\tau_{\mu',y}\right)^2+\left(\tau_{\mu,\mathrm{z}}-\tau_{\mu',\mathrm{z}}\right)^2}$. The dielectric function can be defined as

$$V_{tot}^{mm'}\left(q_x\right)=\sum_{n,n'}\varepsilon_{nn'mm'}^{-1}\left(q_x,\omega\right)V_{nn'}^{ext}\left(q_x\right) \tag{3.60}$$

where $\varepsilon_{nn'mm'}(q_x,\omega)$ defines the four-dimensional dielectric matrix and $V_{tot}^{mm'}(q_x)=V_{ind}^{mm'}(q_x)+V_{ext}^{mm'}(q_x)$. Using equation (3.58), and converting the summation of final states to an integration this gives

$$\varepsilon_{nn'mm'}(q_x,\omega)=\left[\delta_{n,m}\delta_{n',m'}-\frac{e^2}{(2\pi)^2\varepsilon_s}\int_{k_x}F_{\mathrm{n,n'}}(k_x,q_x)L_{nn'}(q_x,\omega)\right] \tag{3.61}$$

Summing over n and n' gives the final 1D dielectric matrix as

$$\varepsilon_{1D,mm'}(q_x,\omega)=\sum_{nn'}\varepsilon_{nn'mm'}(q_x,\omega) \tag{3.62}$$

3.2.5. Surface Roughness Scattering in Nanowires

Using Fermi's Golden Rule, the scattering rate for surface roughness can be written as (Kotylar2012)

$$W_{\mu,\nu}(k_x,k_x^{'})=\frac{\left|F^{i}_{\mu,k_x,\nu,k_x^{'}}\right|^2}{\hbar}\left\langle\Delta^2_{q_\pm}\right\rangle DOS(k_x^{'}) \tag{3.63}$$

where

$$\left\langle\Delta^2_{q_{x\pm}}\right\rangle=\frac{3\pi}{4}\Delta^2\lambda\frac{1}{\left(1+\frac{q_\pm^2\lambda^2}{2}\right)^{\frac{5}{2}}} \tag{3.64}$$

and

$$F^{i}_{\mu,k_x,\nu,k_x^{'}} = \frac{\partial E_{\mu,k_x}}{\partial r_c}|_{V=0}\ \delta_{\mu,\nu} + \sum_m C^*_{\mu,m}(k_x) C_{\nu,m}(k_x^{'}) \frac{\partial V_m}{\partial r_c}\left(1 - \frac{\left|r_c^i - r_{mc}\right|}{t_i}\right)$$
$$+ \left(E_{\mu,k_x} - E_{\nu,k_x^{'}}\right) \sum_m C^*_{\mu,m}(k_x) \frac{\partial C_{\nu,m}(k_x^{'})}{\partial r_c}\left(1 - \frac{\left|r_c^i - r_{mc}\right|}{t_i}\right) \tag{3.65}$$

where λ is the correlation length, Δ is the rms fluctuation of the surface i, r_c^i is the distance along the direction c from the surface and t_i is the maximum distance of an atom from the surface along the direction c. The overlap integral in equation (3.65) consists of three parts. The first part is the Prange-Nee term. To calculate this we add an atomic layer to the surface i as shown in Figure 3.9 and the derivative is approximated as

$$\frac{\partial E_{\mu,k}}{\partial r_c}|_{V=0} \approx \frac{\left(E_{\mu,k} - E_{\mu,k,0}\right)}{r_c} \tag{3.66}$$

where $E_{\mu,k,0}$ is the eigenvalue of the band μ at k before the atomic layer is added and $E_{\mu,k}$ is the eigenvalue after the atomic layer is added. r_c is the thickness of the atomic layer. The last two terms represent the electrostatics. The 2nd term is simple to evaluate and requires the Poisson solution at each atomic position. Since the Poisson grid is a regular grid, interpolating the potential to the atomic positions is trivial. On the other hand, the 3rd term requires the derivatives of the expansion coefficients along the direction normal to the surface. Approximating the derivative using finite difference, we need to interpolate the expansion coefficients along the direction normal to the surface. This is not trivial as the atom positions represent scattered data as shown in Figure 3.10.

Therefore the local polynomial interpolation method is used to do this, which is implemented from an external library.

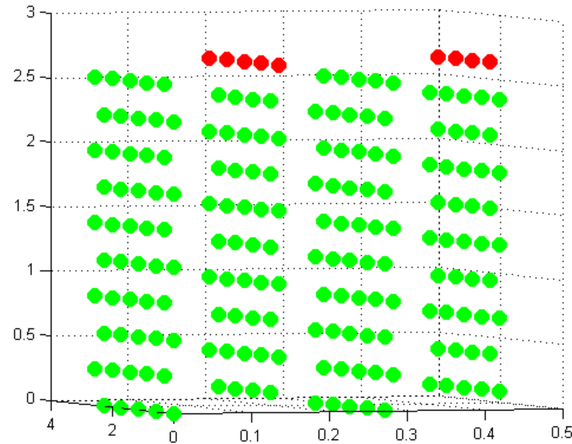

Figure 3.9: Plot of the additional atom layer added to a 2.5 nm x 2.5 nm Si nanowire to calculate the Prange-Nee term in equation (3.65).

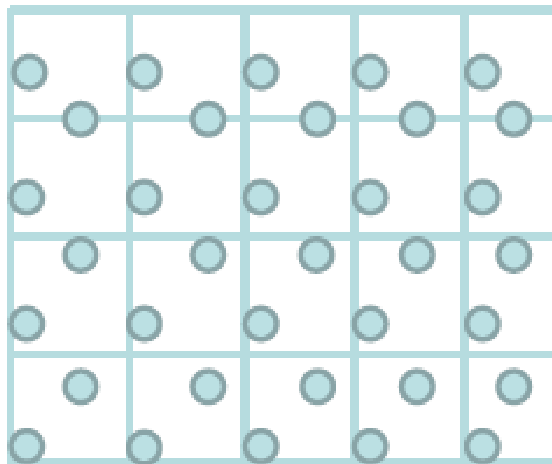

Figure 3.10: Plot of the atom structure against a Poisson grid in two dimensions to show the requirement of a local interpolation method to calculate the derivative of the atom tight binding coefficients along the Poisson grid points.

3.2.6. Impact Ionization Scattering

The impact ionization rate is calculated using the Fermi's golden rule assuming the dielectric constant is a scalar value and the frequency dependence of this quantity will be ignored. The rate of impact ionization from $k_{1,n}$ to $k_{2,n'}$ is (Ferry1991)

$$\begin{aligned} W_{II}\left(k_{1,\mathrm{n}},k_{2,\mathrm{n'}}\right) = \frac{2\pi}{\hbar}\sum_{\substack{k_4,k_3,\\ m,m'}}\left|M\left(k_{1,\mathrm{n}},k_{2,\mathrm{n'}},k_{3,\mathrm{m'}},k_{4,\mathrm{m}}\right)\right|^2 \\ \times\delta\Big(E\left(k_1\right)-E\left(k_4\right)-E\left(k_2\right)-E\left(k_3\right)\Big) \end{aligned} \tag{3.67}$$

where $k_{1,n}$ is the initial electron in band n, $k_{2,n'}$ is the final state of the initial electron after the scattering process, $k_{4,\mathrm{m}}$ is the bound electron (hole) in the valence band before the scattering process and $k_{4,\mathrm{m'}}$ is the final state of the bound electron in the conduction band. Therefore in equation (3.67) the summation is over the valence bands for the bound electron and the conduction band for the final state of the bound electron. The matrix element in equation (3.67) is given by (Kamakura1994)

$$\left|M\left(k_{1,\mathrm{n}},k_{2,\mathrm{n'}},k_{3,\mathrm{m'}},k_{4,\mathrm{m}}\right)\right|^2 = \frac{1}{2}\left(\left|M_a\right|^2+\left|M_b\right|^2+\left|M_a-M_b\right|^2\right) \tag{3.68}$$

where

$$M_a = \int\left\langle \psi_{1,\mathrm{n}}\left(k_1,\mathbf{r}_1\right)\psi_{4,\mathrm{m}}\left(k_4,\mathbf{r}_2\right)\left|\frac{e^2}{4\pi\varepsilon\left|\mathbf{r}_1-\mathbf{r}_2\right|}\right|\psi_{2,\mathrm{n'}}\left(k_2,\mathbf{r}_1\right)\psi_{3,\mathrm{m'}}\left(k_3,\mathbf{r}_2\right)\right\rangle d\mathbf{r}_1 d\mathbf{r}_2 \tag{3.69}$$

$$M_b = \int\left\langle \psi_{1,\mathrm{n}}\left(k_1,\mathbf{r}_1\right)\psi_{4,\mathrm{m}}\left(k_4,\mathbf{r}_2\right)\left|\frac{e^2}{4\pi\varepsilon\left|\mathbf{r}_1-\mathbf{r}_2\right|}\right|\psi_{3,\mathrm{m'}}\left(k_2,\mathbf{r}_1\right)\psi_{2,\mathrm{n'}}\left(k_3,\mathbf{r}_2\right)\right\rangle d\mathbf{r}_1 d\mathbf{r}_2 \tag{3.70}$$

and the ½ factor in equation (3.68) is due to the fact that the same processes are counted twice in the summation. Assuming $M_a = M_b$ we can write (3.67) as

$$W_{II}\left(k_{1,\mathrm{n}}, k_{2,\mathrm{n}'}\right) = \frac{2\pi}{\hbar} \sum_{\substack{k_4, k_3, \\ m, m'}} \left| M\left(k_{1,\mathrm{n}}, k_{4,\mathrm{m}}; k_{2,\mathrm{n}'}, k_{3,\mathrm{m}'}\right) \right|^2 \times \delta\Big(E(k_1) - E(k_4) - E(k_2) - E(k_3)\Big) \tag{3.71}$$

where

$$M\left(k_{1,\mathrm{n}}, k_{4,\mathrm{m}}; k_{2,\mathrm{n}'}, k_{3,\mathrm{m}'}\right) = \int \left\langle \psi_{1,\mathrm{n}}\left(k_1, \mathbf{r}_1\right) \psi_{4,\mathrm{m}}\left(k_4, \mathbf{r}_2\right) \left| \frac{e^2}{4\pi\varepsilon \left|\mathbf{r}_1 - \mathbf{r}_2\right|} \right| \psi_{2,\mathrm{n}'}\left(k_2, \mathbf{r}_1\right) \psi_{3,\mathrm{m}'}\left(k_3, \mathbf{r}_2\right) \right\rangle d\mathbf{r}_1 d\mathbf{r}_2 \tag{3.72}$$

Simplifying equation (3.72) we use the Fourier transform of $\frac{e^2}{4\pi\varepsilon\left|\mathbf{r}_1 - \mathbf{r}_2\right|}$ as

$$\int \frac{e^2}{(2\pi)^3} \frac{e^{i\mathbf{q}.\left|\mathbf{r}_1 - \mathbf{r}_2\right|}}{\varepsilon\left|\mathbf{q}\right|^2} d\mathbf{q} = \sum_{\mathbf{q}} \frac{e^2}{V} \frac{e^{i\mathbf{q}.\left|\mathbf{r}_1 - \mathbf{r}_2\right|}}{\varepsilon\left|\mathbf{q}\right|^2} = \frac{e^2}{4\pi\varepsilon\left|\mathbf{r}_1 - \mathbf{r}_2\right|} \tag{3.73}$$

and considering only the terms involving $\mathbf{r_1}$ in equation (3.72) we get

$$I_1 = \int \sum_{\mathbf{q}} \psi_{1,\mathrm{n}}\left(k_1, \mathbf{r}_1\right) \frac{e^2}{V} \frac{e^{i\mathbf{q}.\left|\mathbf{r}_1 - \mathbf{r}_2\right|}}{\varepsilon\left|\mathbf{q}\right|^2} \psi_{2,\mathrm{n}'}\left(k_2, \mathbf{r}_1\right) d\mathbf{r}_1 \tag{3.74}$$

Expanding the TB wave functions as was done previously and using the small $\mathbf{q}$ approximation.

$$I_1 = \sum_{\substack{q_x, \mathbf{q}_t, \\ \mu}} C_{\mathrm{n},\mu}\left(k_1\right) C^*_{n',\mu}\left(k_2\right) \frac{e^2}{V} \frac{e^{i\mathbf{q}.\left|\tau_\mu - \mathbf{r}_2\right|}}{\varepsilon\left|\mathbf{q}\right|^2} \delta\left[k_1 - k_2 + q_x\right] \tag{3.75}$$

where $\mathbf{q}=\left(q_x,\mathbf{q}_t\right)$. Including the terms involving **r2** as well, the matrix element in equation (3.75) becomes

$$M=I_2=\int\psi_{4,\mathrm{m}}\left(k_4,\mathbf{r}_2\right)I_1\psi_{3,\mathrm{m'}}\left(k_3,\mathbf{r}_2\right)d\mathbf{r}_2 \tag{3.76}$$

$$\begin{aligned}I_2=&\sum_{\substack{q_x,\mathbf{q}_t,\\ \mu,\nu}}C_{\mathrm{n},\mu}\left(k_1\right)C^*_{n',\mu}\left(k_2\right)\frac{e^2}{V}\frac{e^{i\mathbf{q}.\left|\tau_\mu-\tau_\nu\right|}}{\varepsilon\left|\mathbf{q}\right|^2}C_{\mathrm{m},\nu}\left(k_4\right)C^*_{\mathrm{m'},\nu}\left(k_3\right)\\ &\times\delta\left[k_1-k_2+q_x\right]\delta\left[k_4-k_3+q_x\right]\end{aligned} \tag{3.77}$$

Summing over q_x we get

$$I_2=\sum_{\substack{\mathbf{q}_t,\\ \mu,\nu}}C_{\mathrm{n},\mu}\left(k_1\right)C^*_{n',\mu}\left(k_2\right)\frac{e^2}{V}\frac{e^{i\mathbf{q}.\left|\tau_\mu-\tau_\nu\right|}}{\varepsilon\left|\mathbf{q}\right|^2}C_{\mathrm{m},\nu}\left(k_4\right)C^*_{\mathrm{m'},\nu}\left(k_3\right)\delta\left[k_4-k_3-\left(k_1-k_2\right)\right] \tag{3.78}$$

Converting the summation over q_t into an integration we get

$$M=\frac{e^2}{L_x\varepsilon\left(2\pi\right)}F_{\substack{n,n'\\ m,m'}}\left(k_1,k_2,k_3,k_4\right)\delta\left[k_4-k_3-\left(k_1-k_2\right)\right] \tag{3.79}$$

where

$$\begin{aligned}F_{\substack{n,n'\\ m,m'}}\left(k_1,k_2,k_3,k_4\right)=&\sum_{\mu,\nu}C_{\mathrm{n},\mu}\left(k_1\right)C^*_{n',\mu}\left(k_2\right)C_{\mathrm{m},\nu}\left(k_4\right)C^*_{\mathrm{m'},\nu}\left(k_3\right)e^{iq_x\cdot\left|\tau_\mu-\tau_\nu\right|}\\ &\times\int_{q_t}\frac{J_0\left(q_t a_{diff}\right)}{q_x^2+q_t^2}q_t dq_t\end{aligned} \tag{3.80}$$

where $a_{diff}=\sqrt{\left(\tau_{\mu,y}-\tau_{\nu,y}\right)^2+\left(\tau_{\mu,\mathrm{z}}-\tau_{\nu,\mathrm{z}}\right)^2}$

The scattering rate from $k_{1,n}$ to $k_{2,n'}$ is therefore

$$W_{II}\left(k_{1,\mathrm{n}},k_{2,\mathrm{n'}}\right)=\frac{2\pi}{\hbar}\sum_{\substack{k_4,k_3,\\ m,m'}}M^2\delta\left(E\left(k_1\right)-E\left(k_4\right)-E\left(k_2\right)-E\left(k_3\right)\right) \tag{3.81}$$

Inserting equation (3.79) into equation (3.81) we get

$$\begin{aligned}W_{II}\left(k_{1,\mathrm{n}},k_{2,\mathrm{n'}}\right)=\frac{2\pi}{\hbar}\frac{e^4}{\varepsilon^2L_x^2\left(2\pi\right)^2}\sum_{\substack{k_4,k_3,\\ m,m'}}&\left|F_{\substack{n,n'\\ m,m'}}\left(k_1,k_2,k_3,k_4\right)\right|^2\\ &\times\delta\left[k_4-k_3-\left(k_1-k_2\right)\right]\\ &\times\delta\left(E\left(k_1\right)-E\left(k_4\right)-E\left(k_2\right)-E\left(k_3\right)\right)\end{aligned} \tag{3.82}$$

Summing over k_4 can be done trivially giving

$$\begin{aligned}W_{II}\left(k_{1,\mathrm{n}},k_{2,\mathrm{n'}}\right)=\frac{2\pi}{\hbar}\frac{e^4}{\varepsilon^2L_x^2\left(2\pi\right)^2}\sum_{\substack{k_3,\\ m,m'}}&\left|F_{\substack{n,n'\\ m,m'}}\left(k_1,k_2,k_3,k_4\right)\right|^2\\ &\times\delta\left(E_n\left(k_1\right)-E_m\left(k_4\right)-E_{n'}\left(k_2\right)-E_{m'}\left(k_3\right)\right)\end{aligned} \tag{3.83}$$

where $k_4=k_3-\left(k_1-k_2\right)$. To perform the sum over k_3 the summation has to be converted to an integral and the delta function in energy has to be used. This gives

$$\begin{aligned}W_{II}\left(k_{1,\mathrm{n}},k_{2,\mathrm{n'}}\right)=\frac{1}{\hbar}\frac{e^4}{\varepsilon^2L_x\left(2\pi\right)^2}\sum_{i,m,m'}&\left|F_{\substack{n,n'\\ m,m'}}\left(k_1,k_2,k_i,k_i-\left(k_1-k_2\right)\right)\right|^2\\ &\times\left[JDOS_{m,m'}\left(k_i-\left(k_1-k_2\right),k_i\right)\right]\end{aligned} \tag{3.84}$$

where

$$JDOS_{m,m'}\left(k_a,k_b\right)=\frac{DOS_m\left(k_a\right)DOS_{m'}\left(k_b\right)}{DOS_m\left(k_a\right)+DOS_{m'}\left(k_b\right)} \tag{3.85}$$

where k_i are the values of k_3 that satisfy the energy conservation relation given by

$$E_n(k_1) - E_m(k_3 - (k_1 - k_2)) - E_{n'}(k_2) - E_{m'}(k_3) = 0 \tag{3.86}$$

Finally, calculating the scattering rate to a region of k-space around k_2 we get

$$\begin{aligned} W_{II}(k_{1,\mathrm{n}}, \Delta k_{2,\mathrm{n'}}) = \frac{1}{\hbar} \frac{e^4}{\varepsilon^2 (2\pi)^3} \int_{E_{\min}}^{E_{\max}} \sum_{i,m,m'} \left| F_{\substack{n,n' \\ m,m'}} \left(k_1, k_2, k_i, k_i - (k_1 - k_2)\right) \right|^2 \\ \times \left[JDOS_{m,m'} \left(k_i - (k_1 - k_2), k_i\right) \right] DOS_{n'}(k_2) \, dE_{n'}(k_2) \end{aligned} \tag{3.87}$$

as the impact ionization scattering rate. Calculating equation (3.87) is extremely computationally expensive. At high energies, the overlap integral is reported to be isotropic in nature, therefore it can be approximated to a constant (Kamakura1994). This greatly reduces the computation time. Figure 3.11 shows the impact ionization rate for a 2 nm x2 nm Si nanowire. The slope at high energies is very close to the slope obtained from the bulk calculations which is fitted by the relation $W(E) = 2 \times 10^{11} (E - E_g)^{4.6}$.

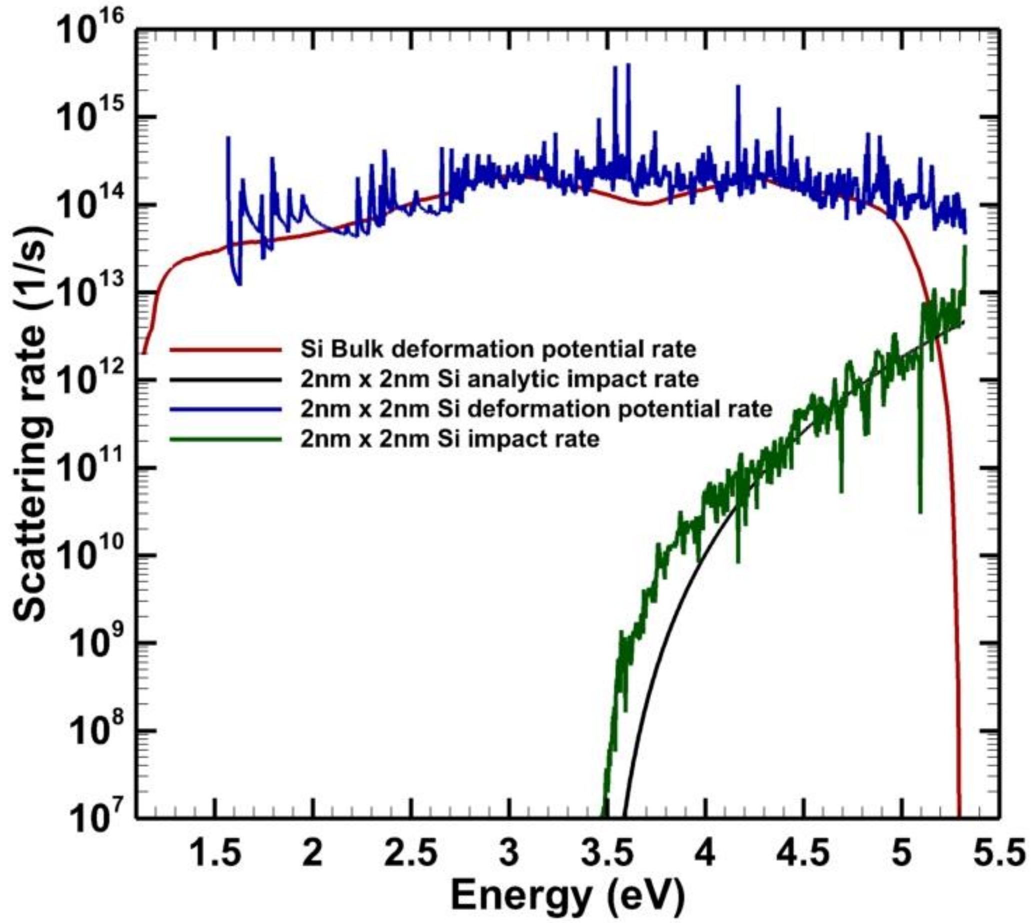

Figure 3.11: Plot of impact ionization rate and deformation potential scattering rate for a 2 nm x 2 nm Si nanowire along [100] and Bulk Si along [100]. The analytical formula is fitted to $W(E) = 2 \times 10^{11} \left(E - E_g\right)^{4.6}$.

3.3. Speed Optimizations for Scattering Rate Calculations

In all the scattering rates described above the overlap integral can be broadly defined as

$$F_{n,n'}\left(k_1,k_2\right)=\sum_{\mu,\nu}C_{\mathrm{n},\mu}\left(k_1\right)C^*_{n',\mu}\left(k_2\right)C_{\mathrm{m},\nu}\left(k_2\right)C^*_{\mathrm{m'},\nu}\left(k_1\right)e^{iq_x\cdot\left|\tau_{\mu,x}-\tau_{\nu,x}\right|}G\left(a_{diff}\right) \quad (3.88)$$

where $a_{diff}=\sqrt{\left(\tau_{\mu,y}-\tau_{\nu,y}\right)^2+\left(\tau_{\mu,\mathrm{z}}-\tau_{\nu,\mathrm{z}}\right)^2}$. The summation is over all the coefficients of the tight binding wave function. This is a large number and is equal to the size of the matrix used to calculate the eigenvalues of the nanowire. Calculating the overlap integral is therefore very time consuming. To simplify equation (3.88), we note that summation over μ and ν are only coupled to each other for different $\tau_{\mu,x}$, $\tau_{\mu,\mathrm{y}}$ and a_{diff} . For an unstrained crystal structure, the number of unique combinations of those quantities is of the order of the number of atoms in the super cell. This is shown in Figure 3.12. Equation (3.88) can then be written as

$$F_{n,n'}\left(k_1,k_2\right)=\sum_i A_{n,n'}\left(k_1,k_2,i\right)e^{iq_x\cdot\left|\tau_{\mu,x}-\tau_{\nu,x}\right|}G\left(a_{diff}\right) \quad (3.89)$$

where the summation is over the number of different combinations. If the size of the matrix is N, then assuming an $sp^3d^5s^*$ TB method including the spin-orbit interaction, the number of atoms is $M = N/20$. If the number of combinations is of the order of M, then to calculate $A_{n,n'}(k_1 ,k_2 ,i)$ from equation (3.89) , requires a first summation over N to store the product combinations of different orbitals on the same atom together and then M x N_{combos} to store the different combinations. This reduces the coputation time from N^2 to $N + M$ x $N_{combos} + N_{combos}$. This greatly reduces the computational time in calculating the overlap integral when $N_{combos} \sim M = N/20$.

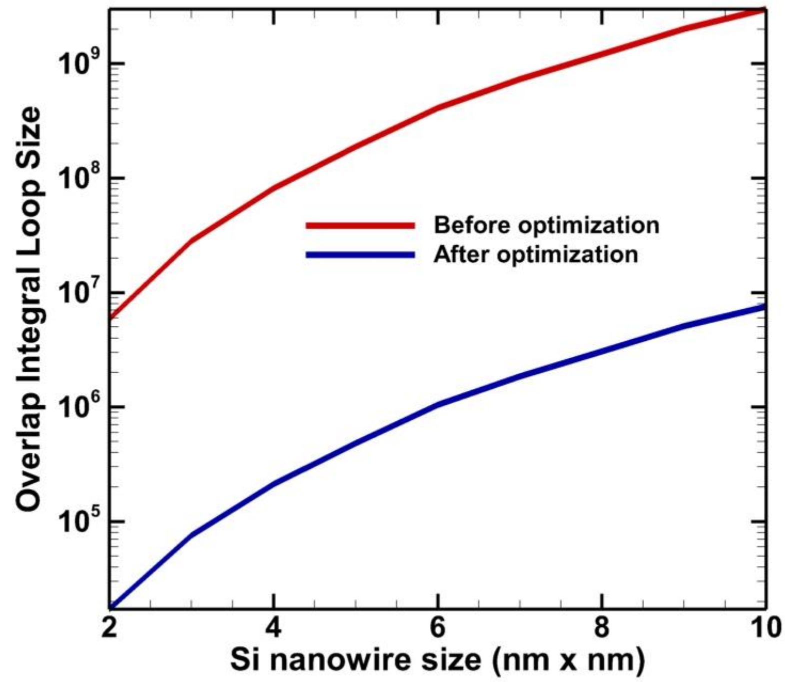

Figure 3.12: Comparison between the loop size of the overlap integral before the optimization equation (3.88) and after the optimization equation (3.89) as a function of a Si nanowire width size.

4. LOW FIELD AND HIGH FIELD TRANSPORT IN NANOWIRES

With the band structure and scattering rates calculated, a uniform field Monte Carlo simulation can be run to obtain the mobility, velocity-field curves, energy loss as well as other transient behavior (velocity overshoot). At low fields, though, it is simpler to solve the Boltzmann transport equation using the Rode's method (Rode1975). Rode's is useful to extract material parameters such as low-field mobility. It directly and exactly solves the Boltzmann transport equation for very low electric fields.

4.1. Rode's Method for 1D and 3D systems

The Boltzmann transport equation (BTE) with Fermi-Dirac statistics for the case of steady-state conditions and no spatial gradients can be written as

$$
\begin{aligned}
-\frac{e}{\hbar}\mathbf{F}.\nabla_{\mathbf{k}} f_{\mu}\left(\mathbf{k}\right) = \sum_{\mathbf{k}',\nu} S_{\nu,\mu}\left(\mathbf{k}',\mathbf{k}\right) f_{\nu}\left(\mathbf{k}'\right)\left[1-f_{\mu}\left(\mathbf{k}\right)\right] \\
-\sum_{\mathbf{k}',\nu} S_{\mu,\nu}\left(\mathbf{k},\mathbf{k}'\right) f_{\mu}\left(\mathbf{k}\right)\left[1-f_{\nu}\left(\mathbf{k}'\right)\right]
\end{aligned}
\tag{4.1}
$$

where $\mathbf{F} = F\mathbf{u}$ is the electric field vector applied to the system along direction $\mathbf{u}$, $S_{\mu,\nu}\left(\mathbf{k},\mathbf{k}'\right)$ is the scattering rate from state $\mathbf{k}$ at band index μ to state $\mathbf{k}'$ at band index ν and $f_{\mu}\left(\mathbf{k}\right)$ is the probability distribution function of state $\mathbf{k}$ at band index μ. Solution of equation (4.1) with a variety of approximations is essentially the basis of various transport methods such as the drift-diffusion method, the Monte-Carlo method (Jacoboni1983), the Rode's method etc. Rode's method is a low-field approximation that

in the limit of $F \to 0$ exactly solves the steady state BTE for a particular system. It is therefore very useful to use the Rode's method to extract low-field material properties such as mobility. In the 3D case equation, equation (4.1) is solved assuming a linear shift in the distribution function that is proportional to the applied electric field

$$f(\mathbf{k}) = f_0(\mathbf{k}) + eFg(\mathbf{k}) \tag{4.2}$$

where $g(\mathbf{k})$ is an unknown function representing the change in distribution function along the direction of the applied field, $f_0(\mathbf{k})$ is the equilibrium Fermi-Dirac distribution function and F is the applied electric field. Substituting equation (4.2) into equation (4.1) and ignoring higher order terms we get,

$$g_\mu(\mathbf{k}) = \frac{\frac{e}{\hbar}F.\nabla_{\mathbf{k}} f_{0,\mu}(\mathbf{k}) + \sum_{\mathbf{k}',\nu} g_\nu(\mathbf{k}')\left[S_{\mathbf{k}',\mathbf{k}}\left(1 - f_{0,\mu}(\mathbf{k})\right) + S_{\mathbf{k},\mathbf{k}'} f_{0,\mu}(\mathbf{k})\right]}{\sum_{\mathbf{k}',\nu}\left[S_{\mathbf{k}',\mathbf{k}} f_{0,\nu}'(\mathbf{k}') + S_{\mathbf{k},\mathbf{k}'}\left(1 - f_{0,\nu}'(\mathbf{k}')\right)\right]} \tag{4.3}$$

and the mobility is given by

$$\mu = -e\frac{\sum_\mu \int g_\mu(\mathbf{k})\mathbf{u}.\mathbf{v}_\mu(\mathbf{k})d\mathbf{k}}{\sum_\mu \int f_{0,\mu}(\mathbf{k})d\mathbf{k}} \tag{4.4}$$

For the case of one-dimensional transport one can directly solve for $f_\mu(k)$ in equation (4.4) to give

$$f_\mu(k) = \frac{\sum_{k',\nu} S_{\nu,\mu}(k',k) f_\nu(k') - \frac{e}{\hbar}F.\nabla_k f_{0,\mu}(k)}{\sum_{k',\nu} S_{\nu,\mu}(k',k) f_\nu(k') + \sum_{k',\nu} S_{\mu,\nu}(k,k')\left[1 - f_\nu(k')\right]}, \tag{4.5}$$

Once the distribution function is obtained, the mobility can be calculated using equation (4.6)

$$\mu_{F\to 0} = \frac{\sum_{\mu}\int\left(v_{\mu}(k)\cdot F\right)f_{\mu}(k)dk}{|F|^{2}\sum_{\mu}\int f_{\mu}(k)dk} \tag{4.6}$$

where the summation is over all the bands. The equilibrium distribution function is a Fermi-Dirac distribution function with the Fermi level calculated from the charge neutrality equation applied to the nanowire bands for a given acceptor or donor doping concentration.

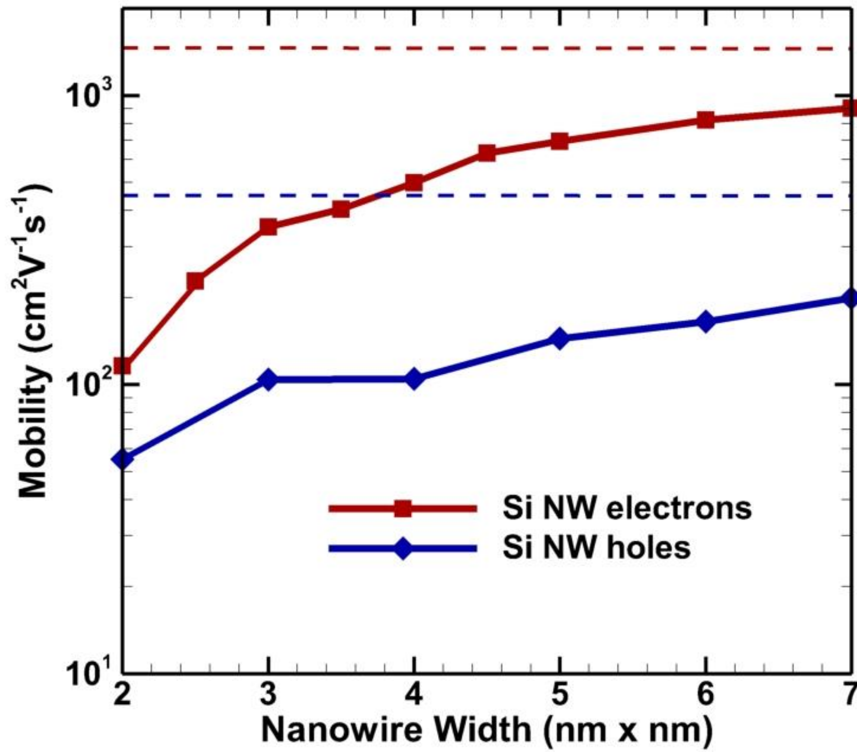

Figure 4.1: Variation of the phonon limited electron and hole mobility of Si nanowire along [100] with nanowire width. The dotted lines indicate the bulk mobility calculated using the Rode's method.

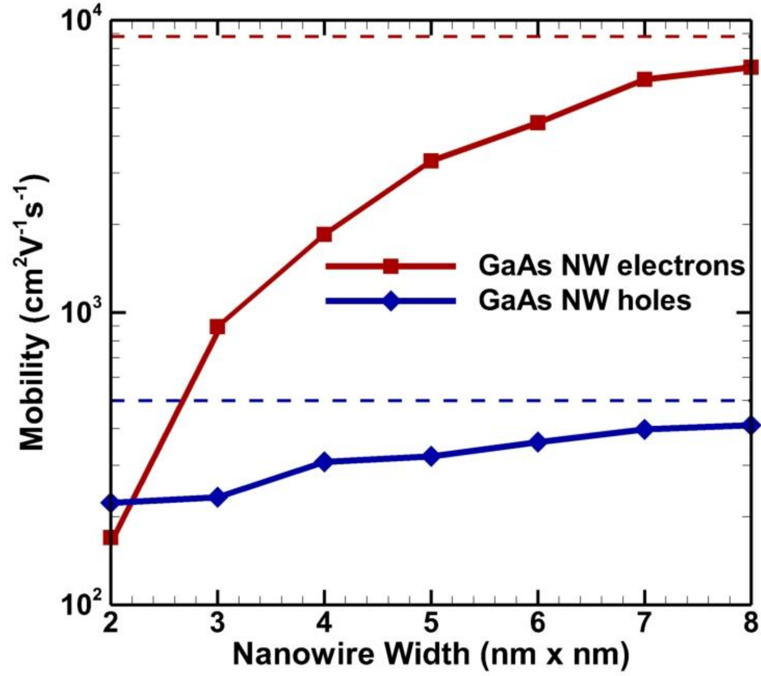

Figure 4.2: Variation of the phonon limited electron and hole mobility of GaAs nanowire along [100] with nanowire width. The dotted lines indicate the bulk mobility calculated using the Rode's method.

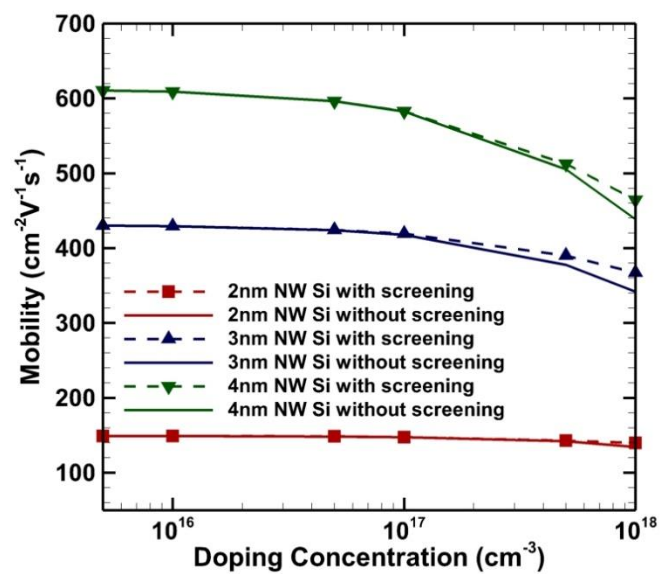

Figure 4.3: Variation of the electron and hole mobility of Si nanowire along [100] with the doping concentration with and without screening.

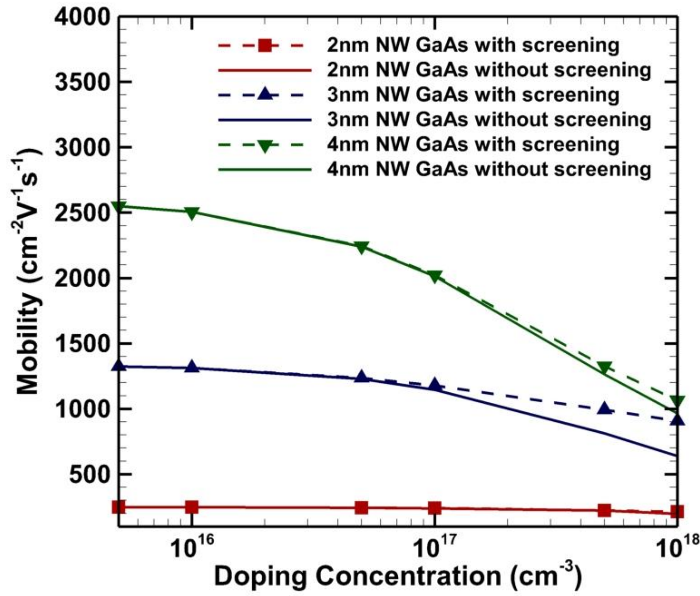

Figure 4.4: Variation of the electron and hole mobility of GaAs nanowire along [100] with the doping concentration with and without screening.

Figures 4.1 and 4.2 show the variation of the phonon limited mobility with nanowire width for Si and GaAs electrons and holes. At larger nanowire widths the mobility tends to the bulk mobility calculated using the Rode's method and indicated with dotted lines. The same scattering parameters were used to calculate the nanowire mobility and bulk material mobility. Figures 4.3 and 4.4 show the variation of the phonon limited mobility with the doping concentration with and without the dielectric screening calculated in chapter 3. As the dielectric matrix is very complicated to calculate, to simplify the calculations, the long wavelength is assumed ($q \rightarrow 0$) and the dielectric constant is calculated using the following formula

$$\varepsilon_D(q_x) = \left[1 + \sum_n \frac{e^2}{(2\pi)^2 \varepsilon_s} \int_{k_x} F_{n,n}(k_x, q_x) L_{nn}(q_x, \omega)\right] \tag{4.7}$$

4.2. Uniform Field Monte Carlo Simulations

The low field analysis is useful to extract physical quantities like the mobility as was shown in the previous section. Unfortunately, to analyze the material under high field conditions a different approach needs to be taken. Solving equation (4.5) for fields not tending to zero is very difficult. The gridding of the k-space has to be very fine and the iterations of the equations regularly diverge. In order to obtain distribution functions for high field conditions, the Monte Carlo method is used.

The Monte Carlo method is a stochastic method used to solve the Boltzmann transport equation. The Boltzmann transport equation can be modified according to (Ferry1991) to obtain

$$\begin{aligned} f(\mathbf{p},t) &= f(\mathbf{p},0)\exp\left(\int_o^t \Gamma_0 ds'\right) \\ &+ \int_0^t ds \int d\mathbf{p}' W(\mathbf{p},\mathbf{p}'-e\mathbf{E}s) f(\mathbf{p}'-e\mathbf{E}s)\exp\left(-\int_o^t \Gamma_0 ds'\right) \end{aligned} \tag{4.8}$$

where

$$\Gamma_O = \int d\mathbf{p}' W(\mathbf{p}',\mathbf{p}) \tag{4.9}$$

and s is a variable along the trajectory of phase space and each coordinate can be parameterized as a function of this variable as

$$\mathbf{r} \to \mathbf{x}^*(s), \quad \mathbf{p} = \hbar\mathbf{k} \to \mathbf{p}^*(s), \ \ t \to s \tag{4.10}$$

Equation (4.8) is the Chamber-Rees path integral (Rees1972) and is the form of the Boltzmann transport equation which can be iteratively solved. In order to make the above equation solvable a useful mathematical trick introduced by Rees (1968) is used in which we make the complicated energy dependent function Γ_0 into an energy independent term, thereby making the term inside the integral in equation (4.8) trivially solvable. This is done by introducing a scattering term called self-scattering (Γ_{ss}). Self-scattering does not change the momentum or the energy of the particle and therefore does not change the physics of the particle. What this term does however is to convert the energy dependent function Γ_0 into an energy independent term by defining

$$\Gamma_{ss}(\mathbf{p}) = \Gamma_T - \Gamma_0(\mathbf{p}) \tag{4.11}$$

Therefore, equation (4.8) becomes

$$f(\mathbf{p},t) = f(\mathbf{p},0)e^{-\Gamma_T t} + \int_0^t ds \int d\mathbf{p}' W(\mathbf{p},\mathbf{p}' - e\mathbf{E}s) f(\mathbf{p}' - eEs) e^{-\Gamma_T s} \tag{4.12}$$

where

$$W^*(\mathbf{p},\mathbf{p}') = W(\mathbf{p},\mathbf{p}') + \Gamma_{ss}(\mathbf{p}')\delta(\mathbf{p} - \mathbf{p}') \tag{4.13}$$

The first term of equation (4.12) is a transient term while the second term is the term which can be iteratively solved. If we look at the second term closely, the first integral over $d\mathbf{p}'$ represents the scattering of the distribution function f out of state $\mathbf{p}$ to state $\mathbf{p}' - \mathrm{e}\mathbf{E}\mathrm{s}$. The second integral represents the integration along the trajectory s and the exponential is just the probability that no scattering takes place during the time it moves a distance s. Thus if we look at how the electrons move physically it consists of a

scattering event determined by the first integral, and then there is a free-flight motion (no scattering) for a time interval t_s. Rees showed that the time steps t_s correlate to $1/\Gamma_T$.

The scattering rates are calculated according to the formulae described in chapter 3. The parameters used in the calculation of the scattering rates are fitted by comparing the velocity field curves obtained from the uniform field Monte Carlo simulations with experimental data and comparing the mobilities obtained from the Rode's method to the experimentally obtained mobility values. Figures 4.5 and 4.6 shows the fit between the velocity field curves for bulk Si and bulk GaAs for electrons and holes respectively.

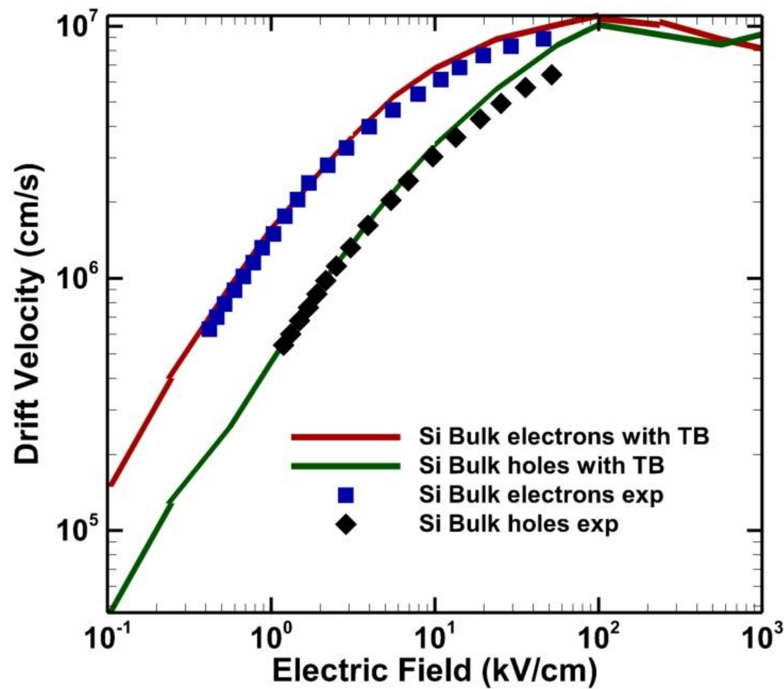

Figure 4.5: Comparison of drift velocity versus electric field for electrons and holes, between Monte Carlo simulations of bulk Si and experimental data using the Tight Binding method. The experimental data is taken from Canali (1975).

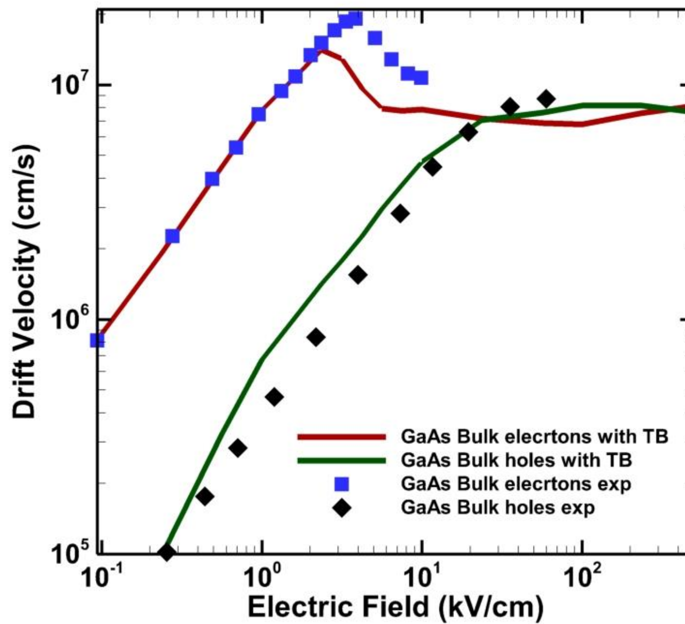

Figure 4.6: Comparison of drift velocity versus electric field for electrons and holes, between Monte Carlo simulations of Bulk GaAs and experimental data using the Tight Binding method. The experimental data for electrons is taken from Pozela (1979) and from Dalal (1971) for holes.

Once the parameters for the scattering rates are fit for the bulk material, the same parameters are then used for the nanowire materials. This way there is no extra parameter required to simulate transport with nanowire structures.

The Monte Carlo method allows us to see the position of the carriers after a simulation for a 3 nmx3 nm GaAs NW. This gives a physical insight into the electron position not possible in other simulations. Figure 4.7 shows the change in carrier population as the electric field changes and Figure 4.8 and 4.9 shows the transient

electron velocity and electron energy at different electric fields. As the electric field increases the carriers populate higher bands and are more widespread in the BZ.

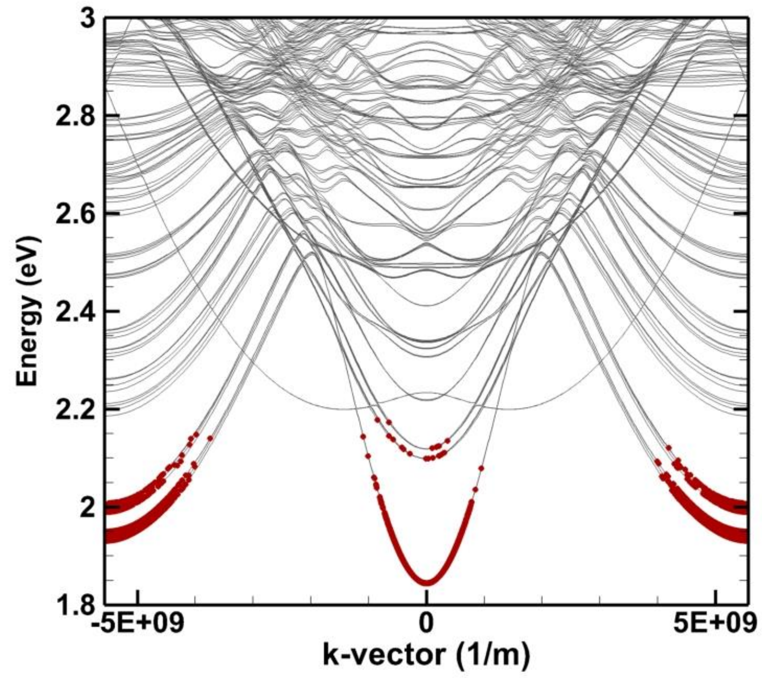

a)

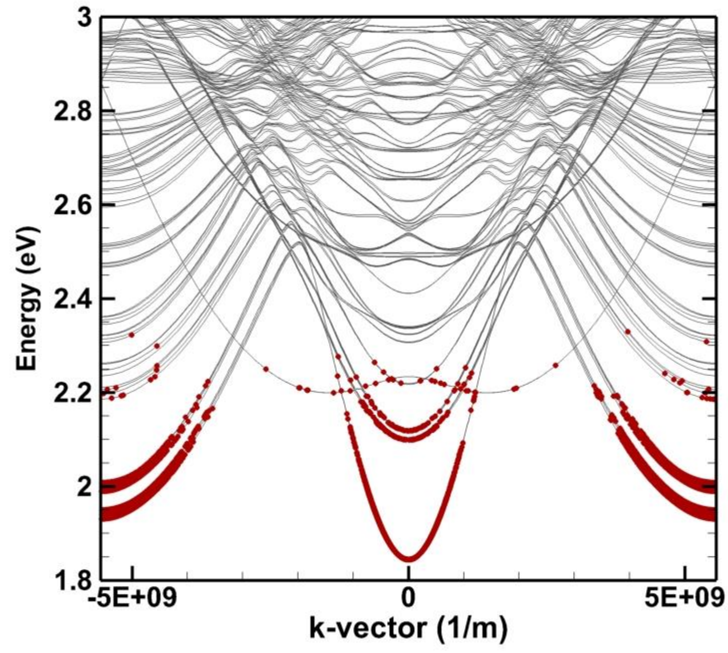

b)

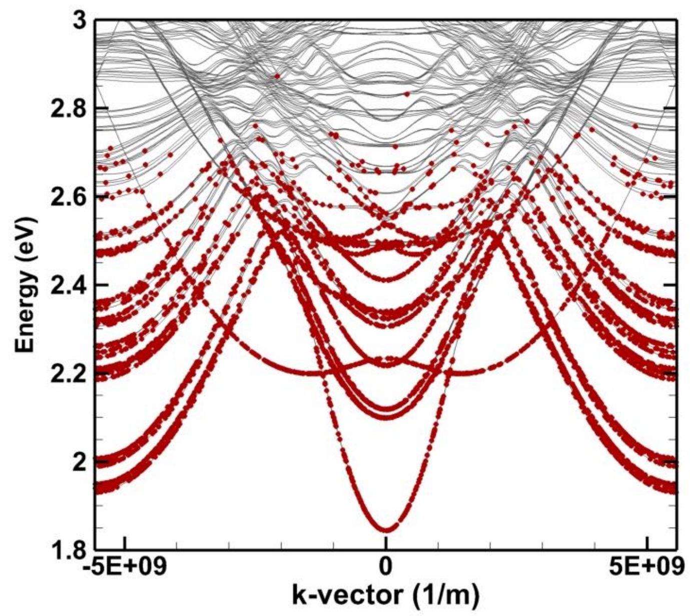

c)

Figure 4.7: Carrier population at steady state in a 3 nm x 3 nm GaAs nanowire along [100] for a) 1.0 kV/cm, b) 10 kV/cm and c) 100 kV/cm. Each red dot represents an electron. The grey lines represent the band structure.

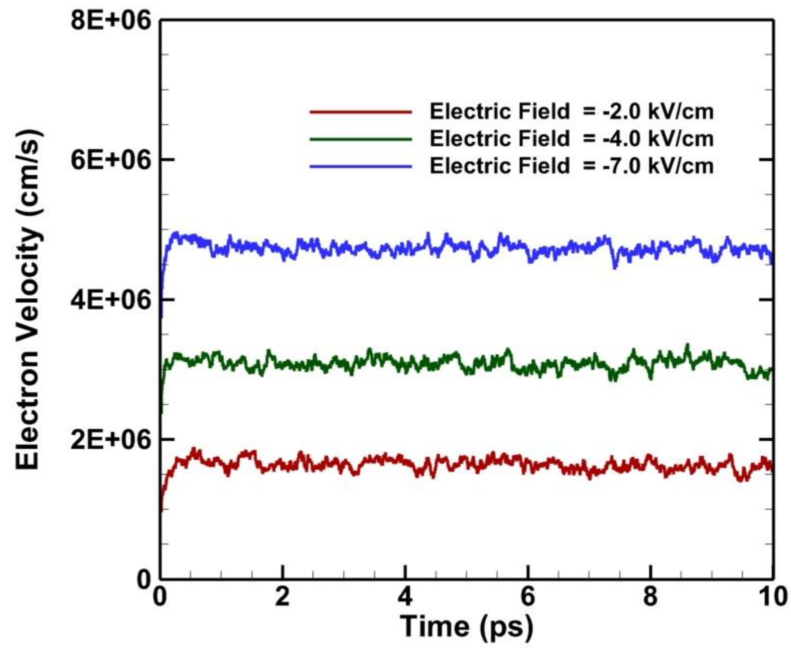

Figure 4.8: Transient plot of electron velocity for a 3 nm x 3 nm GaAs nanowire along [100] for different electric fields.

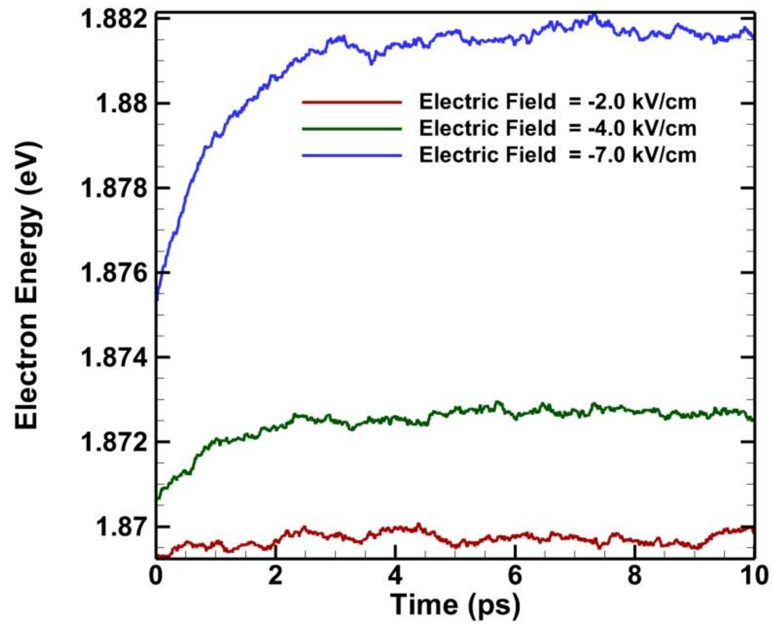

Figure 4.9: Transient plot of total electron energy for a 3 nm x 3 nm GaAs nanowire along [100] for different electric fields.

4.3. Multiband Transport in Nanowires

The full band Monte Carlo method (FBMC) is used to simulate high field transport in a variety of materials. The traditional method requires the calculation and storage of the band structure of the material on the full Brillouin zone (BZ). The acceleration of carriers in the presence of an electric field is accomplished using the free-flight drift routine detailed in Jacoboni (1983), which involves moving all the carriers according to the Bloch acceleration theorem for a time t and then scattering the carriers according to their rates previously calculated at the end of the so-called free flight.

The free-flight drift routine is a single band model in which the carrier are assumed to remain in the same band during drift. This model does not work well at band crossings or

when the energy separation between the bands are small. At band crossings, it is difficult to maintain the carrier's band identity because the bands are sorted in energy after being calculated in an eigenvalue solver, there is no unique band identifier. Therefore when a carrier reaches a band crossing, for example, it is unclear which band it follows (Fischetti1991). An electric field can induce inter band transitions (Nilsson2001) when the energy separation between the bands are small, and the electric field sufficiently large. This effect becomes prominent in materials such as nanowires where the energy spacing between the bands is small and the bands intercross and anti-cross frequently across the Brillouin Zone (BZ). The utility of the multi-band drift model is to replace the traditional free-flight drift routine in single band Monte Carlo models. After a carrier undergoes a drift for a particular duration of time, there is a finite possibility of it undergoing a transfer to the other bands. Various approaches have been proposed to incorporate carrier transitions between different bands such as the overlap test (Bellotti2000), and the velocity continuity method (Brennan2000). Both these methods have drawbacks that the transition rate does not depend on the electric field and is sensitive to the mesh size (Bertazzi2009). Krieger and Iafrate (KI) have developed a set of equations which give the transition probability of a carrier under an electric field as a function of time (Krieger1987) when solved. These equations are a series of complex partial differential equations, which were previously solved using the 4th order (RK4) Runge-Kutta method (Bertazzi2009). Since this method is computationally expensive of, the KI equations were previously only solved on a small part of the BZ in bulk materials, where band crossings were expected to result in interband tunneling at high electric fields. In nanowires, the band crossings and interband tunneling can occur throughout the

BZ due to the dense nature and mixing of the bands. Therefore, a fast and full BZ wide solution of the KI equations is necessary to properly account for interband tunneling in nanowires, as well as providing a more computationally efficient algorithm for treating bulk materials as well.

We present for the first time numerical calculations of the multi-band transport and interband tunneling in nanowires. A new method of solving the KI equations is also presented which greatly improves the accuracy and speed of the simulation.

4.3.1. Krieger and Iafrate (KI) Equations

The Krieger and Iafrate (KI) equations provides the solution of the time-dependent Schrödinger equation for Bloch waves under an electric field described by (Krieger1987)

$$H\psi(\mathbf{r},t) = \left[\frac{\left[\mathbf{p} - (e/c)\mathbf{A}\right]^2}{2m} + v(\mathbf{r}) \right] \psi = i\hbar \frac{\partial \psi}{\partial t} \tag{4.14}$$

where

$$\mathbf{A} = -c\int_0^t F(t')dt' \tag{4.15}$$

and $v(\mathbf{r})$ is the crystal periodic potential, c is the speed of light and $F(t)$ is the time varying electric field. Substituting

$$\psi(\mathbf{r},t) = \sum_n C_n(t)\phi_n'(\mathbf{r},t) \tag{4.16}$$

In to equation (4.14), where $\phi_n'(\mathbf{r},t)$ is the solution to the eigenvalue problem

$$\left[\frac{\left[\mathbf{p}-(e/c)\mathbf{A}\right]^2}{2m}+v(\mathbf{r})\right]\phi_n^{'}(\mathbf{r},t)=\varepsilon_n(t)\phi_n^{'}(\mathbf{r},t) \tag{4.17}$$

where $\varepsilon_n(t)$ are the eigenvalue solutions, we get the KI equations

$$i\hbar\frac{\partial C_n(t)}{\partial t}=\varepsilon_n(t)C_n(t)+eF(t)\sum_{n'}X_{n,n'}(t)C_{n'}(t) \tag{4.18}$$

where $F(t)$ is the time dependent electric field, $-e$ is the electronic charge, $\varepsilon_n(t)$ is the eigenvalue of the nth band with wave vector $k(t)$, and $C_n(t)$ are time dependent coefficients and the X matrices given by

$$X_{n,n'}(k(t))=-i\int_{\Omega}u^*_{n,k(t)}(x)\nabla_k u_{n',k(t)}(x)d^3x \tag{4.19}$$

where Ω is the volume of the primitive cell, and $u_{n,k(t)}$ is the Bloch function for band n for wave vector $k(t)$. The wave vector $k(t)$ is determined from the Bloch acceleration theorem

$$\hbar\frac{\partial k(t)}{\partial t}=-eF(t) \tag{4.20}$$

where e is the charge of the carrier.

4.3.2. Solution of the KI Equations

Previous methods to solve the Krieger and Iafrate equations have used the Runge-Kutta method of the 4th order (RK4) to solve equation (4.18). This method required solving the coupled complex partial differential equations for every possible initial condition (n possible conditions if there are n bands), which is numerically expensive as

the time step required to solve the KI equations using the RK4 method can be very small (~10^{-18} s to ~10^{-19} s). This time step becomes more problematic at higher electric fields as the time steps need to be readjusted increasingly smaller according to the electric field). Solutions to the KI equations are assumed to be correct if $\sum_n |C_n(t)|^2 \approx 1$. The probability coefficients rapidly diverge if the time step is too large, so one has to continuously check the sum and recalculate it if it is too large.

A more elegant solution can be obtained by using the Magnus expansion (Magnus1954). Writing equation (4.18) in matrix notation we get

$$\frac{\partial C(t)}{\partial t} = C(t)\,\mathrm{A}(t) \tag{4.21}$$

where $C(t)$ is an $n\times 1$ matrix and $A(t)$ is an $n\times n$ matrix where n is the number of bands and each element is given by

$$A_{nn'}(t) = \begin{cases} \dfrac{\varepsilon_n(t)}{i\hbar} - \dfrac{eF(t)}{i\hbar} X_{nn}(t) & n = n' \\ -\dfrac{eF(t)}{i\hbar} X_{nn'}(t) & n \neq n' \end{cases} \tag{4.22}$$

Due to the nature of the problem, k-space and time are synonymous and related to each other by equation (4.20), it is easier to operate over k-space rather than time, and therefore converting from dt to dk, equation (4.21) can be written as

$$\frac{\partial C(k)}{\partial k} = C(k)\,\mathrm{A}(k) \tag{4.23}$$

where

$$A_{nn'}(k)=\begin{cases}-\dfrac{i\varepsilon_n(k)}{eF(k)}+iX_{nn}(k) & n=n' \\ iX_{nn'}(k) & n\neq n'\end{cases} \tag{4.24}$$

Applying the Magnus expansion to equation (4.23) we get

$$C(k_f)=\exp\left[\Omega(k_f)\right]C(k_i) \tag{4.25}$$

where

$$\Omega(k_f)=\sum_{j=1}^{\infty}\Omega_j(k_f) \tag{4.26}$$

The first two terms of the infinite series expansion are given by (Blanes2009)

$$\Omega_1(k_f)=\int_{k_i}^{k_f}A(k_1)\,dk_1 \tag{4.27}$$

$$\Omega_2(k_f)=\frac{1}{2}\int_{k_i}^{k_f}\int_{k_i}^{k_1}\left[A(k_1),A(k_2)\right]dk_2\,dk_1 \tag{4.28}$$

where k_i is the value of the wave vector when $t=0$ and k_f is the wave vector at $t=t_1$, and $\left[A(k_1),A(k_2)\right]=A(k_1)A(k_2)-A(k_2)A(k_1)$ is the commutator operator. A recursive procedure to generate the 2nd and higher terms in the Magnus expansion is given by

$$\Omega_n(k_f)=\sum_{j=1}^{n-1}\frac{B_j}{j!}\int_{k_i}^{k_f}S_n^j(k)\,dk \tag{4.29}$$

where

$$\begin{aligned}S_n^j(k)&=\sum_{m=1}^{n-j}\left[\Omega_m(k),S_{n-m}^{j-1}(k)\right]\\ S_n^1(k)&=\left[\Omega_{n-1}(k),A(k)\right]\end{aligned} \tag{4.30}$$

where B_j are the Bernoulli numbers. The main advantage of the Magnus solution is that very often, the truncated series still has important qualitative properties of the exact solution (Iserles1999). For example, regardless of the truncation of the Magnus series, $\sum_n |C_n(\mathrm{k})|^2$ is always equal to 1 due to the unitary nature of the solution. In fact this is a property shared by all exponential perturbation methods such as the Fer method (Fer1958) and the Wilcox method (Wilcox1967). This is not true in the case of RK4 methods or other perturbation methods like the Dyson series method.

Solving equation (4.25) requires the calculation of the exponential of a matrix. The calculation of the matrix exponential is usually numerically expensive for large matrices and scales as the cube of the matrix size, but in this case, the size of the matrix is the number of bands, which even in the case of nanowires, is at most 100. Also, once the matrix is computed, the final probabilities can be calculated by a simple matrix multiplication with the initial conditions, thus this approach is numerically advantageous over the RK method, in which the KI equations are simply recalculated for every possible initial condition.

To calculate the X matrices defined in equation (4.19) requires the calculation of the derivative of the Bloch function, $u_{n,k(t)}$. Two methods have been used to calculate the derivative, Rayleigh-Schrödinger perturbation theory (Schrödinger1926) and the finite difference method. Rayleigh-Schrödinger perturbation theory (RSPT) states that

$$\nabla_k u_n(k) = \sum_{n',\mathrm{n'}\neq \mathrm{n}} \frac{\langle u_{n',k} | \partial H(k)/\partial k | u_{n,k} \rangle}{\varepsilon_{n'}(k) - \varepsilon_n(k)} u_{n'}(k) \qquad (4.31)$$

where $H(k)$ is the tight binding Hamiltonian for the time independent Schrödinger equation

$$H(k)\psi_k = \varepsilon_k \psi_k \tag{4.32}$$

where ψ_k is the wave vector containing the Bloch functions $u_{n,k(t)}$. Inserting equation (4.31) into equation (4.19) and using the orthogonality of the Bloch functions we get

$$X_{n,n'}(k(t)) = \begin{cases} \dfrac{\langle u_{n',k} | \partial H(k)/\partial k | u_{n,k} \rangle}{\varepsilon_{n'}(k) - \varepsilon_n(k)} & n \neq n' \\ 0 & n = n' \end{cases} \tag{4.33}$$

For the case of degenerate bands at a certain $k(t)$, degenerate perturbation theory has to be used. The result of the X matrices obtained from using Rayleigh-Schrödinger perturbation theory is independent of the k-space gridding.

Using the finite difference method, the derivative of the Bloch function can be written as

$$X_{n,n'}(k(t)) = -i \int_\Omega u^*_{n,k(t)}(x) \left(\frac{u_{n',k(t)+dk/2}(x) - u_{n',k(t)-dk/2}(x)}{dk} \right) d^3x \tag{4.34}$$

which can be simplified to

$$X_{n,n'}(k(t)) = -\frac{i}{dk}\left[I_{n'k^+,n,k} - I_{n'k^-,n,k} \right] \tag{4.35}$$

where

$$I_{n'k^+,n,k} = \int_\Omega u^*_{n,k}(x).u_{n',k^+}(x).d^3x \tag{4.35}$$

is the overlap integral between two neighboring states, with $k^{\pm}(t) = k(t) \pm dk/2$ and dk is a small separation in k-space. If $n = n'$, the X matrix must be purely real to ensure

that $\sum_n |C_n(t)|^2 = 1$. This is enforced by setting the imaginary part to be 0 in equation (4.35) when $n = n'$, this result is similar to result obtained using Rayleigh-Schrödinger perturbation theory, where the X matrix value is 0 when $n = n'$. The phase of the wave functions must be treated carefully as detailed in (Lindefeldt2004) to obtain smoothly varying X matrices in the complex plane across the BZ. To compare the two methods, the X matrices were calculated on a fine k-space grid for a 3 nm$\times$3 nm InAs nanowire along [100]. Figure 4.10 shows the value of the magnitude of X using both methods.

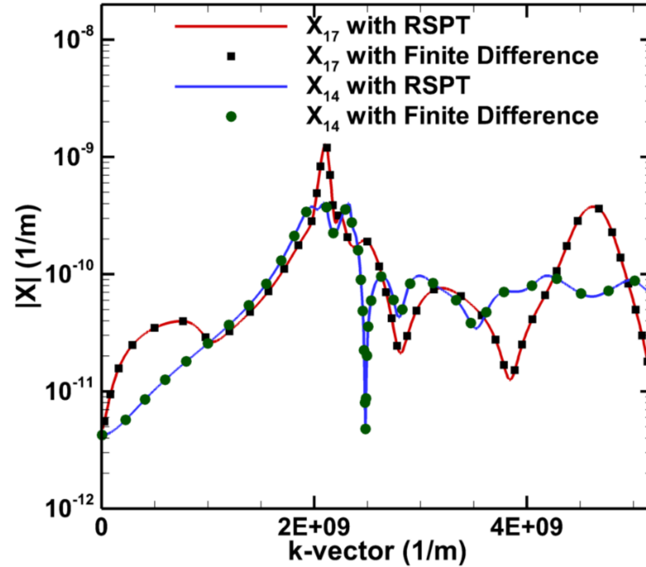

Figure 4.10: The magnitude of the X matrix between band 1 and band 7, and band1 and band 4 in a 3 nm x 3 nm InAs nanowire along [100]. The symbols represent values obtained using Rayleigh-Schrödinger perturbation theory (RSPT) and the line represents values obtained using the finite difference method.

As can be seen in Figure 4.10, the finite difference method is just as accurate as the perturbation method for a fine k-space grid. The 1D BZ was equally divided into 2400 grid points on which the band structure was calculated. In all the simulations in this work, the finite difference method was used to calculate the X matrices.

4.3.3. Numerical Solution of the KI Equations in Nanowires

The band structure of the nanowire is calculated in the present work on a discrete k-space grid using the empirical tight binding method with the $sp^3d^5s^*$ orbitals including spin (Luisier2006). Since the k-space is divided into discrete k-cells, the solution of the probability coefficients from equation (4.25) at the $(i+1)^{th}$ cell is given by

$$C(k_{i+1}) = \exp(\Omega^{\sim}) C(k_i) \tag{4.37}$$

where $\Omega^{\sim}$ is the truncated Magnus series expression from equation (4.26). As can be seen from equations (4.27) to (4.29) the higher order terms of the Magnus series are numerically expensive to compute and involve several nested integrals. To solve numerically, the X matrices are calculated at discrete k-points and then linearly interpolated between them. The energy in between the k-points is interpolated using a quadratic scheme. The individual terms of the Magnus series can be calculated using a Gaussian quadrature of the nested integrals in equations (4.27) and (4.28). The value of $\Omega^{\sim}$ up to the 4th order in k is given by (Iserles1999)

$$\Omega^{\sim} = \Omega_1 + \Omega_2 \tag{4.38}$$

$$\Omega^{\sim} = \frac{1}{2} h \left[A_1 + A_2 \right] - \frac{\sqrt{3}}{12} h^2 \left[A_1, A_2 \right] \tag{4.39}$$

where $k_{i+1} = k_i + h$ and

$$\begin{aligned} A_1 &= A\left(k_i + \left(\frac{1}{2} - \frac{\sqrt{3}}{6}\right)h\right) \\ A_2 &= A\left(k_i + \left(\frac{1}{2} + \frac{\sqrt{3}}{6}\right)h\right) \end{aligned} \tag{4.40}$$

where $\left[A_1, A_2\right]$ represents the commutator operator. The value of the coefficients at the next grid point is then calculated using equation (4.37). The exponential of the matrix is calculated using the method described in (Moler2003). The 4th order Magnus (MG4) integrator described in equation (4.39) has been previously used to solve linear differential equations with a very high accuracy (Wen-cheng2006, Aparicio2005). Figure 2 shows the difference between using just Ω_1, and using both Ω_1 and Ω_2 in equation (4.38) in solving the KI equations. Even though the difference is small, in this work both Ω_1 and Ω_2 are used to solve the KI equations. It should be noted once again, that even though we use just 2 terms of the Magnus series, we obtain a 4th order accurate solution in k.

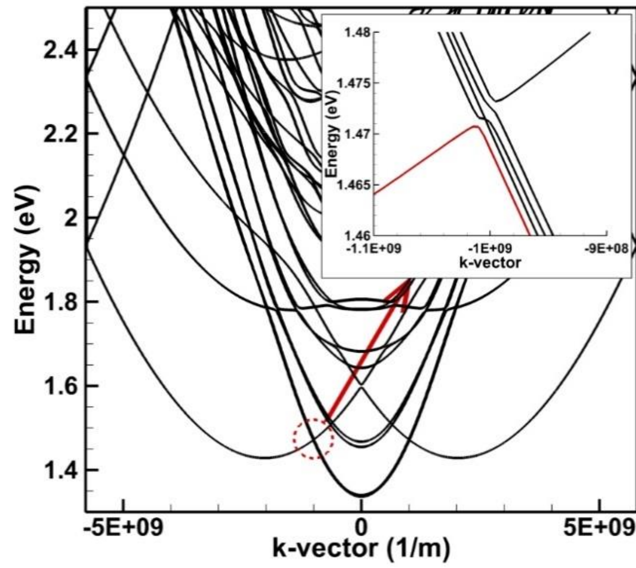

a)

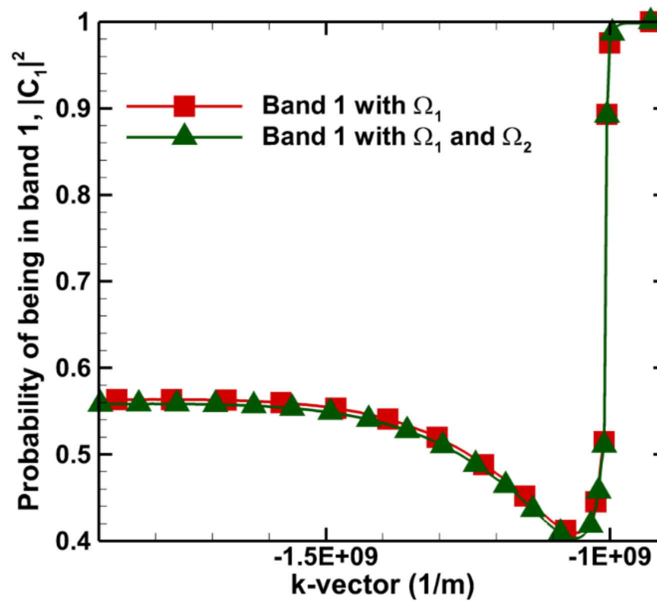

b)

Figure 4.11: (a) The conduction band of a 3 nm×3 nm Si nanowire along [100]. The inset shows a magnified section of the band structure highlighting a crossing. (b) The

difference between using the 1st term and both the 1st and 2nd terms in the Magnus expansion on the probability coefficients for the region of the band structure shown in the inset of Figure 4.11 (a). The electron is initialized in the 1st band shown in red under an electric field of 10 kV/cm. The square symbols represent values obtained using just the 1st term and the delta symbols represent values obtained using both the 1st and 2nd term of the Magnus expansion.

Aparicio (2005) has shown that the operation counts for a single time/k-vector step for a MG4 method scales as $6n^2+5n^3$ while the RK4 method scales as $10n^2$, where n is the matrix size. In our particular case, we need the probability coefficients for each permutation of initial conditions, so the RK4 method has to be resolved for every possible initial condition while the MG4 method needs to perform an additional n $[n\times n][n\times 1]$ matrix multiplications (an additional n^2 operations n times) to obtain the final probability coefficients. The total operation counts then becomes $6n^2+6n^3$ for the Magnus 4th order and $10n^3$ for the RK4 method for a single time/k-vector step. Therefore, for the same step size, the solutions of the KI equations using the Magnus 4th order method provides a slightly better form of solution, although they both scale as $\mathrm{O}(n^3)$. A limiting factor in the case of the Magnus 4th order method is the computation of the matrix exponential ($5n^3$). Nevertheless, the key difference between the RK4 method and the MG4 method lies with the choice of the time/k-vector step size. The MG4 method being inherently exponential in nature, more accurately captures the exact solution and therefore a coarser step size can be used. On the other hand, the RK4

method is a polynomial approximation and requires a much smaller step size, typically two orders of magnitude less.

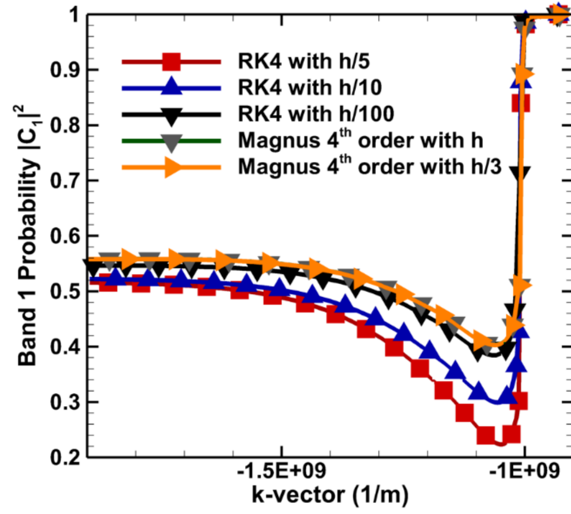

a)

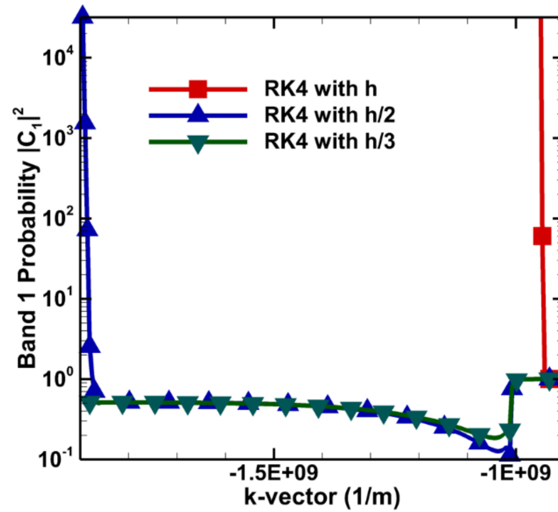

b)

Figure 4.12: (a) The difference between using different step sizes for the Magnus 4th order and the Runge-Kutta 4th order (RK4) method. The region of the band structure simulated is shown in Figure 4.11 (a) inset. The band 1 is highlighted in red. (b) The sensitivity of the RK4 method to coarse step sizes is shown. h is the step size on which the band structure is calculated.

Figure 4.12 (a) shows the variation of the probability coefficient for band 1 after passing through a band crossing. The MG4 method is highly accurate for the standard step size over which the band structure is calculated. Reducing the step size by a factor of 3 does not change the result in any significant way. However, the RK4 method requires a much finer step to obtain an accurate solution. Therefore, for a reasonably accurate solution, the RK4 method would be 100 times slower when evaluating the above band crossing. Also the RK4 method is very unstable if the step size is below a certain size. As seen in Fig. 4.12 (b), dividing the original step size by a factor of 1, 2 and 3 can significantly change the result and cause it to runaway exponentially if the step size is too large. This effect is problematic since there is no way of knowing the correct step size beforehand. Therefore, one has to adopt a step size and then recalculate the problem with a smaller step size till is reasonably close to 1.0. This approach is numerically expensive, and adopting the MG4 method over the RK4 method improves the computational time significantly (at least by 100 times in the above case).

4.3.4. Implementation of the KI Equation Solution within the Monte Carlo Method

As mentioned in the Introduction, the free-flight drift model of the standard Monte Carlo algorithm needs to be modified to account for interband transitions. A charge carrier undergoes drift for a particular duration of time in the presence of a given electric field, and during this free flight period, there is a finite possibility of it undergoing a transferring to other bands. Therefore, one would ideally like to solve the KI equations for every carrier during its free-flight, at its current position in k-space, and calculate the probability of undergoing a transition to other bands. However, this is impractical as there are typically anywhere between 10^7 – 10^{11} carrier drifts in a traditional Monte Carlo routine, and a significant increase in the computational time for each carrier free flight greatly affects the overall simulation run time. A less computationally expensive approach taken here is to create a lookup table, storing the transition probabilities for every possible initial condition and for a finite number of points in k-space. During runtime, depending on the carrier's initial band and the position in k-space, the corresponding transition probability table is pulled up and a random number is used to decide the final band of the carrier after at the end of the free flight. The memory required to store the transition probability tables is negligible compared to the already existing cost of storing the scattering tables within the full band Cellular Monte Carlo (CMC) scheme (Saraniti2000). The algorithm described above, and the results presented in the next section, apply to the case of simulation in a uniform electric field (so-called k-space simulation). However, the look-up table approach can be

generalized to different fields as well, with the size of the look-up table still much less than the scattering tables used in the CMC algorithm.

To implement the above idea, a step size Δk for the k-space grid is required. The grid on which the band structure is calculated is usually too coarse. To identify the correct Δk, a minimum electric field $F_{\min}$ is used. Below $F_{\min}$, the effect of multi-band drift is assumed to be unimportant, and Δk can then be calculated as

$$\Delta k = \frac{eF_{\min} t_{drift}}{\hbar} \tag{4.41}$$

The 1D BZ is then divided equally into N k-points separated by Δk where N is given by,

$$N = \frac{2\pi}{a\Delta k} \tag{4.42}$$

where a is the periodicity of the supercell along the nanowire axis. The KI equations are solved for the duration of the drift and the transition probabilities for every k-point and initial band index, are then stored for a particular electric field F and drift time, t_{drift}. The electric fields used in the uniform field simulation are then chosen to be integer multiples of $F_{\min}$. This is important so as to correctly capture the transition probabilities. If $F / F_{\min} = p$, where p is not an integer, then after a drift time t_{drift}, the final k-value of the carrier will be

$$k_f = k_i + p\Delta k \tag{4.43}$$

where k_i is the initial k-value. Since the transition probabilities are only stored for every Δk, there will be an error in the stored transition probabilities during the actual carrier drift. There still exists an error after a carrier undergoes a scattering event, as its

momentum will in general not lie on the k-points of the pre-calculated transition tables. To minimize this error, $F_{\min}$ must be chosen as small as computationally possible. In this work, $F_{\min}$ was chosen to be 2x10^5 V/m, which gives a Δk of 1.22×10^5 m^{-1} for a drift time of 4×10^{-16} s. This gives a total of N = 94,843 k-points in the finer k-space grid for [100] Si. The exponential in equation (4.37) is the transition probability from k_i to k_{i+1}. Depending on the electric field and drift time, the final transition probability matrix is calculated by successively multiplying the matrices for the required number of k-cells obtained using equation (4.43)

$$C(k_f) = T_f \ldots\ldots T_{i+2} T_{i+1} T_i C(k_i) \tag{4.44}$$

Once the final transition matrix from k_i to k_f is calculated, the probability coefficients for every possible initial condition is calculated and stored.

In the present work, the Si and InAs nanowire band structures are calculated using the semi-empirical $sp^3d^5s^*$ Tight Binding (TB) model including spin. Deformation potential scattering rates are calculated from the TB coefficients using the method outlined in Chapter 3. Impact ionization is not included in this work. The carriers (electrons and holes) are initialized according to a one-dimensional Maxwell distribution at room temperature. The traditional full band Monte Carlo approach is then performed with the inclusion of the modified free-flight drift routine to account for the inter band transitions after the free flight.

4.3.5. Effect of Interband Tunneling on Transport in Nanowires

The usefulness of the KI equations is the ability to simulate a field dependent probability of interband transitions. In Figure 4.13 (a), a section of 3 nm$\times$3 nm InAs nanowire band structure along [100] is magnified to demonstrate interband tunneling. The electron is initially in band 1, shown in red in the inset of Figure 4.13 (a) and undergoes drift for different constant electric fields. The initial k-point is -3.3×10^{9} m^{-1} and the final k-point is -4.4×10^{9} m^{-1}. The probability of the electron being in various bands is presented as $|C|^{2}$ and is shown in Figures 4.13 (b), 4.13 (c) and 4.13 (d) for electric fields of 10kV/cm, 100 kV/cm and 1 MV/cm, respectively.

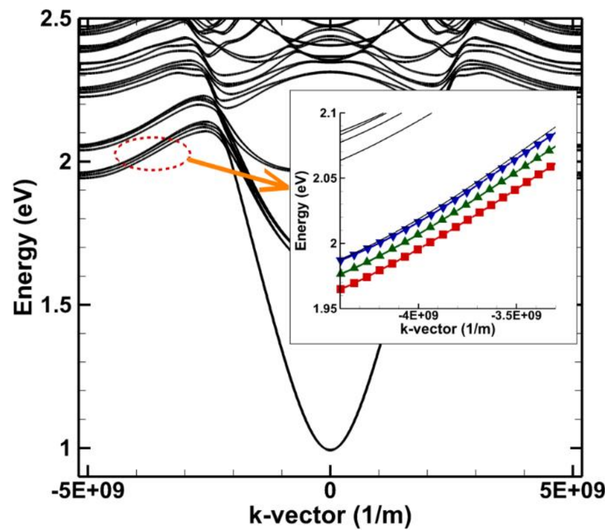

a)

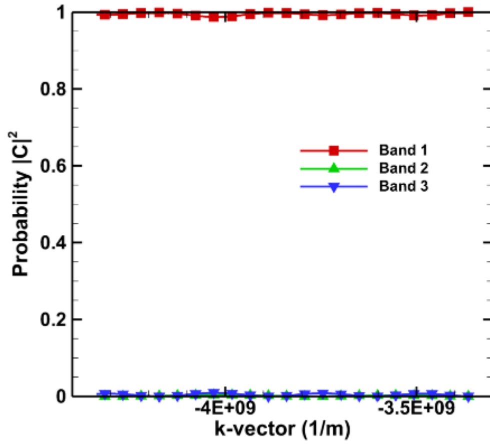

b)

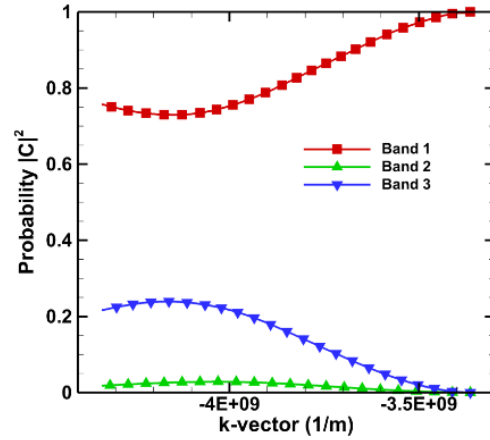

c)

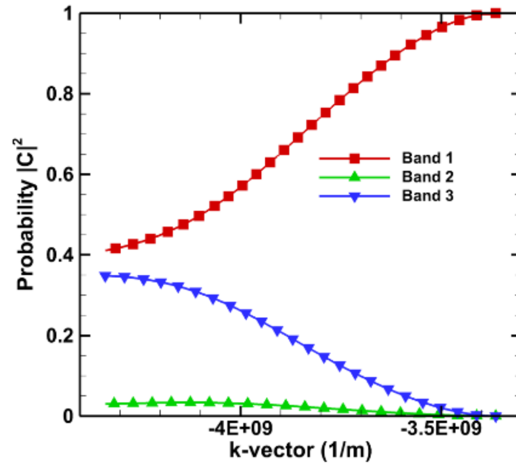

(d)

Figure 4.13: (a) Band structure of a 3 nm×3 nm InAs nanowire band structure along [100]. The inset shows a magnified part of the band structure showing bands close to one other. The 1st band is represented by square symbols, the 2nd band by left triangles and the 3rd band by right triangles. (b) Plot of transition probabilities as a function of $k(t)$ under an applied electric field of (b) 10kV/cm, (c) 100 kV/cm and (d) 1 MV/cm for the first three bands at the location shown in the inset of Figure 4.12 (a).

At 10kV/cm, the probability of remaining in band 1 is close to unity since the electric field is not high enough to induce interband transitions as can be seen in Figure 4.13 (b) for the energy separation between bands of Figure 4.13 (a). As can be seen in Figure 4.13 (c) and Figure 4.13 (d), at higher electric fields of 100kV/cm and 1MV/cm, the electron tunnels to the 2nd and 3rd band with increasingly higher probability with field, with the highest probability being to the 3rd band even though the energy separation between the 1st and 3rd band is higher than that between the 1st and 2nd bands. This somewhat non-intuitive result is due to the fact that the X matrices are higher between the 1st and 3rd band as compared to the 1st and 2nd band due to the overlap of the wave functions related to symmetry.

A similar case is shown for a 3 nm$\times$3 nm Si nanowire along [100] in Figure 4.14 (a), where we have the case of an actual band crossing/anti-crossing. The initial k-point is -9.0×10^{8} m^{-1} and the final k-point is -1.9×10^{9} m^{-1}. The band crossing/anti-crossing occurs at -1.0×10^{9} m^{-1}. Due to the very low energy separation near the band crossing, interband tunneling occurs even at electric fields as low as 1.0 kV/cm, as shown in Figure 4.14 (b). As the carrier drifts across the band crossing, the probability that the electron remains in the 1st band reduces drastically. The probability of transition is independent of the electric field in this case since the energy bands are very close to one other. In equation (4.24) when the energy difference between bands goes to 0, the KI equations become independent of the electric field as is evident in Figure 4.14 (b) and 4.14 (c). Therefore inter band tunneling is very important and requires an accurate solution of the KI equations across the full BZ.

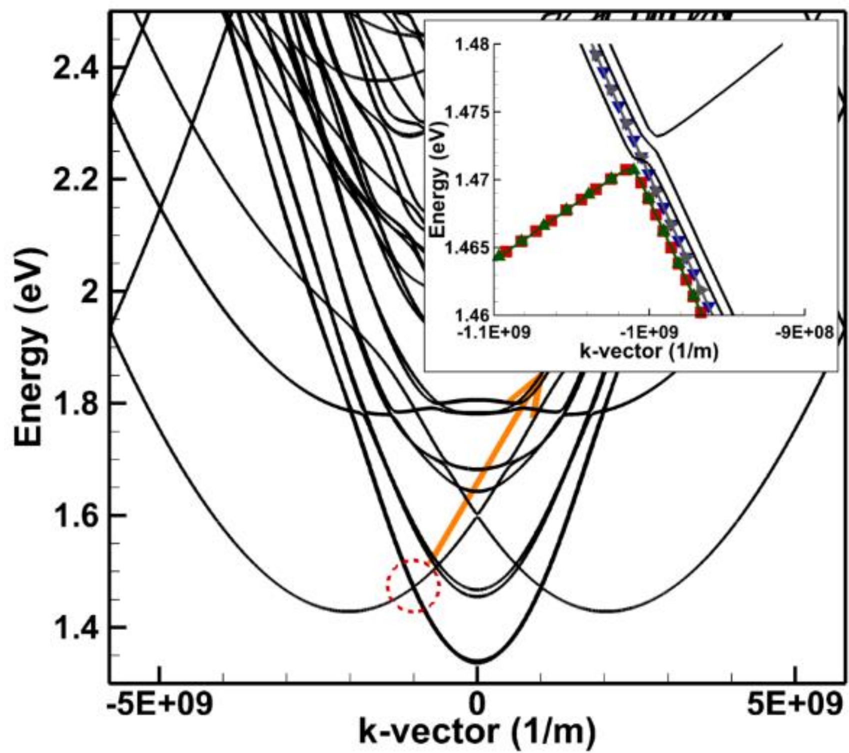

(a)

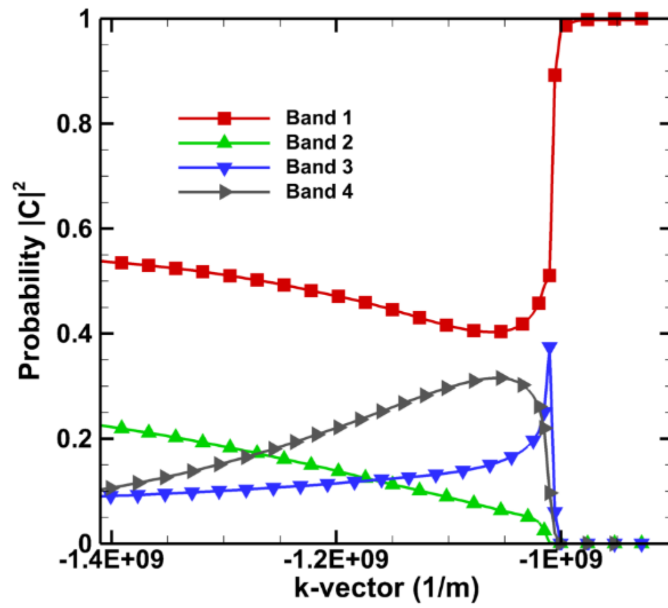

b)

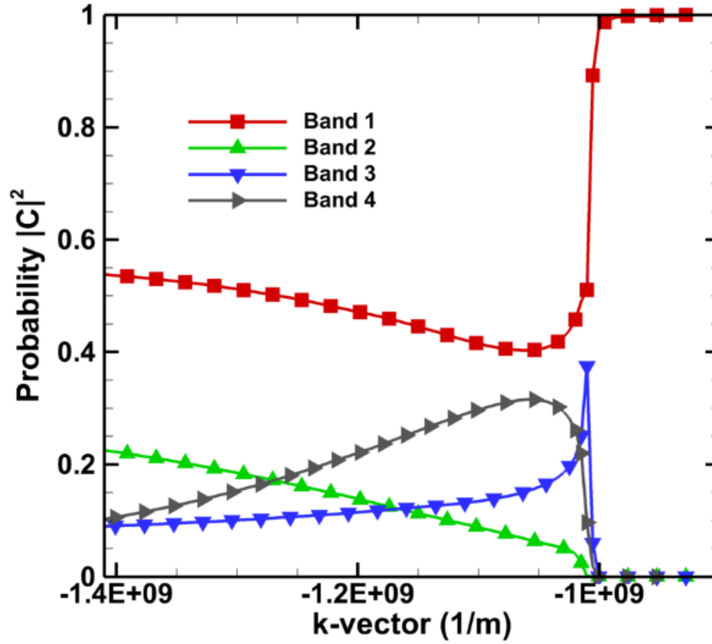

c)

Figure 4.14: (a) Band structure of a 3 nm$\times$3 nm Si nanowire along the [100] direction. The inset shows a magnified part of the band structure showing a band crossing. The first four bands are colored and marked. (b) Plot of transition probabilities as a function of $k(t)$ under an applied electric field of (b) 1.0 kV/cm and (c) 100 kV/cm for the first four bands at the band crossing shown in the inset of (a).

In Figures 4.15 and 4.16, the effect of the multi-band drift model on the average kinetic energy of the carriers from a uniform field Cellular Monte Carlo simulation are shown.

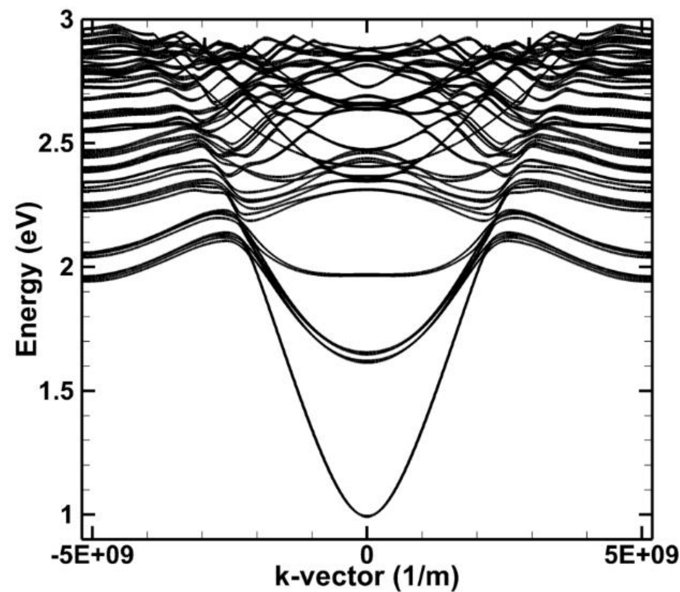

a)

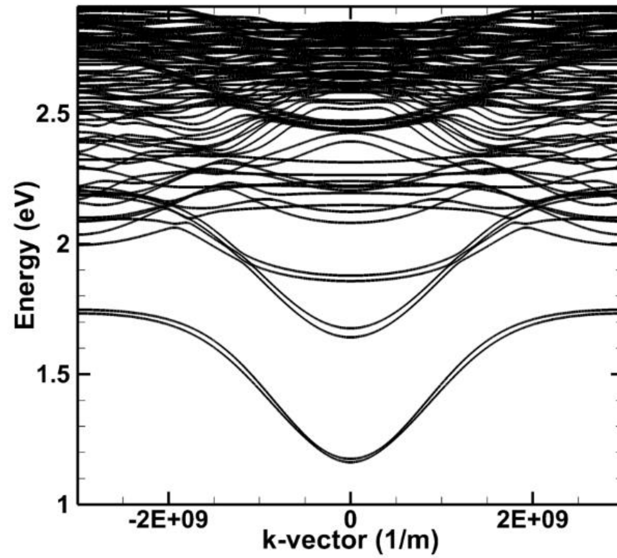

(b)

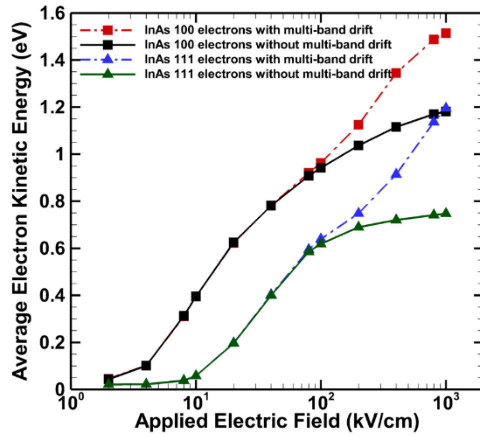

(c)

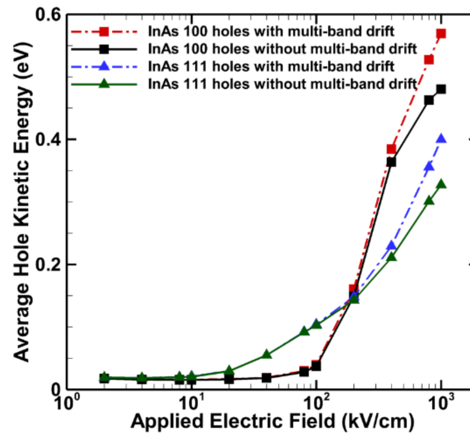

(d)

Figure 4.15: (a) Conduction band structure of 3 nm×3 nm InAs nanowire along [100]. (b) Conduction band structure of 3 nm×3 nm InAs nanowire along [111]. (c) Plot of average electron kinetic energies in 3 nm×3 nm InAs nanowires along [100] and [111] with and without multi-band drift. (d) Plot of average hole kinetic energies in 3 nm×3 nm InAs nanowires along [100] and [111] with and without multi-band drift.

The effect of the multi-band drift is very apparent in the case of the electrons in 3 nm$\times$3 nm InAs nanowires. In Figure 4.15 (a) and Figure 4.15 (b), the conduction band of 3 nm$\times$3 nm InAs nanowires along the [100] and [111] directions are shown. In the [100] direction bands, there are several anti-crossings near 2.2 eV (K.E. ~ 1.2eV) which causes the energy to saturate in the absence of interband tunneling. The same situation is present in the [111] direction bands as there is a small band gap present between the first two conduction bands, and the rest of the conduction bands. This gap would only be crossable with inelastic scattering processes such as polar and non-polar optical phonon scattering in a traditional Monte Carlo. This effect becomes apparent with consideration of the average energy of the electrons, which saturate at 0.6eV above the conduction band minima as seen in Figure 4.15 (c). When the multi-band drift model is employed, the electrons achieve much higher energies due to interband tunneling. The average kinetic energy of the holes is plotted in Figure 4.15 (d). The average kinetic energies of the holes when multi-band drift model is used are higher than the case when it is not used, although the change in energy is not as high as it is in the case of electrons.

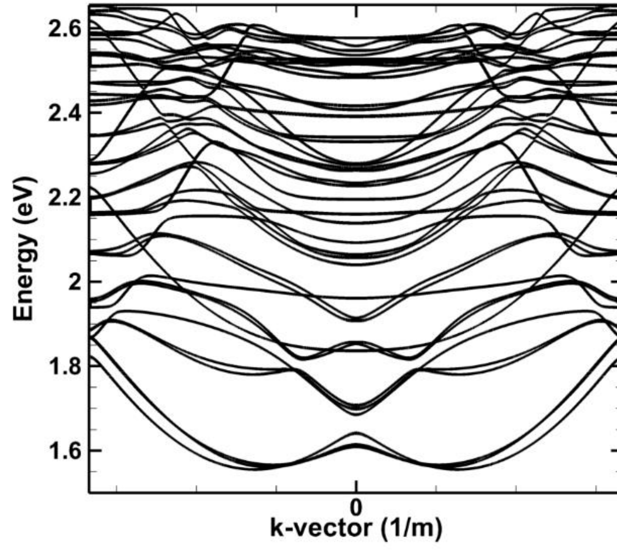

a)

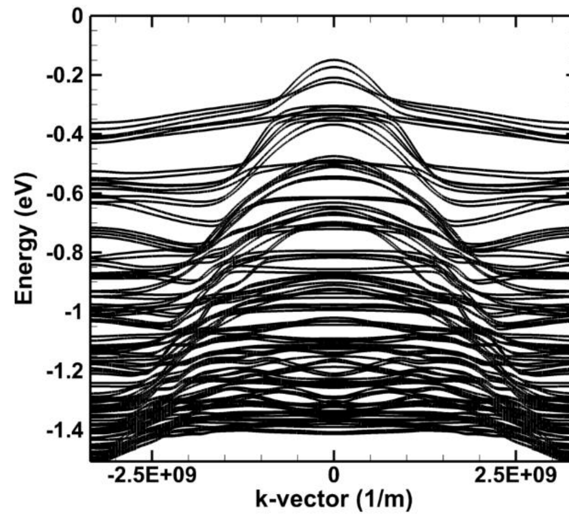

b)

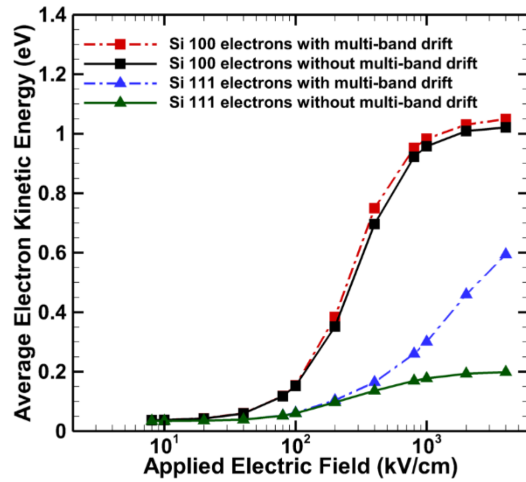

c)

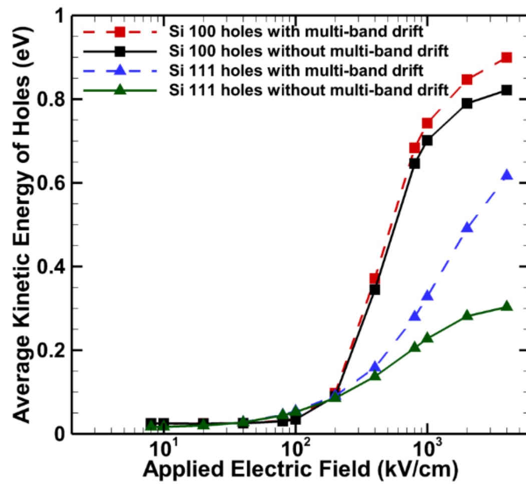

d)

Figure 4.16: (a) Conduction band structure of 3 nm×3 nm Si nanowire along the [111] direction. (b) Valence band structure of 3 nm×3 nm Si nanowire along the [111] direction. (c) Plot of average electron kinetic energies in 3 nm×3 nm Si nanowires along the [100] and [111] directions with and without multi-band drift. (d) Plot of average hole

kinetic energies in 3 nm×3 nm Si nanowires along the [100] and [111] directions with and without multi-band drift.

In Figures 4.16 (a) and 4.16 (b) the conduction and valence band of 3 nm×3 nm Si nanowire along the [111] direction is shown. In the case of the 3 nm×3 nm Si nanowire along the [111] direction, in the valence band shown in Figure 4.16 (b), there exists a number of band anti-crossings, therefore the carriers are unable to reach high energies with the traditional drift algorithm and the addition of the multi-band drift significantly increasesthe average energy. Similarly in Figure 4.16 (a), without the multi-band drift approach, the carriers' energy saturates as carriers are unable to reach high enough energies with just inelastic scattering, as can be seen in Figures 4.16 (c) and 4.16 (d). In the case of 3 nm×3 nm Si nanowires, the multi-band drift model makes more of a difference for [111] Si compared to [100] Si for both electrons and holes, due to the differences in bandstructure between the two in the direction of the electric field.

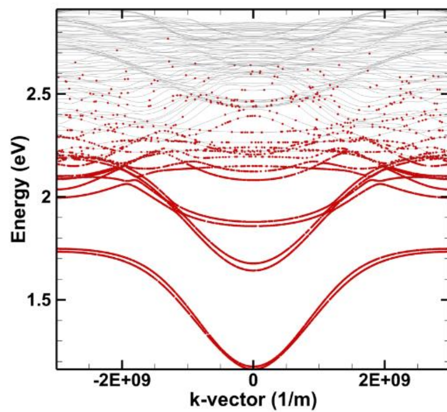

(a)

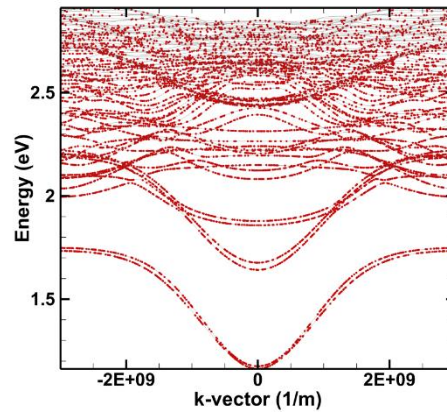

(b)

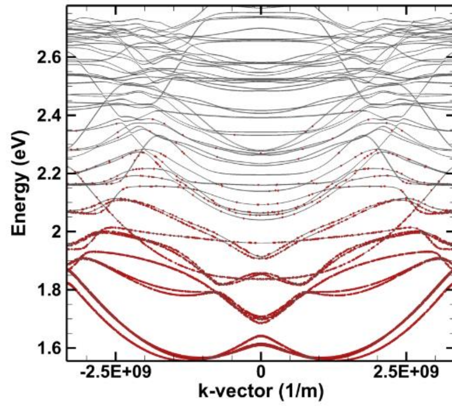

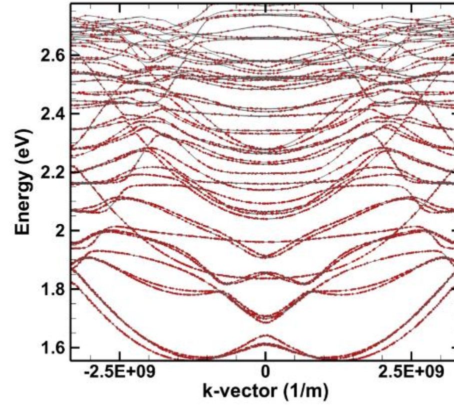

(c) (d)

Figure 4.17: (a) Snapshot of electrons in the conduction band of 3 nm×3 nm InAs along [111] at the end of the simulation without multi-band drift at 1MV/cm. Each red dot represents an electron. (b) Snapshot of electrons in the conduction band of 3 nm×3 nm InAs along [111] at the end of the simulation with multi-band drift at 1MV/cm. (c) Snapshot of electrons in the conduction band of 3 nm×3 nm Si along the [111] direction at the end of the simulation without multi-band drift at 4MV/cm. Each red dot represents an electron. (d) Snapshot of electrons in the conduction band of 3 nm×3 nm Si along the [111] direction at the end of the simulation with multi-band drift at 4MV/cm.

Figures 4.17 (a)-4.17 (d) demonstrate the difference in carrier populations with and without the inclusion of multi-band transport. In Figure 4.17 (a), a snapshot of 10000 electrons is shown for a 3 nm×3 nm InAs nanowire along the [111] direction at an electric field of 1MV/cm for the case of a conventional CMC simulation, where the electrons are unable to reach higher bands. When the multi-band drift algorithm is employed, carriers are able to access much high energies as is shown in Figure 4.17 (b).

A similar case for Si is shown in Figure 4.17 (c) and Figure 4.17 (d) at an electric field of 4MV/cm.

4.4. High Field Transport in Nanowires

Figures 4.18, 4.19, 4.20 and 4.21 show the average electron and hole drift velocity versus electric fields for different nanowire widths. As the nanowire widths increase the trend becomes closer to the curves obtained for the bulk materials. Except at high electric fields, the velocity of the nanowires does not show any velocity saturation which would be expected.

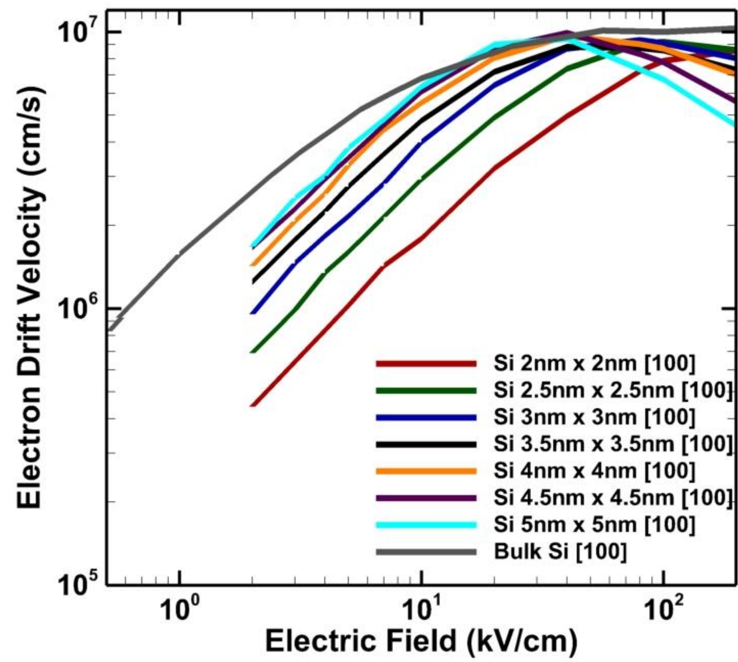

Figure 4.18: Electron drift velocity of Si nanowires along the [100] direction versus electric field for different nanowire widths. The drift velocity curve for bulk Si is also shown for comparison.

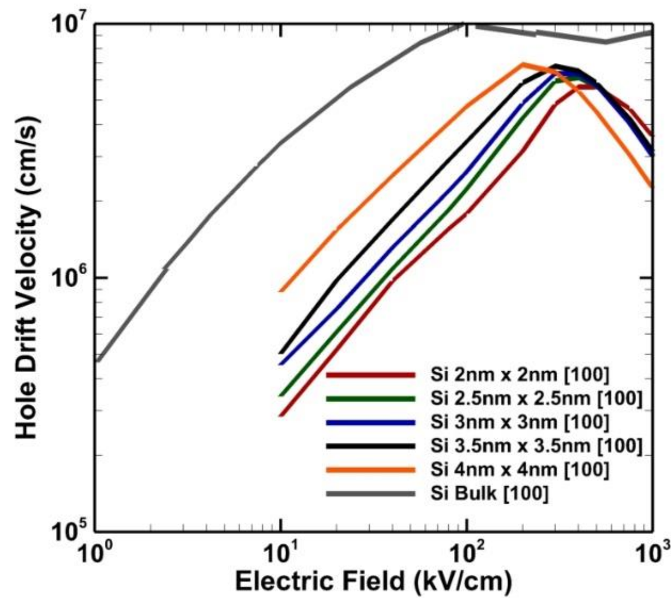

Figure 4.19: Hole drift velocity of Si nanowires along [100] versus electric field for different nanowire widths. Drift velocity curve for bulk Si is also shown for comparison.

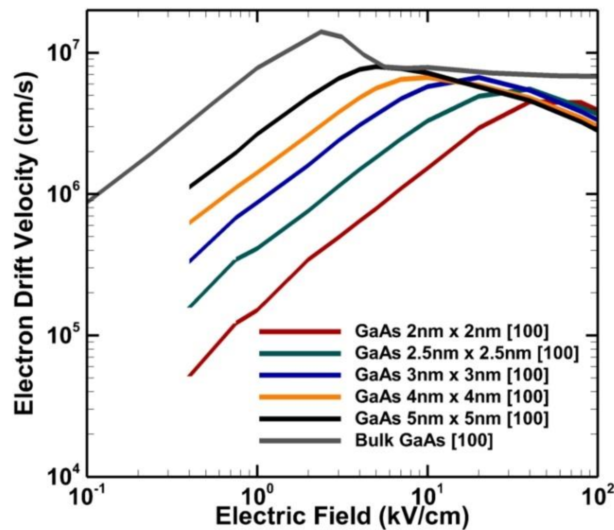

Figure 4.20: Electron drift velocity of GaAs nanowires along [100] versus electric field for different nanowire widths. Drift velocity curve for bulk GaAs is also shown for comparison.

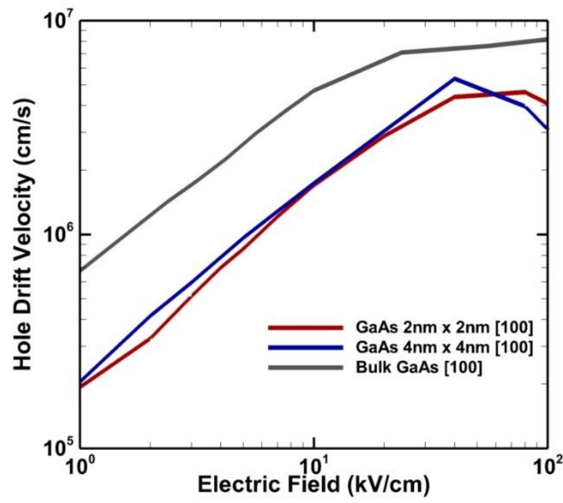

Figure 4.21: Hole drift velocity of GaAs nanowires along [100] versus electric field for different nanowire widths. Drift velocity curve for bulk GaAs is also shown for comparison.

5. ENERGY RELAXATION IN NANOWIRES

The analysis of energy relaxation rates are also possible using a uniform field Monte Carlo simulation. The scattering rates of the nanowire are calculated as shown in the previous chapters. A plot of the rate is shown in Figure 5.1. To simulate hot carrier relaxation during photoexcitation, the electrons are initialized with a mean energy corresponding to the excitation energy shown in Figure 5.2 and a Gaussian half-width of 100 meV. After a few picoseconds, the initial distribution thermalizes and the decay is exponential as shown in Figure 5.2. As shown in Figure 5.3, the relaxation rate in the NWs is increasingly slower compared to the bulk as the NW width is reduced, due to the 1D nature of the scattering rates.

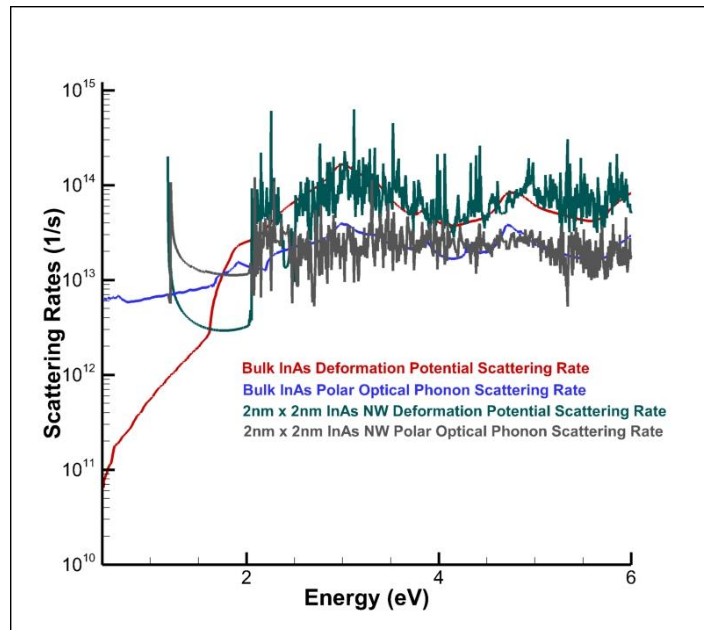

Figure 5.1: Scattering rates of a 2 nmx2 nm InAs NW compared with bulk.

At high fields an electron “runaway” effect is also observed. At low fields the distribution is Maxwellian with a temperature of 315K, but at high fields the distribution becomes more uniform due to the runaway effect (Dimitrev2000) as shown in Figure 5.4. This is attributed to the nature of the 1D scattering rates which decreases in value with increase in energy within a band as seen in the inset of Figure 5.4.

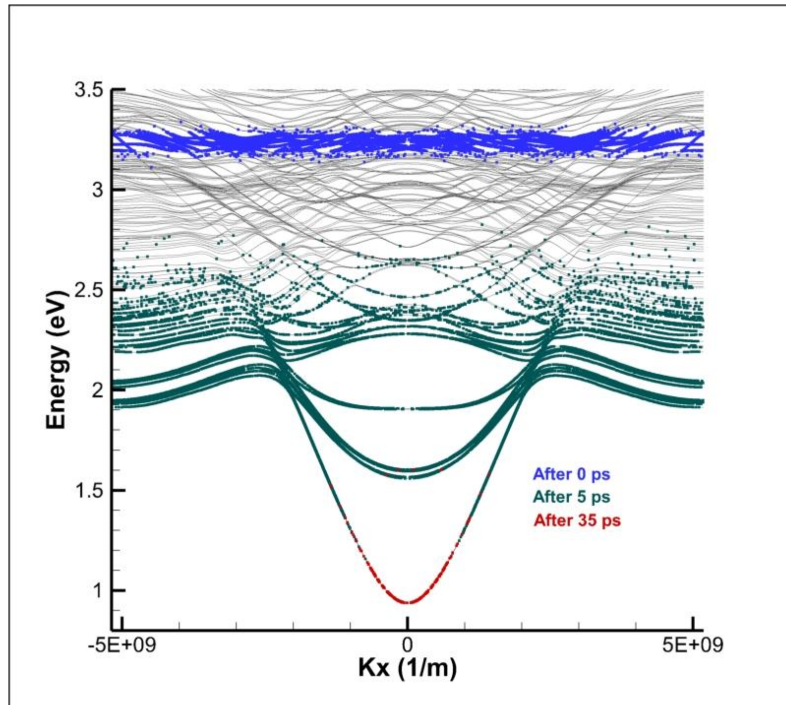

Figure 5.2: Carrier chart for a 3 nmx3 nm InAs NW with excited electrons at 2Eg for different times.

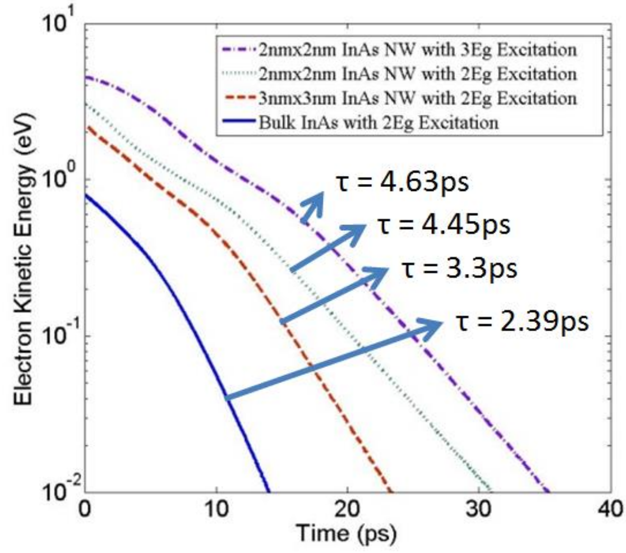

Figure 5.3: Energy relaxation of hot electrons in Bulk InAs, 2 nmx2 nm InAs NW [100] and 3 nmx3 nm InAs NW [100].

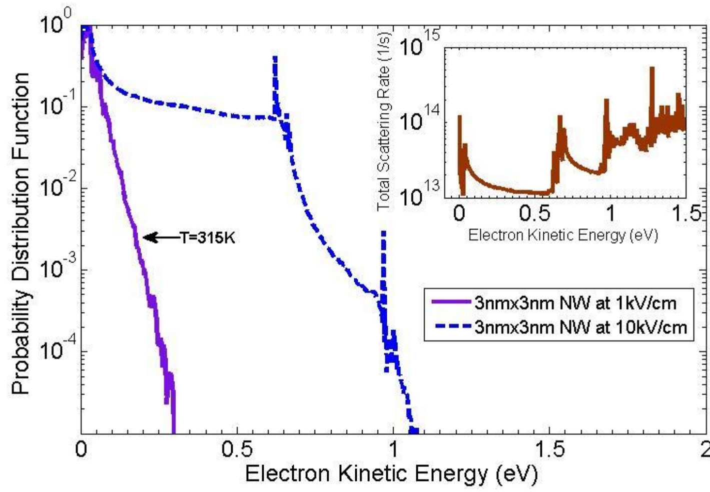

Figure 5.4: Distribution functions for different electric fields on a 3 nmx3 nm InAs NW [100].

5.1. Energy Relaxation in Cladded Nanowires

In this section we investigate the effect of cladding on the energy relaxation and multi-excitation generation of nanowires. The core nanowire is a square $In_{0.53}Ga_{0.47}As$ nanowire along [100] and the cladding material is InP which is lattice matched with $In_{0.53}Ga_{0.47}As$. A full band Monte-Carlo simulation is used to solve the Boltzmann transport equation and calculate the average energies of the carriers while they relax after undergoing an initial excitation in energy. The percentage of carriers undergoing an impact ionization event, thereby creating a new electron-hole pair, is also calculated.

The band structure of the cladded nanowire is calculated using the $sp^3d^5s^*$ empirical Tight Binding (TB) model including spin. To calculate the band structure, the supercell of the cladded nanowire must first be calculated. The cladded nanowires consist of an $In_{0.53}Ga_{0.47}As$ core cladded with InP. At 53% In, $In_{0.53}Ga_{0.47}As$ is lattice matched to InP. The supercell is created for a given thickness of the core nanowire and a given thickness of the cladded material. The resultant supercell of the cladded nanowire for a 2.0 nm × 2.0 nm $In_{0.53}Ga_{0.47}As$ core and 1.5 nm of InP cladding is shown in Figure 5.5.

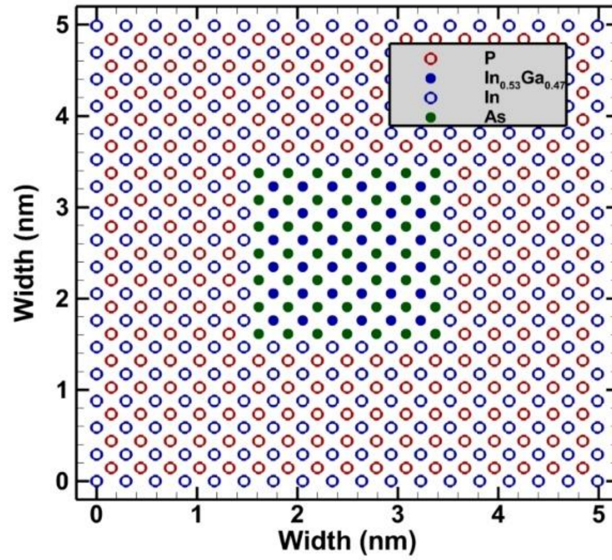

Figure 5.5: The supercell of a 2.0 nm × 2.0 nm $In_{0.53}Ga_{0.47}As$ nanowire along [100] cladded by 1.5 nm of InP.

As can be seen in the Figure 5.5, besides needing the tight binding material parameters for $In_{0.53}Ga_{0.47}As$ and InP, the material parameters for InAs are also needed as there are In-As bonds at the edge between the two materials. The cladded nanowire containing 50 supercells is shown in Figure 5.6. The cladded material is shown in blue and the core in red.

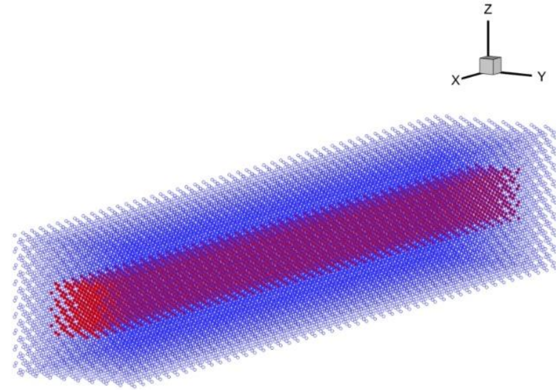

Figure 5.6: 50 supercells of a 2.0 nm × 2.0 nm $In_{0.53}Ga_{0.47}As$ nanowire along [100] cladded by 1.5 nm of InP. The InP atoms are shown in blue and the $In_{0.53}Ga_{0.47}As$ atoms in red.

The band structure of a 2.0 nm × 2.0 nm $In_{0.53}Ga_{0.47}As$ nanowire with 1.5 nm InP cladding is shown in Figure 5.7 and the band structure of a 2.0 nm × 2.0 nm $In_{0.53}Ga_{0.47}As$ nanowire with 0.5 nm is shown in Figure 5.8. The first 300 conduction bands are shown in both figures. As can be seen from the figures, increasing the cladding thickness greatly reduces the energy span of the conduction bands making them denser at high energies for higher cladding thicknesses.

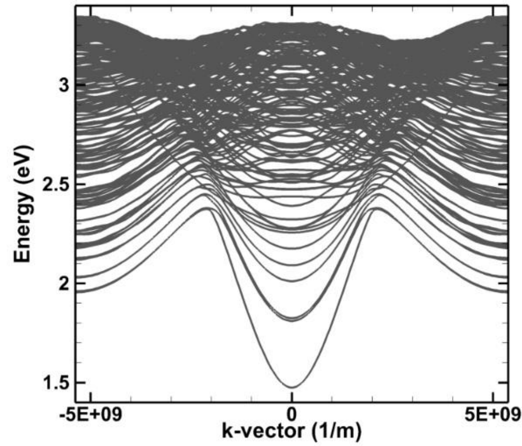

Figure 5.7: The first 300 conduction bands of a 2.0 nm × 2.0 nm $In_{0.53}Ga_{0.47}As$ nanowire along [100] with 1.5 nm InP cladding.

The variation of the band gap of the cladded nanowire is shown for different cladding thicknesses in Figure 5.9. Increasing the thickness of the cladding layer reduces the band gap because of the reduced confinement of the nanowire.

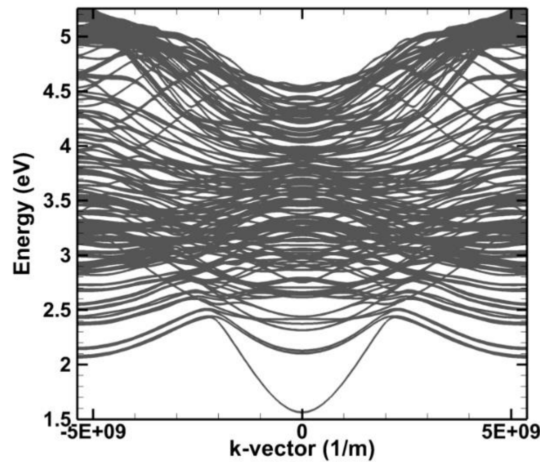

Figure 5.8: The first 300 conduction bands of a 2.0 nm × 2.0 nm $In_{0.53}Ga_{0.47}As$ nanowire along [100] with 0.5 nm InP cladding.

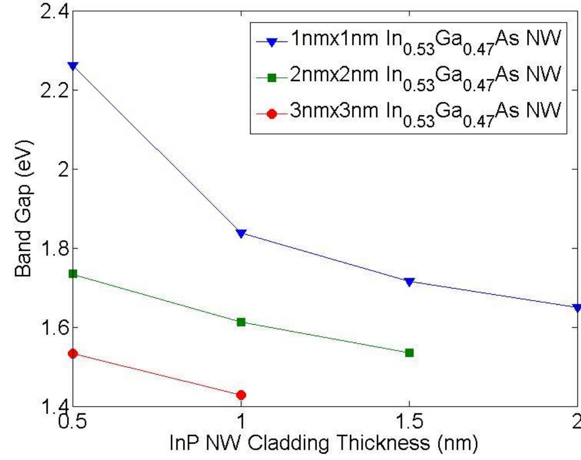

Figure 5.9: Band gap of $In_{0.53}Ga_{0.47}As$ nanowires along [100] with InP cladding for different wire and cladding thicknesses.

The scattering rates are calculated according to the methods described in Chapter 3 except the impact ionization rates. The impact ionization rates are calculated using a simple power law similar to the method used for bulk rates (Fischetti1991). The power law is given by

$$W_{II}(k,k') = \alpha\left(E - E_g\right)^{\beta} \tag{5.1}$$

where E_g is the band gap of the cladded nanowire, E is the kinetic energy of the state k and α and β are fitting parameters with values 1.7×10^{13} eV^{-2}s^{-1} and 2.0 respectively.

To simulate hot carrier relaxation, the electrons are initialized with a Gaussian distribution at a mean energy greater than the band gap of the material. The standard deviation of the Gaussian distribution is 20 meV. A full band uniform field Monte Carlo simulation is then run and the average carrier energies are calculated as a function of time as they relax. The average energy of the electrons for different nanowire cladding

dimensions as they relax is shown in Figure 5.10 and Figure 5.11. The electrons are initialized at 1.2 E_g above the conduction band minima

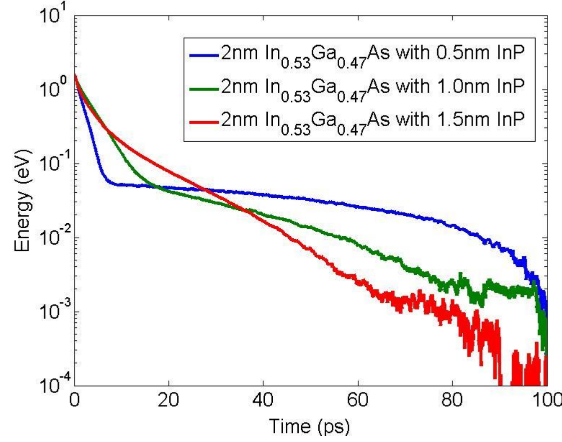

Figure 5.10: Average electron energies for 2 nm ×2 nm $In_{0.53}Ga_{0.47}As$ nanowire along [100] with different cladding thicknesses.

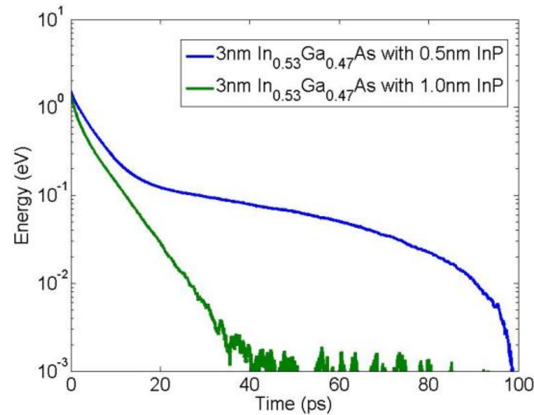

Figure 5.11: Average electron energies for 3 nm ×3 nm $In_{0.53}Ga_{0.47}As$ nanowire along [100] with different cladding thicknesses.

The percentage of carriers undergoing impact ionization is also calculated as a function of the excitation energy. As can be seen in Figure 5.12, the excitation energy of the electrons has to be above $1.2\,E_g$ to $1.4\,E_g$ of the nanowire to have a significant

percentage of the electrons undergo impact ionization. This is due to the fact that unless the electrons are sufficiently excited, they will lose energy and relax to below one band gap above the conduction band minima before they have the chance to undergo an impact ionization event and generate an electron-hole pair.

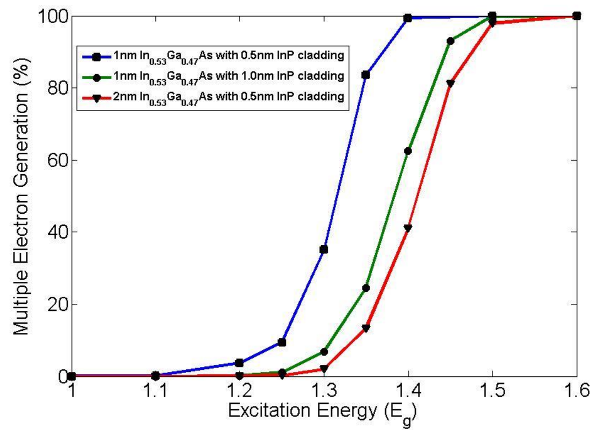

Figure 5.12: Percentage of carriers undergoing impact ionization (multiple electron generation) as a function of excitation energy for different nanowire claddings.

6. DEVICE SIMULATIONS

6.1. Junctionless Nanowire Field Effect Transistors

In the previous chapters, the low field and high field transport in nanowires were analyzed. The full band structure of nanowires and the scattering rates were calculated using the tight binding model and compared to the bulk rates at high energies and large nanowire widths. To simulate high field transport, it was also found out that the traditional free-flight drift routine of a Monte Carlo model had to be modified to account for multi-band transport and interband tunneling. In this chapter, the focus will be on the simulation of realistic nanowire devices. The tool chosen to do this is the three-dimensional particle based Cellular Monte Carlo (CMC) code developed at Arizona State University (Saraniti2000). To simplify matters, at the moment, only the transport in junctionless nanowire FETs (JNFETs) is considered in this chapter.

Junctionless nanowire FETs (JNFETs) have gained popularity since its demonstration by the Tyndall Institute (Colinge2010).The device is relatively simple to fabricate, with good scaling behavior, making it a promising next-generation technology for the end of the semiconductor roadmap. A JNFET consists of a single nanowire either p-doped or n-doped. It is usually gated all around and the source and drain are on either end of the nanowire as shown in Figure 6.1.

In the present work we implement a full band particle based Monte Carlo simulation coupled with a Schrödinger solver to simulate quantum confinement effects and phonon limited dissipative transport in the JNFET. In order to treat the carriers as a

particle but still retain all the effects of quantum confinement, the traditional CMC has to be modified. The carrier is still assumed to be a particle along the direction of the nanowire axis but its charge is assumed to be smeared along the confined directions. At any point in the device, the band structure of the carrier is given by the solution of the Schrödinger equation. The Schrödinger equation is solved by using the semi-empirical $sp^3d^5s^*$ Tight Binding (TB) model including spin-orbit interaction. The charge carriers are treated as particles moving freely along the axis of the nanowire and confined along the transverse directions.

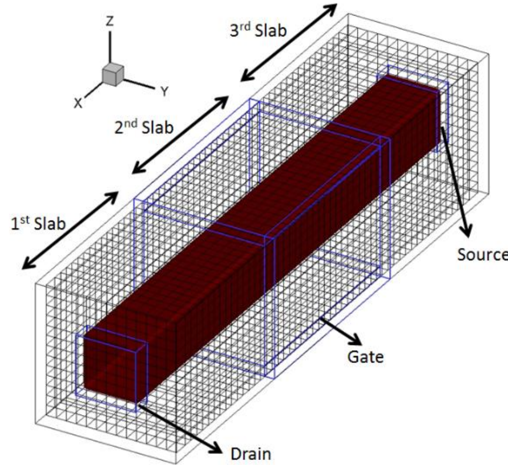

Figure 6.1: An example device structure showing the division of the JNFET into slabs to simplify the computations.

The device is divided into several 'slabs' along the axis of the nanowire as shown in Figure 6.1. Each slab is treated as a separate material with its own 1D band structure and 1D scattering rates. The slab is then populated with atoms depending on the material, nanowire orientation and physical dimensions. By assuming the slab extends infinitely along the axis of the wire a unit cell for the nanowire is calculated as described in chapter

2. This unit cell is used in the $sp^3d^5s^*$ TB model to obtain the 1D band structure of the slab as shown in Figure 6.2.

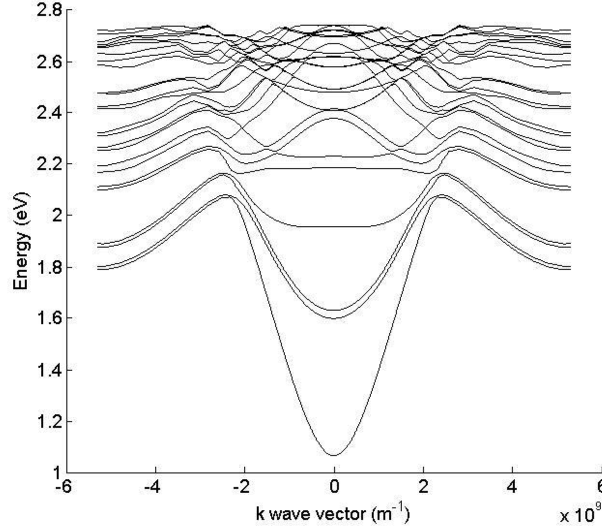

Figure 6.2: Band Structure for a 3 nmx3 nm $In_{0.7}Ga_{0.3}As$ nanowire.

From the TB coefficients the 1D scattering rates for every *k* to *k'* are calculated as discussed in previous chapters and stored in lookup tables. Even though the carrier is assumed to be a point charge along the axis of the nanowire to account for confinement effects its charge distribution along the confinement directions should be smeared according to its wave function. The charge of a single carrier is distributed along the entire cross-section of the nanowire according to equation (6.1) and as shown in Figure 6.3.

$$\rho(\mathrm{r_m}) = q_c \sum_{l=1}^{n_l} \left| C_{l,m}(k,i) \right|^2 \tag{6.1}$$

where r_m is the cross-sectional position of the atom *m* in the unit cell. q_c is the charge of carrier *c*. n_l is the number of atomic orbitals on atom *m*. $C_{l,m}(k,i)$ is the TB coefficient of

carrier *c,* at atom m and orbital *l* which is at wave vector *k* and band *i.* In Figure 6a, a carrier (red circle) is shown within a particular Poisson slice (1 cell width along the nanowire axis direction).

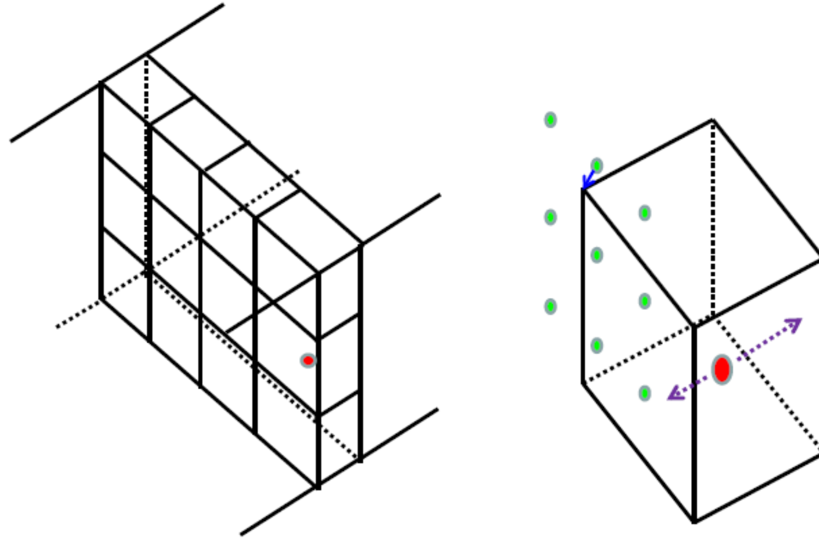

Figure 6.3: Diagram showing the charge of the carrier distributed along the atoms within a Poisson well.

The carrier's charge now has to be distributed according to its wave function according to equation (6.1) along the atoms in the cross-section of the nanowire denoted by green circles in Figure 6b. This has to be done for all the carriers present in that Poisson slice during the charge assignment step of the particle based CMC. An example of the distributed charge for an electron in the 1st conduction band at the Gamma point in a 3 nm x 3 nm GaAs nanowire along [100] is shown in Figure 6.4a. Due to the localized nature of the basis states in the tight binding scheme, each spike in the charge distribution shown in Figure 6.4a is the charge on a single atom. The potential obtained from the output of the Poisson solver is still smooth as shown in Figure 6.4b.

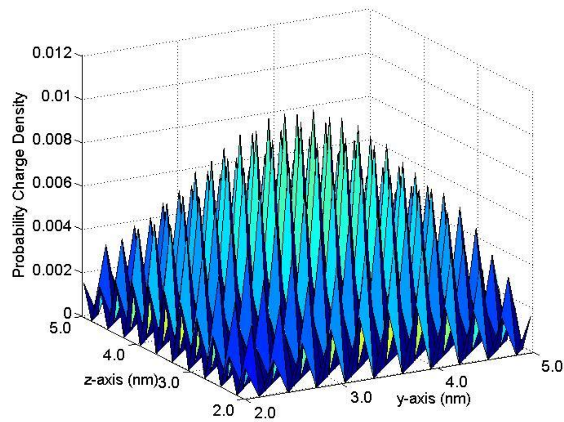

a)

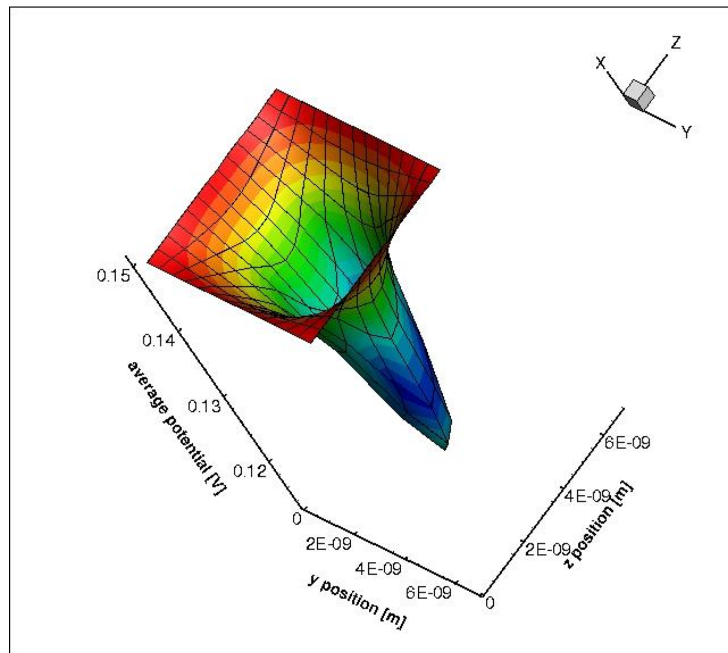

b)

Figure 6.4: a) Probability charge density across the cross-section of a nanowire for a 3 nmx3 nm $In_{0.7}Ga_{0.3}As$ nanowire for an electron at the 1st conduction band at the Gamma point. b) Potential variation along the cross-section of the device based on the solution of the Poisson solver showing quantum confinement.

Once the charge on each atom due to all the carriers is calculated according to equation (6.1) it is then interpolated onto the grid points of the Poisson solver using the same charge schemes that is used in bulk particle based CMC's (Saraniti2000). Therefore, depending on the number of carriers within 1 Poisson slice along the nanowire axis and depending on their wave function, the cross sectional charge density distribution is obtained. This has to be done for every Poisson slice in every 'slab' in the JNFET. Each slab could have a different set of TB coefficients, so depending on which slab the carrier is in, the corresponding band structure is used.

Each node in the Poisson grid has an associated cross-sectional area. All atoms within that area are assigned to that node. The charge on a node is then calculated by summing over the charge of all atoms within that node. This way the charge of a carrier is distributed across all nodes in its cross-sectional area. The 3D Poisson equation is then solved. The potential obtained from the Poisson solver is interpolated back to the atom positions and fed back in to the TB model to recalculate the band structure. Ideally each Poisson slice in the device structure should be assigned to be a single slab. But this means that each Poisson slice of the device has to have its own band structure and own scattering rates table. This becomes very computationally expensive so usually many Poisson slices are grouped together to form a single slab. If a single slab contains many Poisson slices as shown in Figure 6.2, then the potential over all the Poisson slices are averaged and then interpolated to the atoms. This process of recalculating band structures and scattering rates is done self-consistently until steady state is achieved. The MC free-flight and scatter routines are purely one dimensional while the Poisson solver, charge

distribution and potential distribution is three-dimensional. Since the TB solver and scattering rate calculation is computationally expensive, the band structure and scattering rates of each slab are only recalculated once every 0.5ps during the simulation as shown in the flowchart in Figure 6.5.

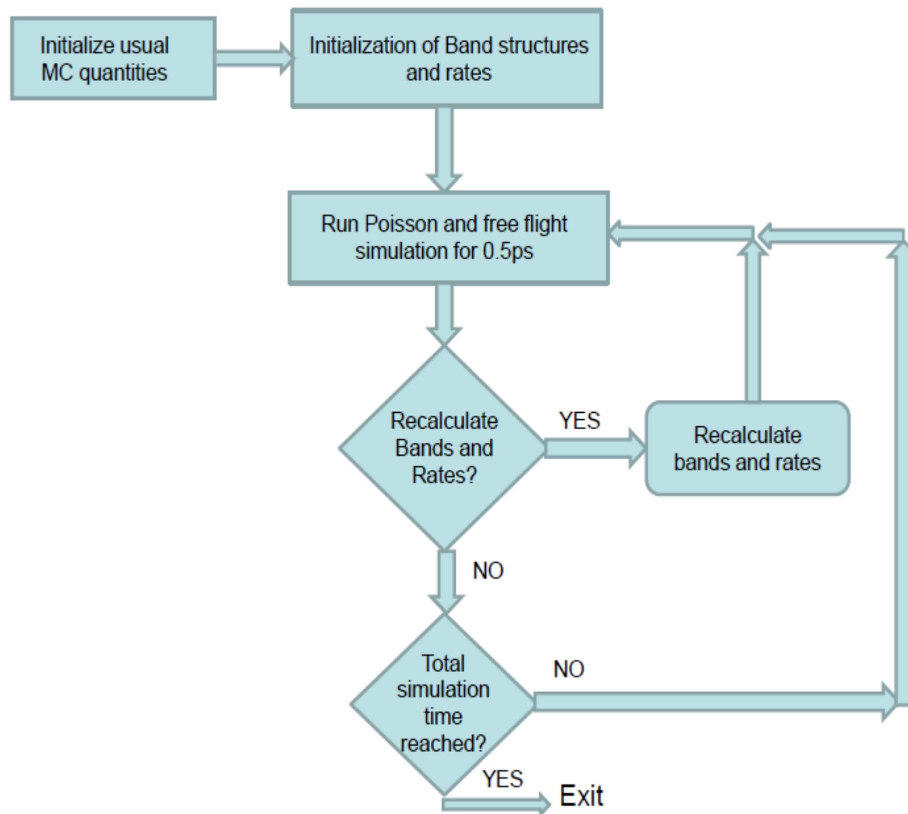

Figure 6.5: Flowchart for the 1D Monte Carlo Method.

This process can be extended to include more slabs in the device to improve the accuracy of the method at an increased cost computationally. Also if the potential does not vary much after 0.5 ps the band structure and scattering rates of the slab do not need to be recalculated as shown in the flowchart in Figure 6.5. This will reduce the computational cost.

6.2. Transport across Different Slabs

As the different slabs defined in the previous section have their own band structure and scattering rates, they must be treated as different materials itself. Therefore, as a carrier drifts from one slab to another slab it is treated as if it is moving across a hetero interface.

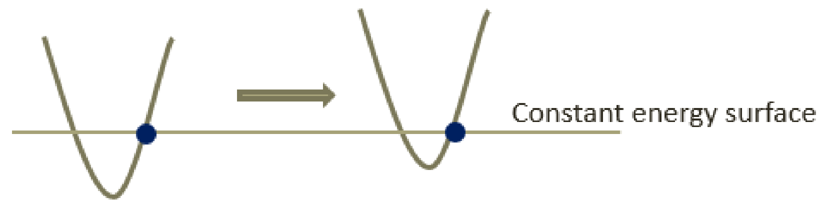

Figure 6.6: Transfer of a carrier moving from 1 slab to another slab. The energy and momentum is conserved during the transition.

If the energy of the carrier is lies within the band gap of the slab it is moving into, then the carrier is reflected back classically. If the carrier has sufficient energy to overcome the band offsets, the energy and momentum of the carrier is conserved by placing it appropriately in the band structure of the new slab. A perfect conservation of momentum and energy is not always possible as that state may not exist in the new slab, the algorithm minimizes the energy and momentum loss in those cases. When the new state is chosen in the new slab, it is important that the k-space state chosen does not have a velocity opposite to the initial velocity so as to prevent the carrier from being reflected back to the first slab.

6.3. Surface Injection at Contacts

In semi-ballistic devices, the injection statistics play an important role in device behavior. Traditionally, the contact injection is performed by maintaining charge neutrality at all the cells in the contact region. After a free-flight drift, the excesses charges in a contact are removed and if there is a deficit of charge, carriers are injected into the contact cell according to the Maxwell distribution function. The removal and addition of charge constitutes a current and the net current out of a contact is calculated by the rate of net charge removed from all the contact cells as described in equation (6.2)

$$I_C = -\sum_{i=1}^{ncells} -\frac{\Delta q_i}{\Delta t} \tag{6.2}$$

where I_C is the current out of the contact, $ncells$ is the number of cells within the contact, Δq_i is the net charge removed/added from cell i and Δt is the free-flight drift time. This method of contact injection works well when the device is large and sufficient scattering takes place in the region outside the contact. But in devices where ballistic transport is a possibility the charge neutrality method of injection is known to produce spurious results as the distribution function injected is not correct (Gonzalez1996). This can be a problem in a JNFET where a fraction of the current could be ballistic.

To accurately model contact injection, the carriers are assumed to be injected from ideal thermal reservoirs (Gonzalez1999). The contact is treated as a surface which injects at a constant rate depending on the temperature and doping of the material it is in contact with. Any carrier that crosses this surface in the other direction is ejected. Since this is a full band calculation the k-space is discretized. The density in k-space of the incoming

electron states with wave vector k impinging per unit time upon the surface between the contact and semiconductor is

$$N(k) = DOS\left(k\right)v(k)A \tag{6.3}$$

where $DOS\left(k\right)$ is the density of states at wave vector k, $v\left(k\right)$ is the velocity of the state and A is the cross-sectional area of the contact surface. The units of $N\left(k\right)$ in equation (6.3) is $1/s$. This means that every $1/N(\mathrm{k})$ seconds a state with wave vector k is introduced into the semiconductor. Since this number is usually very small, a time interval equal to the free-flight time is used. Density in a certain time interval Δt in a certain range of k is,

$$N\left(\Delta k, \Delta t\right) = N\left(k\right)\Delta k \Delta t\left(\frac{e}{q_c}\right) \tag{6.4}$$

where e is an electron charge and q_c is the charge of the carrier. Once a state is introduced, the probability of that state being occupied is given by

$$r < f(E(k)) \tag{6.5}$$

The free-flight time interval is divided into $N(\Delta k, \Delta t)$ units. At each time unit, a state is generated and if a carrier is generated, it is drifted for the remaining time interval as shown in Figure 6.7.

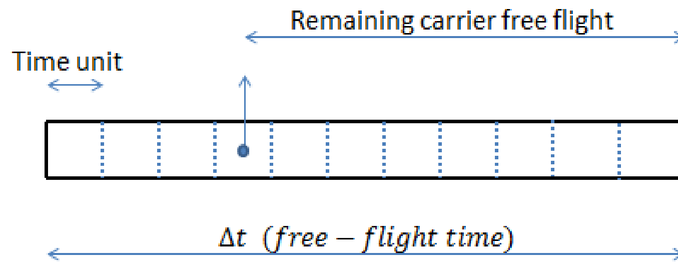

Figure 6.7: Schematic showing the carrier injection algorithm.

The injection rate does not depend on the applied voltage or the electric field immediately outside the contact. This can remove spurious results such as a < 60 mV/dec subthreshold swing in a JNFET as shown in Figure 6.8. Also due to the surface contact injection method, the artificial resistance drop at the contacts is significantly reduced as deduced from the increase in overall current in Figure 6.8.

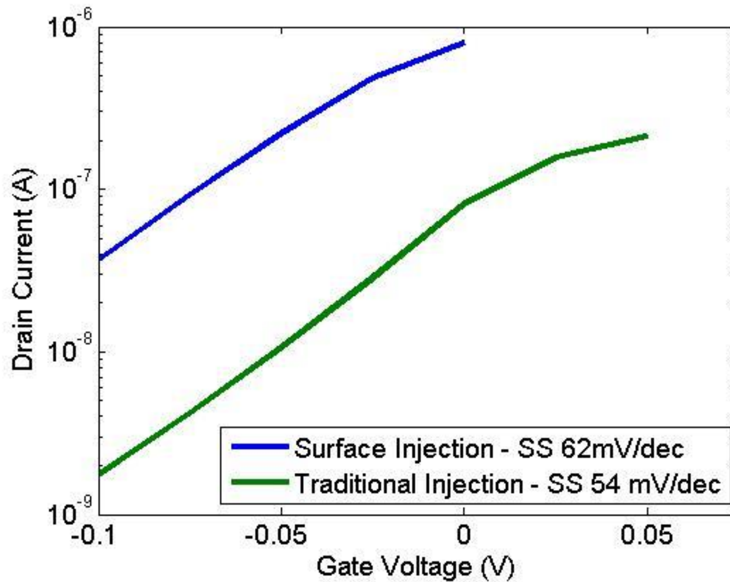

Figure 6.8: Comparison of subthreshold swing (SS) of a JNFET using the traditional charge neutrality injection method and the surface injection method.

6.4. Simulation of $In_{0.7}Ga_{0.3}As$ JNFET

The device structure simulated consists of an n-type 3 nm x 3 nm $In_{0.7}Ga_{0.3}As$ nanowire doped to 10^{18} cm^{-3}. The gate is wrapped around the nanowire with a dielectric thickness of 2 nm. The source and drain contacts are on either end of the nanowire. The length of the device is 100 nm but varies based on the simulation. The gate length is 40 nm as shown in Figure 6.7 and is also varied. The device was divided into 3 'slabs', one from the source to the gate, one under the gate and the other from the gate to the drain. The band structure and scattering rates of the slabs were recalculated every 0.5 ps till the simulation converged.

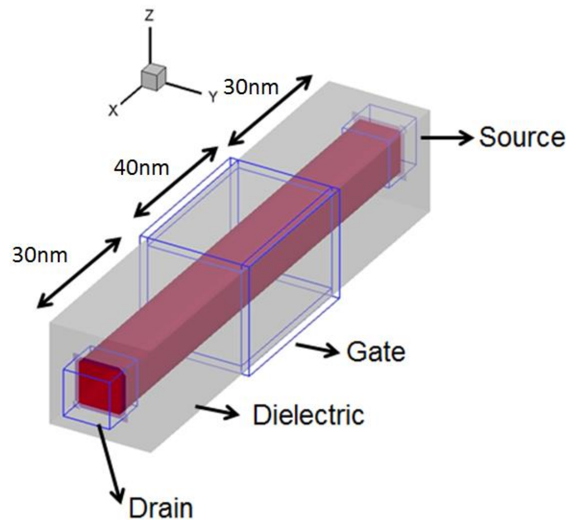

Figure 6.9: General JNFET device structure simulated.

The I_D-V_G and I_D-V_D curves are shown in Figure 6.10. The device structure is varied to observe the effect of device length on the subthreshold swing. The ratio of the gate length to the device length is kept a constant for all simulations. The injection statistics starts to

play a role at low device lengths as the devices start to become semi-ballistic at low gate lengths. The variation on subthreshold swing with different gate lengths is shown in Figure 6.11 for a 3 nm x 3 nm $In_{0.7}Ga_{0.3}As$ JNFET. The subthreshold swing seems to saturate at a value of 62 mV/dec, slightly higher than the ideal value most likely due to the discretization of the k-space in a full band Monte Carlo simulation which causes a corresponding energy error.

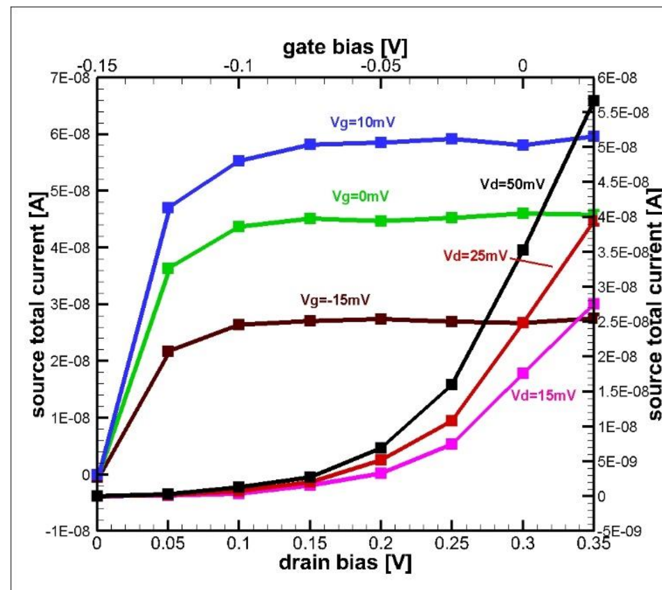

Figure 6.10: I_D-V_D and I_D-V_G curves for different V_G and V_D values respectively for the device structure shown in Figure 6.7.

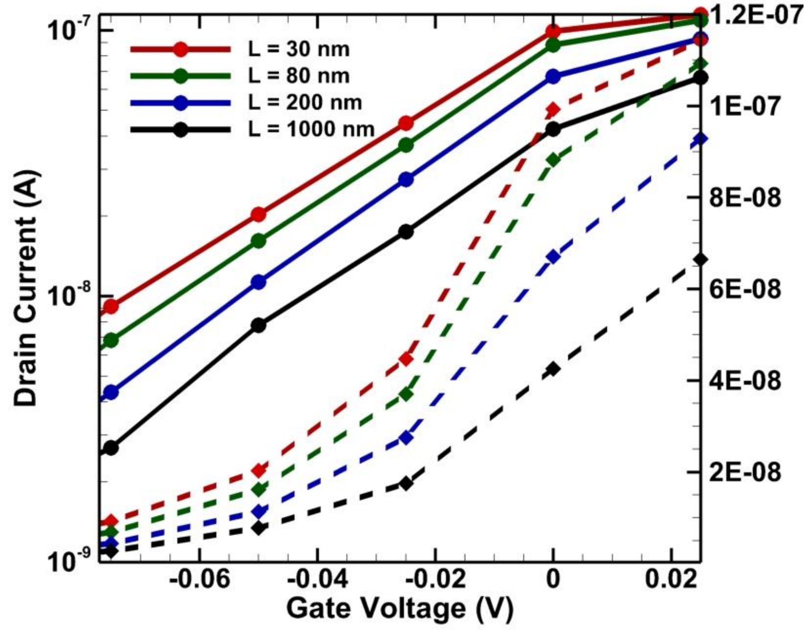

a)

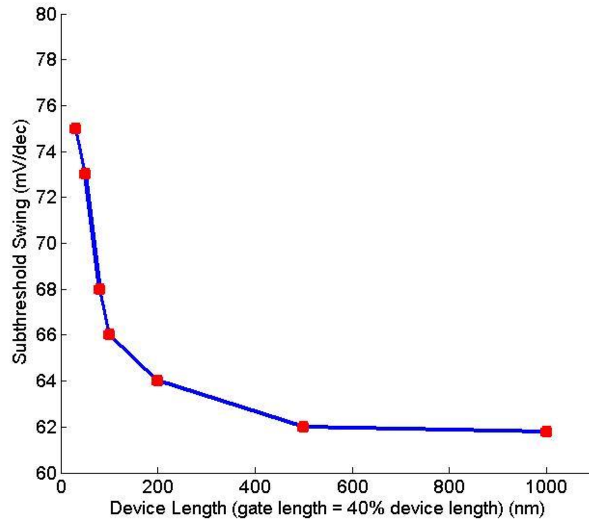

b)

Figure 6.11: a) Plot of I_D vs V_G for different gate length JNFETs, b) Variation of subthreshold swing of the nanowire JNFET against its device and gate length.

6.5. Ballistic Percentages

Due to the particle based nature of the CMC, the number of particles that encounter a scattering event can be easily calculated.

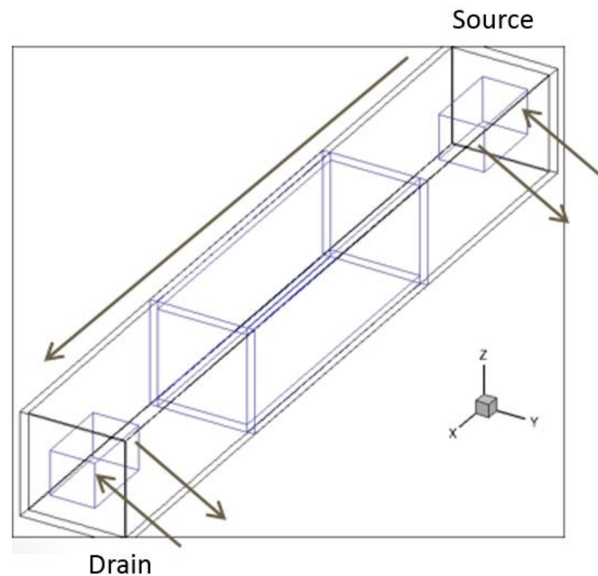

Figure 6.12: Schematic plot of a JNFET showing the paths a carrier can take from the point of injection to ejection. Only the path traveling from one contact to another is considered in the study of ballisticity.

While keeping track of the carriers undergoing a scattering event, only the carriers that are injected at the source and reach the drain, or vice versa should be included in the calculation. Due to the nature of surface injection, a large injection and ejection of carriers is constantly occuring at the contacts and those carriers that do not make it across the device should be discarded as shown in Figure 6.12.

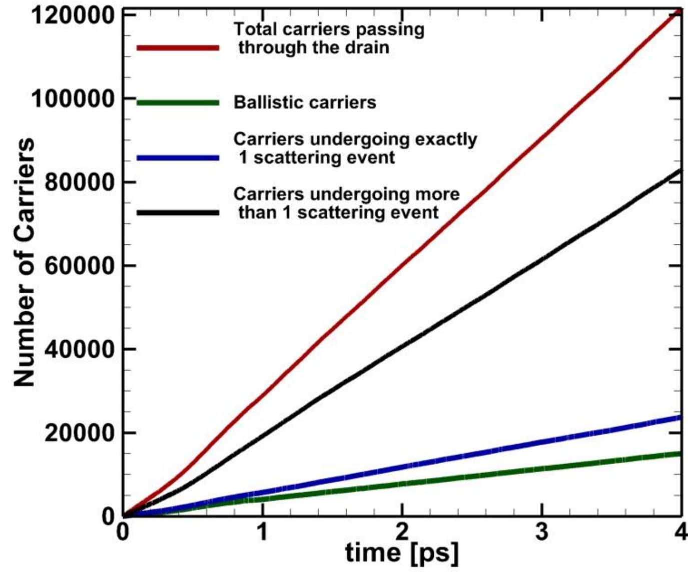

a)

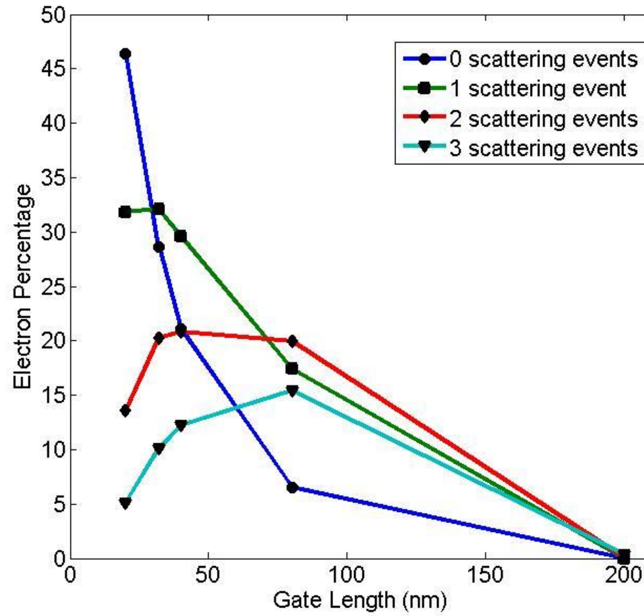

b)

Figure 6.13: a) Plot of total carriers passing through the drain that underwent different number of scattering events, b) Ballistic percentage as a function of gate length.

The number of carriers exiting the contact can be very noisy due to the low currents obtained from these devices. If one were to simply find the mean of the number of carriers exiting the contacts at every time step, the result would be too noisy. To reduce the noise, instead of calculating the number of carrier exiting every time step, the total number of carriers exiting the contact since the start of the simulation is stored at every time step. This is shown in Figure 6.13a for a device length of 200 nm. A counter can be stored on each carrier keeping track of the number of times it undergoes a scattering event. Once the data shown in Figure 6.13a is obtained, the slope of each line can be calculated to a very low degree of error. The ratio of the slopes gives the ballistic percentage as shown in equation (6.6)

$$B_i = \frac{S_i}{S_{total}} \times 100 \tag{6.6}$$

where B_i is the ballistic percentage of a carrier undergoing i scattering events, S_i is the slope of the number of carriers that underwent i scattering events versus time and S_{total} is the slope of the total number of carriers passing through the drain versus time. The plot of ballistic percentages versus different device lengths is shown in Figure 6.13b. As can be seen, the percentage of carriers that go through the device without scattering drops quickly as the device length increases.

7. SUMMARY AND CONCLUSIONS

In this work, the transport in nanowires and nanowire devices is analyzed using the full band Monte Carlo model and the empirical tight binding model. Modifications to the existing Monte Carlo method were undertaken to simulate nanoscale materials and devices. Chapter 1 was dedicated to the emergence of nanoscale devices in current integrated circuit technology and the methods employed to study transport in such nanoscale devices. The Monte Carlo method was shown to be optimal to simulate such devices as it is relatively computationally inexpensive compared to the NEGF methods while still being physically accurate due to the possibility of incorporating transport in a fully quantum way , making it more desirable than the computationally inexpensive but physically inaccurate drift diffusion models.

Chapter 2 discusses the empirical tight binding method used to calculate the bulk and nanowire full band structures. Due to its atomistic nature, the same parameters used to simulate the bulk material band structure can be used to simulate the nanowire material band structure. Therefore no additional parameters are introduced in order to calculate the nanowire band structure. Important physical properties such as the band gap are shown to agree to bulk values as the nanowire widths increase. At high energies it is shown that the density of states of the nanowire rapidly oscillates around the density of states value of the bulk material for the same set of tight binding parameters.

Chapter 3 discusses the calculation of the scattering rates in 1D systems using the Fermi's golden rule. New scattering rates are derived for the deformation potential scattering rate, polar optical phonon scattering rate, ionized impurity scattering rate, surface roughness scattering rate and the impact ionization scattering rate. A new formula

to calculate the dielectric screening in 1D systems is also derived within the tight binding basis. Importantly it is shown that the scattering rates of the nanowire material oscillate around the same scattering rates of the bulk material at high energies for the same scattering rate parameters. This is consistent with the density of states of the nanowire approaching the value of the bulk material at high energies. A useful optimization of the calculation of the overlap integral in the scattering rates is also discussed. The improvement in the computation speed of the overlap integral allows for relatively large nanowire scattering rates to be calculated.

Chapter 4 focuses on the low field and high field transport in nanowire materials. The Boltzmann transport equation is analyzed for low fields using the Rode's method derived for 1D systems. Using the Rode's method, the mobility of the nanowires are extracted. The mobility values are shown to approach the bulk value for large nanowire widths in Si and GaAs nanowires along the [100] direction. The variation of the mobility with doping concentration is also discussed and the effect of screening is demonstrated. The latter part of the chapter discusses the uniform field Monte Carlo method as a means to analyze transport in the high field regime in nanowires. The scattering rate parameters of bulk Si and bulk GaAs are fitted to experimentally obtained velocity field curves and mobility values. The same parameters are then used to simulate transport in nanowire materials.

We also presented a new solution of the KI equations for multi-band transport using the Magnus expansion method. The usefulness of the Magnus expansion to solve the problem of multi-band drift is demonstrated by using it to solve the KI equation across the full BZ in semiconductor nanowire systems. The ability of the Magnus

solution to retain qualitative properties of the original solution greatly simplifies the problem. Depending on the problem at hand, the Magnus series can also be accordingly truncated to the required degree of accuracy, reducing the computation time without introducing exponentially increasing errors as is the case with the Runge-Kutta 4th order method. The importance of field induced interband tunneling is shown by performing uniform field full band Monte Carlo simulations of Si and InAs nanowires by modifying the traditional free-flight drift routine. Depending on the nature of the band structure, the multi-band drift model may or may not be necessary. Interband tunneling also becomes very important at high electric fields where impact ionization may be dominant. In such cases, it is important to include this model in the traditional Monte Carlo routines to accurately account for the correct number of impact events at high electric fields.

The velocity field curves of Si and GaAs for different nanowire widths along the [100] direction are obtained and compared with the bulk velocity field curves for electrons and holes. As the nanowire width increases the velocity field curves seem to approach the bulk velocity field curves except at very high fields where the velocity of the nanowire systems start to decrease.

In Chapter 5 the energy relaxation of excited carriers in free-standing and cladded nanowires are discussed. Using a full band Monte Carlo simulation the electron energy relaxation times of InAs nanowires along the [100] direction are shown to be greater than the energy relaxation time of bulk InAs. At moderately high electric fields, a runaway effect is also observed in the nanowires and is attributed to the 1D nature of the scattering rates. A full band Monte Carlo simulation is also used to evaluate the carrier relaxation in cladded nanowires. The energy relaxation as a function of time is studied for different

cladding and core thicknesses. By using a simple impact ionization model, the multi-excitation generation of carriers is also studied as a function of excitation energy. It is found out that the excitation energy must be sufficiently above the band gap to allow for the carriers to undergo impact ionization even after dissipating energy through various scattering mechanisms.

In Chapter 6 a full band particle based Monte Carlo simulator is constructed for nanowire devices. This chapter presents a numerical technique for Monte Carlo simulations of nanowire devices by fully including quantum mechanical confinement effects and dissipative phonon scattering within a full-band framework. The modeling of the carrier as a particle along the free direction and as a smeared charge along the quantized directions allows for the effect of the confining potential on the band structure and scattering rates of the carrier. The inclusion of a new way to calculate the polar optical phonon scattering using the TB coefficients is also presented. The comparison between the confined scattering rates and the bulk scattering rates at high energies provides a useful way to calibrate the parameters for the confined material in a consistent way. The capabilities of the model have been demonstrated by simulating an $In_{0.7}Ga_{0.3}As$ JNFET. New materials and different device structures can be easily simulated using this technique making this a very useful simulation model for quantum devices.

7.1. Future Work

There are several place in this work where further improvements can be made. One of them is the use of confined phonons instead of the bulk phonon dispersion

relation. There have been recent work done on the effect of confinement on Si nanowires and it has been shown that for small nanowire widths (2 nm x 2 nm and 3 nm x 3 nm) the effect of confined phonons is important (Buin2008). The scattering rates described in Chapter 3 can be easily modified to allow for confined phonons and instead of integrating over the phonons along the confined direction, there will be a summation over the confined phonon modes.

Also the scattering rates can be improved by using a self-consistent Green's function approach to account for the energy broadening due to collisions. This will smoothen out the peaks in the scattering rates that are there due to the 1D density of states that are calculated using Fermi's golden rule. This will help the device simulation runs too, as there won't be spikes in the scattering rate forcing the reduction of the free-flight time.

Finally, comprehensive simulations using the modified particle based CMC described in chapter 6 needs to be run to understand the effect of various structures and scattering mechanisms on the characteristics of JNFETs.

REFERENCES

Alvi, P.A. Lal, K.M. Siddiqui, M.J. Naqvi, A. 2005. Carbon Nanotubes Field Effect Transistors: A Review. *Indian Journal of Pure & Applied Physics* 43: 899-904.

Bertazzi, F. Moresco M. and Bellotti, E. 2009. Theory of high field carrier transport and impact ionization in wurtzite GaN. Part I: A full band Monte Carlo model. *Journal of Applied Physics* 106(063718).

Blanes, S. Casas, F. Oteo, J. A. and Ros, J. 2009. The Magnus expansion and some of its applications. *Physics Reports* 470:151-238.

Boykin, T.B. Klimeck, G. Oyafuso, F. 2004. Valence Band Effective-mass Expressions in the $sp^3d^5s^*$ Empirical Tight-binding Model applied to a Si and Ge Parametrization. *Physical Review B.* 69(115201).

Boyle, P. Broadie, M. Glasserman, P. 1997. Monte Carlo Methods for Security Pricing. *Journal of Economic Dynamics and Control.* 21 (8-9): 1267-1321.

Brennan, K.F. Bellotti, Farahmand, E. M. Nilsson, H.-E. Ruden, P. P. Zhang, Y. 2000. Monte Carlo simulation of noncubic symmetry semiconducting materials and devices *IEEE Trans. Electron Devices* 47(1882).

Brews, J.R. et al. 1980. Generalized Guide for MOSFET Miniaturization. *IEEE Electron Device Letters* 1.1: 2-4.

Buin, A.K. Verma, A. Anatram, M.P. 2008. Carrier-Phonon Interaction in Small Cross-sectional Silicon Nanowires. *J. Appl. Physics.* 104(053716).

Cardona, M. 2006. Vibrational Spectra of Hydrogen in Silicon and Germanium. *Physica status solidi (b)* 118(2):463-481.

Chelikowsky, J.R. Cohen, M.L. 1984. Nonlocal Pseudopotential Calculations for the Electronic Structure of Eleven Diamond and Zinc-Blende Semiconductors. *Phys. Rev. B.* 30(4828).

Choi, Y.-K. Lindert, N. Xuan, P. Tang, S. Ha, D. Anderson, E. King, T.-J. Bokor, J. Hu, C. 2001. Sub-20nm CMOS FinFET Technologies. *IEEE International Electron Devices Meeting Technical Digest* 421-424.

Colinge, J-P. Lee, C-W. Afzalian, A. Akhavan, N.D. 2010. Nanowire Transistors without Junctions. *Nature Nanotechnology*, 5: 225-229.

Crane, H.L. Gibbs, N. Poole, W. Stockmeyer, P. 1976. Matrix Bandwidth and Profile Reduction. *ACM Trans. On Mathematical Soft.* 2(4): 375-377.

Cui, Yi. Zhong, Zhaohui. Wang, Deli. Wang, Wayne U. Lieber, Charles M. 2003. High Performance Silicon Nanowire Field Effect Transistors. *Nano Letters* 3 (2): 149-152.

Dastjerdy, E. Ghayour, R. Sarvari, H. 2010. 3D Quantum Mechanical Simulation of Square Nanowire MOSFETs by using NEGF Method. *Central European Journal of Physics* 9(2):472-481.

Datta, S. 1997. Electronic Transport in Mesoscopic Systems, *Cambridge, UK: Cambridge University Press*.

Dmitriev, A.P. Kachorovskii, V.Yu. Shur, M. Stroscio, M.A. 2000. Electron Runaway and Negative Differential Mobility in Two Dimensional Electron or Hole Gas in Elementary Semiconductors. *Solid State Comm.* 113:565-568.

Fer F. Bull. 1958. Résolution de l'équation matricielle U=pU par Produit infini d'exponentielles matricielles. *Classe Sci. Acad. Roy. BeI*, 44:818-829.

Ferry, D. Goodnick, S.M. 1997. *Transport in Nanostructures*. Cambridge University Press.

Fiori, G. Iannaccone, G. 2007. Three-Dimensional Simulation of One-Dimensional Transport in Silicon Nanowire Transistors. *IEEE Transactions on Nanotechnology* 6(5).

Fischetti, M. Laux, S.E. 1988. Monte Carlo Analysis of Electron Transport in Small Semiconductor Devices Including Band-structure and Space-charge Effects. *Phys. Rev. B.* 38(9721).

Frank, DJ. Dennard, RH. Nowak, E. Solomon, PM. Taur, Y. Wong, HSP. 2001. Device Scaling limits of Si MOSFETs and their application dependencies. *Proceedings of IEEE* 89 (3): 259-288.

Gonzalez, T. Mateos, J. Pardo, D. Varani L. and Reggiani, L. 1999. Injection Statistics Simulator for Dynamic Analysis of Noise in Mesoscopic Devices. *Semicond. Sci.Technol*. 14.

Hernandez, V. Roman, J.E. Vidal, V. 2005. SLEPc: A Scalable and Flexible Toolkit for the Solution of Eigenvalue Problems. *ACM Trans. Math. Software.* 31(3): 351-362.

Horiguchi, S. 1996. Validity of Effective Mass Theory for Energy Levels in Si Quantum Wires. *Physicia B* 96 (4): 336-338.

Iserles A. and Nørsett, S. P. 1999. On the Implementation of the Method of Magnus Series for Linear Differential Equations. *Phil. Trans. R. Soc. Lond, A* 357:983–1019.

Jacoboni, C. Reggiani, L. 1983. The Monte Carlo method for the solution of charge transport in semiconductors with applications to covalent materials. *Rev. Mod. Phys.* 55(645).

Kamakura, Y. Mizuno, H. Yamaji, M. Morifuji, M. Taniguchi, K. Hamaguchi, C. Kunikiyo, T. Takenaka, M. 1994. Impact Ionization Model for Full Band Monte Carlo Simulation. *Journal of Applied Physics* 75(3500).

Klimeck, G. Bowen, R.C. Boykin, T.B. Salazar-lazaro, C. Cwik, T, Stoica, A. 2000. Si Tight-binding Parameters from Genetic Algorithm Fitting. *Superlattices and Microstructures*. 27 (2/3).

Kotlyar, R. Linton, T.D. Rios, R. Giles, M.D. Cea, S.M. Kuhn, K.J. Povolotsky, M. Kubis, T. Klimeck, G. 2012. Does the Low Hole Transport Mass in <100> and <111> Si Nanowires Lead to Mobility Enhancements at High Field and Stress: A Self-consistent Tight Binding Study. *Journal of Applied Physics* 111 (123718).

Krieger J.B. and Iafrate, G.J. 1986. Time evolution of Bloch electrons in a homogeneous electric field. *Phys. Rev. B* 33(5494).

Lee, S. Oyafuso, F. Allmen, P. Klimeck, G. 2004. Boundary Conditions for the Electronic Structure of Finite-extent Embedded Semiconductor Nanostructures. *Physical Review B*. 69(045316).

Lehoucq, R.B. Sorensen, D.C. Yang, C. 1997. APRACK Users Guide: Solution of Large Scale Eigenvalue Problems by Implicitly Restarted Arnoldi Methods.

Lindefeldt, U. Nilsson H-E. and Hjelm M. 2004. Choice of wavefunction phases in the equations for electric-field-induced interband transitions. *Semicond. Sci. Technol*. 19.

Lu, W.C. Wang, C.Z. Ruedenberg, K. Hol, K.M. 2005, Transferability of the Slater-Koster Tight-binding Scheme from an Environment-dependent Minimal-basis Perspective. *Physical Review B*. 72(205123).

Luisier M. Schenk A. Fichtner W. and Klimeck, G. 2006. Atomistic simulation of nanowires in the sp3d5s∗ tight-binding formalism: From boundary conditions to strain calculations. *Phys Rev B* 74(205323).

Magnus, W. 1954. On the exponential solution of differential equations for a linear operator. *Comm. Pure and Appl. Math*. VII (4):649–673.

Martinez, A. Brown, A. R. Roy S. and Asenov, A. 2012. NEGF Simulations of a Junctionless Si Gate-All-Around Nanowire Transistor with Discrete Dopants. *Solid State Electronics* 71:101-105.

Martinez, A. Barker, J.R. Asenov, A. Svizhenko, A. Anantram, M.P. 2007. Developing a Full 3D NEGF Simulator with Random Dopant and Interface Roughness. *J Comput Electron* 6:215-218.

Moler, C. and VanLoan, C. 2003. Nineteen Dubious Ways to Compute the Exponential of a Matrix, Twenty-Five Years Later. *SIAM Review* 45(1):3-49.

Moore, G. 1965. Cramming more Components onto Integrated Circuits. *Electronics*, 38 (8): 114-117.

Nilsson, H-E. Martinez, A. Ghillino, E., Sannemo, U. Bellotti, E. Goano, M. 2001. Numerical Modeling of Hole Interband Tunneling in Wurtzite GaN and SiC, *J. Appl. Physics.* 90(2847).

Papaconstantopoulos, D.A. 1986. Handbook of the Band Structure of Elemental Solids. *Plenum, New York.*

Rees, H.D. 1969. Calculation of Distribution Functions by Exploiting the Stability of the Steady State. *J. Phys. Chem. Solids.* 30:643-655.

Rieger, M.M. Vogl, P. 1993. Electronic Band Parameters in Strained $Si_{1-x}Ge_x$ Alloys on $Si_{1-y}Ge_y$ substrates. *Physical Review B*. 48(19).

Rode, D.L. 1972. Low Field Electron Transport. *Semiconductors and Semimetals*. 10:1-89.

Saraniti, M. Goodnick, S.M. 2000. Hybrid Fullband Cellular Automaton/Monte Carlo Approach for Fast Simulation of Charge Transport in Semiconductors. *IEEE Transactions on Electron Devices* 47(10).

Schrödinger, E. 1926. Quantisierung als Eigenwertproblem. *Annalen der Physik* 80:437-490.

Vo, T. Williamson, A.J. Galli, G. 2006. First Principles Simulations of the Structural and Electronic Properties of Silicon nanowires. *Physical Review B*. 74(045116).

Vogl, P. Hjalmarson, H.P. Dow, J.D. 1983. A Semi-empirical Tight-binding Theory of the Electronic Structure of Semiconductors. *J. Phys. Chem. Solids.* 44(5): 365-378.

Vurgaftman, I. Meyer, J.R. Ram-Mohan, L.R. 2001. Band Parameters for III-V Compound Semiconductors and their Alloys. *J. Appl. Phys.* 89(5815).

Wang, J. Polizzi, E. Lundstrom, M. 2004. A Three-dimensional Quantum Simulation of Silicon Nanowire Transistors with the Effective-Mass Approximation. *Journal of Applied Physics* 96:2192-2204.

Wen-cheng L. Zi-chen, D. and Yong, H. 2006. *Applied Mathematics and Mechanics (English Edition)* 27:1383-1390.

Wilcox, R. M. 1967. Exponential Operators and Parameter Differentiation in Quantum Physics. *J. Math. Phys.* 8:962.

Zhou, L. Dimakis, E. Hathwar, R. Aoki, T. Smith, D.J. Moustakas, T.D. Goodnick, S.M. McCartney, M.R. 2013. Measurement and Effects of Polarization Fields on One-monolayer-thick InN/GaN Multiple Quantum Wells. *Physical Rev. B.* 88(125310).